UNIVERSITÀ DEGLI STUDI DI NAPOLI FEDERICO II

PH.D. THESIS IN

INFORMATION TECHNOLOGY AND ELECTRICAL ENGINEERING

INVESTIGATION OF PYROELECTRIC EFFECT GENERATED BY LITHIUM NIOBATE CRYSTALS INDUCED BY INTEGRATED MICROHEATERS

SHOMNATH BHOWMICK

TUTOR: PROF. GIOVANNI BREGLIO

CO- TUTOR: DR. GIUSEPPE COPPOLA

XXIX CICLO

SCUOLA POLITECNICA E DELLE SCIENZE DI BASE
DIPARTIMENTO DI INGEGNERIA ELETTRICA E TECNOLOGIE DELL'INFORMAZIONE

Abstract:

This thesis work focuses on the investigation of the pyroelectric effect from the –Z surface of Lithium (LiNbO$_3$) crystal using different microheater (µH) designs fabricated on the +Z surface of the crystal. Thermal analyses of the microheater designs were performed both theoretically and experimentally using COMSOL™ Multiphysics and FLIR SC7000 thermocamera respectively. The pyroelectric effect was investigated analysing the current impulses detected using a metallic probe detector connected to an oscilloscope. The temperature variation induced by the microheater causes a spontaneous polarization in the crystal resulting in the formation surface bound charges. The electric field generated between the probe and the crystal surface causes the charge emission that appears as a voltage impulse on the oscilloscope. In an ambient condition, the air layer act as a dielectric thin film layer at few hundreds of microns between the detector probe and crystal surface gap spacing. It was demonstrated and validated that the threshold field strength require to generate the PE was near the dielectric breakdown of air. The pyroelectric emission shows a higher dependency on the rate of thermalization of the microheater and also the electric field generated between the probes to surface gap spacing's of crystal. The deep characterization of µHs is investigated, in order to demonstrate the reliability and the effectiveness of these microdevices for all those applications where compact and low-power consuming electrical field sources are highly desirable.

Keywords: P*yroeletric Fields, Lithium Niobate, Microheaters, COMSOL ™, Joules Effect, thermal Effect analysis*

To my wife Sudeshna

&

My family

List of publications

i. **S. Bhowmick**, M. Iodice, M. A. Gioffrè, G. Breglio, A. Irace, M. Riccio, G. Romano, S. Grilli, P. Ferraro, L. Mecozzi, S. Coppola, O. Gennari, R. Rega, G. Coppola
"Investigation of Pyroelectric fields generated by Lithium Niobate crystals through integrated microheaters**"**
Sensors and Actuators A: Physical, (submitted),

ii. L. Mecozzi, O. Gennari, R. Rega, S. Grilli, **S. Bhowmick**, M. A. Gioffrè, G. Coppola, P. Ferraro
"SPIRALS FORMATION AT MICROSCALE BY μ- PYROELECTROSPINNING"
Soft Matter, May 2016, DOI: 10.1039/C6SM00156D

iii. O. Gennari, S. Grilli, S. Coppola, V. Pagliarulo, V. Vespini, G. Coppola, **S. Bhowmick**, M. A. Gioffrè, V. Ambrogi, P. Cerruti, C. Carfagna, P. Ferraro
"SPONTANEOUS ASSEMBLY OF CARBON-BASED CHAINS IN POLYMER MARTIXES THROUGH SURFACE CHARGE TEMPLATES"
Langmuir December 2013, 29, pp. 15503-15510, DOI: *10.1021/la403603d.*

Conference Proceedings

i. **S Bhowmick**, M Iodice, M Gioffrè, G Breglio, M Riccio, A Irace, G Romano, G Coppola:
"*Pyroelectric effect Investigation on LiNbO₃ crystal under humidity conditions using Microheater*".
11th IEEE Nanotechnology Materials and Devices Conference (2016), Toulouse, France.
DOI: 10.1109/NMDC.2016.7777087

ii. L. Mecozzi, O. Gennari, R. Rega, S. Grilli, **S. Bhowmick**, M. A. Gioffrè, G. Coppola, P. Ferraro
"*SPIRAL FORMATION AT MICROSCALE BY M-PYRO-ELECTROSPINNING*"
AIP Conference Proceedings 1736, 020079 (2016); Naples, Italy.

iii. **S. Bhowmick**, M. Iodice, M.A. Gioffrè, G. Breglio, M. Riccio, A. Irace, G. Romano, G. Coppola
"*PYRO-ELECTRO-THERMAL ANALYSIS OF LINBO3 USING MICROHEATERS*"
Fotonica AEIT Italian Conference on Photonics Technologies (2015), Turin, Italy.

iv. **S. Bhowmick**, O. Gennari, S. Grilli, V. Vespini, G. Gentile, V. Ambrogi, P. Cerruti, M. A. Gioffrè, C. Carfagna, P. Ferraro, S. Coppola, V. Pagliarulo, G. Coppola
"*CARBON BASED WIRES ASSEMBLING USING PYROELECTRIC EFFECT CONTROLLED BY MEANSOF TITANIUM M-HEATERS*"
1st EOS Topical metting on Optical Microsystems (OµS' 13), Capri, Italy

Contents

Acknowledgments

Introduction

The main objective of the thesis is to investigate the pyroelectric fields generated by a pyroelectric crystal (Lithium Niobate) through integrated microheater structures. Pyroelectric effect (PE) has been known for many years but it is only in the last few years that a lot of applications have been found. These applications are seen both in technology (i.e. infrared detection, imaging, thermometry, pyrometry, radiometry, etc.) and science (atomic structure of crystals, anharmonicity of lattice vibrations etc.) [1-4]. However, there are other applications that are attracting great interest, including lithography [5,6], electrohydrodynamic effect based devices [7], electron emission devices [8,9], ion source spectrometry [10,11], alignment of nano-particles under electrode-free approaches [12], nano droplet drawing [13,14]. As a result of its increasing demand in various fields, it becomes important for us to explore the pyroelectric behaviour, how it is generated and how we can apply/use in different applications.

Pyroelectricity is the ability of certain materials to generate an electrical potential in response to a temperature change. This change in temperature induces a slightly movement of the molecules within the material that changes their dipole moments. Thus, two oppositely charged faces (+Z surface and –Z surface) are created and an electrical field across the material is established. In other words, the pyroelectric effect (PE) is due to the dependence of the spontaneous polarization (Ps), the dipole moment per unit volume of the material, on the temperature. Historically, thermal stimulation tools such as: Laser, soldering iron, hot plate and peltier were used to create a variation in temperature so to generate pyroelectric effect that creates a spatial charge distribution on the surface of driving pyroelectric crystal. However, these techniques were limited, as they don't fulfil the modern world demand for lab-on chip process due to macroscopic heating tools. Other limitations in these approaches besides macroscopic heating tools were controlling and manipulating of the temperature gradients. One of the best ways to overcome the aforementioned limitations of traditional used heating sources would be by using microheater. Microheaters are small high power heaters with precise control that can offer control temperature gradients, different temperature distributions. In addition, microheaters can be easily fabricated, are cost effective, reliable and can be downsize to microscale. The study of microheaters and pyroelectric effect had already been done separately in the past. However, the investigation of amalgamation of the two: generating pyroelectric effect using microheater was unexplored until now. In this thesis work the aforementioned concept was investigated in detail way.

Here, we present a deep characterization of such microheaters (μHs) fabricated onto the surface of Z-cut pyroelectric crystal (Lithium niobate), in order to demonstrate the reliability and effectiveness of these microdevices for all of those applications where compact and low power consuming electric field sources are highly desirable. Moreover, the microscale nature of the μH allows one to stimulate the crystal locally, thus opening the route even to the development of array pyroelectric sources. The realization of these μHs was performed using semiconductor device fabrication techniques. The fabrication procedures make use of skills established in the past for a different class of applications including thermo-optical switches, chemical sensors, gas sensors, flow sensors and MEMS(Micro-Electro-mechanical system) [16-18]. Four different μH configurations are analysed here in order to investigate and exploit different temperature distributions and their effect on the pyroelectrical effect: 1) the 'meander'; 2) the 'fan'; 3) the 'spiral'; 4) the 'S-shape' [19]. Both the thermal and the electrical behaviour of the μHs were investigated theoretically and experimentally for fully understanding their operation modes and, consequently, for opening the route to new potential applications. The pyroelectric effect activated by the μH was investigated analysing the pyroelectrical current impulses detected using a micrometric metallic probe connected to an oscilloscope [20]. In particular, the temperature variation due to the μH induces a spontaneous polarization change, which produces a redistribution of the bound charges on the Lithium Niobate (LiNbO$_3$) surface. The electrical field generated between the crystal

surface and the metallic probe causes an air breakdown that appears as an impulse on the oscilloscope. Generally, when a LiNbO$_3$ crystal is heated under ambient conditions, free charges in the air will readily compensate the change in the polarization, thereby avoiding the creation of an electric field [21]. Although, when the probe is few hundreds of microns far from the crystal surface where the air acts as a thick dielectric layer and the generated electric field strength between tip and surface is greater enough for inducing an air breakdown. The pyroelectric current impulses were analysed for different μH designs and operating conditions in order to demonstrate the effectiveness of the μH as thermal tool for activating the pyroelectric effect. In particular, we validate that the threshold electric field strength required to generate the current impulses at oscilloscope is approximately 3×10^6 V/m (dielectric breakdown of air). Current impulses with larger amplitude are detected above this threshold field strength while the impulses gradually disappear below the afore-mentioned threshold. Furthermore, the PE was investigated under different humidity conditions using fan shape microheater. These investigations demonstrate that by regulating the rate of heating and cooling of the microheater, the occurrence of the PE from the surface of the LiNbO$_3$ can be manipulated and/or controlled also in different ambient conditions in an easy and efficient manner. The carried out results could be partially useful for applications that exploit the activation of a pyroelectric field between the crystal surface and non-conducting region, such as: 3D lithography [22], aligning nano particles in electrode free [12], nano-droplet drawing [13,14].

In chapter one, we briefly report on the basic concept of Pyroelectricity, its behaviour in smart material such as Lithium Niobate (LiNbO$_3$) and its general properties that make it a novel material for various applications in the field of optics, holography and biomedical applications. Then a particular focus on the pyroelectric effect of the lithium niobate crystal is presented. This effect has been widely studied to better understand its physical behaviour and also to know the influence of external parameters on it. Then a brief discussion is done on the basic heat transfer mechanics: conduction, convection and radiation that is responsible for the thermal energy. The chapter proceeds' presenting microheater as the thermal tool for inducing the pyroelectric effect on the pyroelectric crystal. Microheater can produce heat by applying an electrical current to a resistor that offers various advantages such as: low power consumption, small size, shaping of the temperature distribution and possibility of in situ control and monitoring. The joules heating effect responsible for the physical phenomenon in a microheater is further discussed. A basic introduction on the working principle for FEM software (COMSOL Multiphysics) is reported, which is adapted in order to model and design the microheater structures. At the end, device realization technologies are discussed such as: photolithography, thin film deposition and lift off process to fabricate our microheater structures on +Z surface of LiNbO$_3$ crystal surface. The preliminary activity is important to better understand the objective and also to be sure to consider all the variables properly during the modelling, designing, fabricating and characterizing of the final device.

In second chapter, microheater designs are presented and more precisely the numerical simulations that are carried out on the structures using finite element software (COMSOL™ Multiphysics). Initially, simulations were performed considering the thermal aspect of the device in stationary conditions. In the simulation stage we test the finite element software, examining the sensibility of the analysis with the boundary conditions (Joules resistive heating, natural convective heat transfer and radiated heat power) along with the meshing parameters. Evaluating the optimized parameter for the stationary condition the thermal simulation parameters in transient condition were further performed. In addition, the steady state electric field formation was further studied between the –Z surface of LiNbO$_3$ crystal and the metallic probe tip. COMSOL simulator was used to investigate the electrical field between the tip and pyroelectric crystal that depends on the electrical potential build up on the surface of the crystal in response to the temperature change. This was followed by the fabrication process steps involve in the realizations of microheaters on + Z surface of LiNbO$_3$ crystal. Furthermore, investigations were performed for the thermal and electrical properties of the thin film materials used for the microheater. Thermal and electrical conductivity of thin film materials is an important parameter to be investigated, as the performance and reliability of the devices are influence by a degree to which they

conduct heat and electricity. These properties vary from the bulk material properties. The thermal conductivity of the thin film material is lower than the bulk material due to the fact that the thermal transport of atoms is lowered as a result of the phonon scattering at lattice imperfections and boundaries. In similar way the lower value of electrical conductivity in thin film materials is due to the low mean free path of the conduction electrons due to high scattering effecting. Hence forth, the investigation were performed for the 3 choices of microheater material: Titanium (Ti), Aluminium (Al) and Indium tin Oxide (ITO) in order to obtain the appropriate thermal and electrical conductivity value for the theoretical and experimental evaluation of the micro-heater device. Emissivity and specific heat of these materials were also investigated, as they are required for numerically modelling and simulating the device.

Chapter three concerns with the device characterization through a series of experimental investigation with the aim of validating the thermal behaviour of device both in static and transient conditions. FLIR SC700 infrared camera is used to carry out the experimental thermal measurements. The aim was to better understand the effective thermal distribution on the -Z surface of the crystal using the different microheater structures. A comparison between the numerical and experimental data is presented to validate the models. Moreover using the statistics methods it has been possible to evaluate the efficiency of the approach taken into considerations and also the correspondence between experimental and finite element analysis. Furthermore, evaluation of the electric field analysis was analysed taken into consideration two major factors: 1) at constant tip to –Z surface gap of 100 µm for different designs of microheaters and 2) at different tip to –Z surface gap for the fan shape microheater. The thermal and electrical behaviour of the device investigation theoretically provides an advantage of understanding their modes of operations and consequently a perception of the further experimental results.

In chapter four, the pyroelectric effect activated by the microheaters was investigated analysing the pyroelectrical current impulses detected using a micrometric metallic probe connected to an oscilloscope. The electrical field generated between the crystal surface and the metallic probe causes an air breakdown that appears as an impulse on the oscilloscope. In particular we validate that the threshold electric field strength required to generate the current impulses at oscilloscope is approximately 3×10^6 [V/m] (dielectric breakdown of air). In addition, investigations were also performed for the pyroelectric effect from the –Z surface of the $LiNbO_3$ crystal varying the tip to surface gap spacing, initial current impulse occurrence at oscilloscope and the temporal distance between the impulses. Furthermore, Pyroelectric effect (PE) under humidity conditions from the –Z surface of the Lithium Niobate ($LiNbO_3$) crystal was investigated using fan shape µHs fabricated on the +Z surface of the crystal. Resistive Aluminium (Al) sensors was integrated along the µH in order to control the temperature variation effect from the microheater. The reported results demonstrate that by regulating the rate of change of heating and cooling of the different microheaters, the occurrence of the pyroelectric effect from the –Z surface of the $LiNbO_3$ can be manipulated and /or controlled in an easy and efficient manner compared with the traditional ways of thermalizing the crystal.

In chapter five, we reported on the various applications performed in collaboration with other groups taking the advantage of PE using integrated microheater structure. We first report on the dispensing of micro-nano liquid droplets as it is important in the field of biotechnology and combinational chemistry. Several methods for dispensing liquid exist, but many required complicated electrode and high voltages circuits. Here, we show, in collaboration with the ISASI's group, a simple way to draw nano-pico litter's liquid droplets from one or multiple sessile drops or liquid film reservoirs using pyroelectrohydrodynamic (PED) dispenser induced by $LiNbO_3$ using integrated fan shape microheater. Local pyroelectric forces, which are activated by using microheater fabricated on lithium niobate substrate, draw liquid droplets from the reservoir below substrate, and deposit then on the underside of the lithium niobate substrate.

Another interesting application, the realization of an optimized micro-heaters array in order to control the heat distribution over a large area about 1.25×1.25 cm^2, on lithium niobate (LiNbO$_3$) crystal. The optimized device will provide us with several benefits, as the possibility of producing microneedles array with high uniformity in shape and height, in specific and relative wide area, with high accuracy. The methodology we pursued, in collaboration with the IIT's group, to obtain the above aforementioned requirement of producing microneedles consists of three fundamental and sequential steps: design, fabrication and characterization.

We also report, in collaboration with the ISASI's group, on an innovative version of electro-spinning (ES) that we call micro-pyro-electrospinning (μ-PES) by controlling the electric field generated pyroelectrically by integrated fan microheater. The pyro-electrohydrodynamic process activated in this way can be used to manipulate soft matter and is able to generate true spiral patterns at microscale by a direct process.

Finally, in conclusion we discuss on the performed deep investigation of the pyroelectric effect induced into lithium niobate by microheater structures integrated directly onto the surface of the crystals. In particular, the main results are summarized. The reported results let us to claim that by regulating the rate of heating or cooling of the different design of microheaters, the occurrence of the pyroelectric effect from the –Z surface of the LiNbO$_3$ can be manipulated and/or controlled is an easy and efficient manner compared with traditional ways of thermalizing the crystal.

Reference:

1) Coates, P. B. (1981). Multi-wavelength pyrometry. *Metrologia , 17*, 3.
2) Fujitsuka, N., Sakata, J., Miyachi, Y., Mizuno, K., Ohtsuka, K., Taga, Y., Tabata, O. (1998). Monolithic pyroelectric infrared image sensor using PVDF thin film. *Sensor and Actuators A:Physical , 66* (1-3), 237-243.
3) Lang, S. B. (2005, august). Pyroelectricity: From ancient curiosity to modern imaging tool. *Physics Today , 31-36.
4) Lehman, J., Eppeldauer, G., Aust, J. A., Racz, M. (1999). Domain-engineered pyroelectric radiometer. *Applied Optics , 38* (34), 7047-7055.
5) Kim, D. W., Moon, C. W., and Yoo, I. K. (2003). Pyroelectric Emission Lithography. *Journal of the Korean Physical Society , 42*, s1196-s1198.
6) Moon, C. W., Kim, D.-W., Rosenman, G., Ko, T. K., and Yoo, I. K. (2003). Patterned Pyroelectric Electron Emitters and their Feasibility Study for Lithography Applications. *Japanese Journal of Applied Physics , 42*, 3523.
7) Coppola, S., Vespini, V., Grilli, S., and Ferraro, P. (2011). Self-assembling of multi-jets by pyro-electrohydrodynamic effect for high throughput liquid nanodrops transfer. *Lab on a Chip , 11*, 3294-3298.
8) Rosenman, G., Shur, D., and Skliar, A. (1996). Ferroelectric electron emission flat panel display. *Journal of applied physics , 79*, 7401.
9) N. Balcon, D. Payan, M. Belhaj, T. Tondu and V. Inguimbert, "Secondary Electron Emission on Space Materials: Evaluation of the Total Secondary Electron Yield From Surface Potential Measurements," in *IEEE Transactions on Plasma Science*, vol. 40, no. 2, pp. 282-290, Feb. 2012. doi: 10.1109/TPS.2011.2172636
10) Neidholdt, L. E., and Beauchamp, L. J. (2007). Compact ambient pressure pyroelectric ion source for mass spectrometry. *Analytical chemistry , 79*, 3945-3948.
11) Neidholdt, E. L., and Beauchamp, J. L. (2009). Ionization mechanism of the ambient pressure pyroelectric ion source (APPIS) and its applications to chemical nerve agent detection. *J Am Soc Mass Spectrom , 20*, 2093-2099.
12) Gennari, O., Grilli, S., Coppola, S., Pagliarulo, V., Vespini, V., Coppola, G., Bhowmick, S., Gioffré, M.A., Gentile, G., Ambrogi, V., Cerruti, C., Carfagna, C., Ferraro, P. (2013). Spontaneous assembly of carbon-based chains in polymer matrix through surface charge templates. *Langumir , 29*, 15503-15510.
13) Ferraro P., Coppola S., Grilli S., Paturzo M. and Vespini V. (2010). Dispensing nano–pico droplets and liquid patterning by pyroelectrodynamic shooting. *Nature Nanotechnology*, 5, 429–435, doi: 10.1038/nnano.2010.82.
14) Vespini, V., Coppola, S., Grilli, S., Paturzo, M., and Ferraro, P. (2013). Milking liquid nano-droplets by an IR laser: a new modality for the visualization of electric field. *Meas. Sci. Technol.,* 24 045203, doi: 10.1088/0957-0233/24/4/045203.
15) Mecozzi, L., Gennari, O., Rega, R., Grilli,S., Bhowmick, S., Gioffrè,M.A., Coppola, G., Ferraro,P. (2016). *Spiral formation at the microscale by μ-pyro-electrospinning.* Soft matter, DOI: 10.1039/c6sm00156d
16) Coppola, G., Sirleto, L., Rendina, I., and Iodice, M. (2011). Advance in thermo-optical switches: principles, materials, design, and device structure. *Opt. Eng.*, 50(7), 071112.
17) Chul ha, S., Kim, Y. S., Yang, Y., Kim, Y. J., Cho, S.M., Yang, H., Kim, Y.T. (2005). Integrated and Micro-Heater embedded gas sensor array based on the polymer composites dispensed in micromachined wells. *Sensors and Actuators B:Chemical , 105* (2), 549-555.
18) Neda, T., Nakamura, K., and Takumi, T. (1996). A polysilicon flow sensor for gas flow meters. *Sensor and actuators A: Physical , 54* (1-3), 626-631.
19) Velmathi, G., Ramshanker, N., and Mohan, S. (2010). 2D simulations and electro-thermal analysis of Micro-Heater design using COMSOL for gas sensor applications. *COMSOL conference,* India.

20) Bhowmick, S., Iodice, M., Gioffre', M., Riccio, M., Irace, A., Romano, G., Coppola, G., (2015). Pyro- Electro-Thermal Analysis of LiNbO3, using Microheaters. *Fotonica AEIT Italian Conference on Photonics Technologies, Turin*. DOI:10.1049/cp.2015.0129

21) Rosenman, G., Shur, D., Krasik, Y., and Dunaevsky, A. (2000). Electron emission from ferroelectrics. *Journal of Applied physics , 88*, 6109.

22) Grilli, S., Coppola, S., Vespini, V., Merola, F., Finizio, A., Ferraro, P. *(2011)*. 3D lithography by freezing liquid instabilities at nanosclae. *PNAS,* 108-15106.

Chapter 1
Basic Concept and Theoretical Background

1.1 What is Pyro-electricity?

Pyro-electricity is the ability of certain materials to generate an electrical potential in response to a temperature change. A pyroelectric solid exhibits a change in spontaneous polarization as a function of temperature. The relationship between the change in temperature ΔT, and the change in spontaneous polarization ΔP_s, is linear and can be written as $\Delta p_s = \bar{p}.\Delta T$ where p is the pyroelectric tensor. In tensor component form this maybe written as $\Delta Ps_i = p_i \cdot \Delta T$. In pyroelectric materials such as Lithium Niobate (LiNbO₃) the effect is due to the movement of the lithium and niobium ions relative to the oxygen layers.
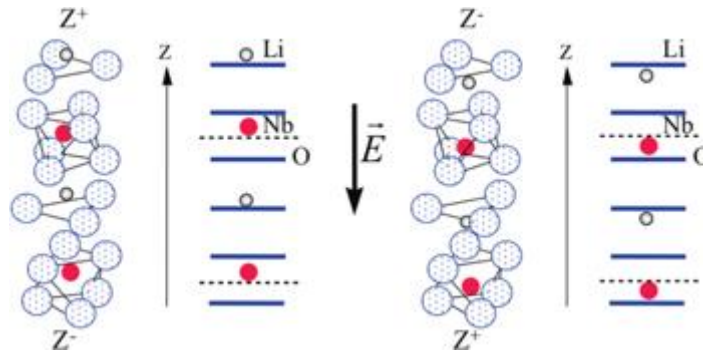
Fig1: Crystalline structure of lithium niobate. [1]

The small red and white circles are the niobium and lithium atoms, respectively. In Fig 1 (left hand side), the ions are shifted above the oxygen planes inducing a positive spontaneous polarization with an electric field along the +z-axis. Applying a negative electric field ($\vec{E}$ in the centre of figure 1) during the fabrication permanently shifts the niobium and lithium atoms below the oxygen planes, therefore inverting the direction of the crystal's spontaneous polarization. Since the Li and Nb ions move only in a direction parallel to the z-axis (trigonal axis), the pyroelectric tensor is of the form:

$$p_i = \begin{bmatrix} 0 \\ 0 \\ p_3 \end{bmatrix}$$

Where, $p_3 = -4 \cdot 10^{-5} [C/K \cdot m^2]$. Note that negative value of p_3 indicates, that upon cooling, the +Z crystal face will become more positively charged. Thus, two oppositely charged faces are created and an electrical field across the material is established. In other words, the pyroelectric effect is due to the dependence of the spontaneous polarization (P_S), the dipole moment per unit volume of the material, on the temperature. It follows that the pyroelectric current is proportional to the rate of polarization change with temperature known as the pyroelectric coefficient p_3, the area A_d (in which the pyroelectric current is detected)and the rate of temperature variation (dΔT_d/dt) within the crystal, as shown in the equation:

$$I_{pyro} = \frac{dPs}{dT} \cdot \frac{d\Delta T_d}{dt} \cdot A_d = p_3 \cdot A_d \cdot \frac{d\Delta T_d}{dt} \tag{1}$$

Pyroelectrically induced electron emission is generally due to the perturbation, by temperature variation, of equilibrium between spontaneous polarization P_S in the crystal and the external screening charges (σ_{sc}) on the crystal surfaces. At equilibrium, all P_S are fully screened by σ_{sc} and no electric field exists. Any excess or lack of screening charges (σ_{sc}), relatively to P_S, leads to the appearance of an electrostatic state from the uncompensated charges:

$$\rho = \Delta(P_s - \sigma_{SC}) \tag{2}$$

Which generate a high electric field at the crystal surface, as large as (10^6–10^8 V/cm), able to cause pyroelectric electron emission (PEE) by field emission (FE) and/or field ionization (FI) effects.
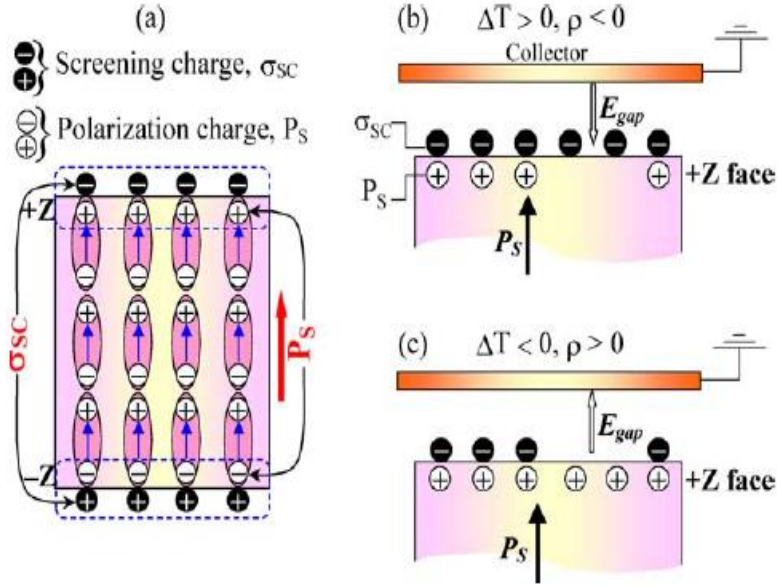
Fig2: Schematic diagram of the electrostatic state evolution of uncompensated charge (p) with the temperature on +Z face surface of a mono domain pyroelectric crystal [2].

The uncompensated charges are limited by the temperature variation of the +Z face LiNbO$_3$ crystal. Using the equation (2), three conditions can be elaborated for the flow of uncompensated charges dependence with the temperature from the –Z surface of LiNbO$_3$ crystal.

At the equilibrium state $\sigma_{SC} = P_S$ i.e. at room temperature ΔT

$$q = \Delta(P_s - \sigma_{sc}) = 0 \tag{3(a)}$$

Hence, no electric field E on the crystal surface is observed.

At $\Delta T > 0$, $\sigma_{SC} > P_S$

$$q = \Delta(P_s - \sigma_{sc}) < 0 \tag{3(b)}$$

Implying the uncompensated charges of q_{sc} is the source of electric field E on the Crystal surface.

At $\Delta T < 0$, $\sigma_{SC} < P_S$

$$q = \Delta(P_s - \sigma_{sc}) > 0 \tag{3(c)}$$

Pyroelectrically induced electron emission (PEE) is observed when the pyroelectric crystal is heated. Screening electrons are released from the surface when the spontaneous polarization decreases in the course of heating. In figure 3, we observe the different possible cases of electrical charge emission, which could take place in the gaps form both sides of pyroelectric crystal surfaces (+Z and –Z faces), independently of the consideration of

the experimental conditions (ambient pressure, gap distance, set up geometry), material parameters (conductivity, pyroelectric coefficient, work function) and so on.
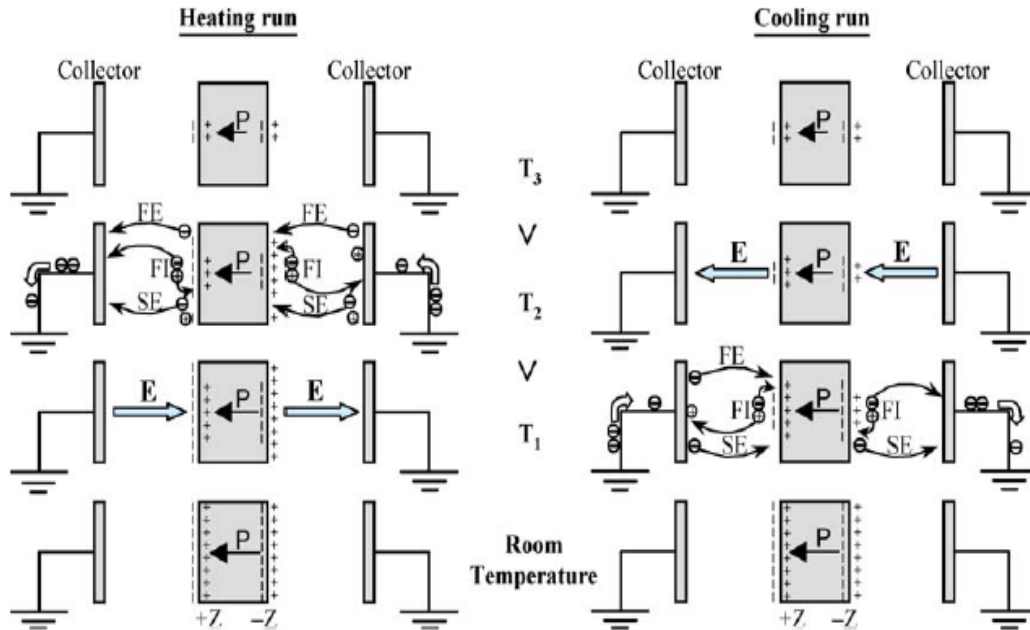
Fig 3: Sketch scenarios of electrical emission sources originated from different effect (FE: Field emission, FI: Field ionization, SE: secondary electron emission) activated by spontaneous polarization PS change with temperature of the pyroelectric crystal [2].

When a pyroelectric crystal heats up from room temperature (RT) to a higher temperature, the decrease of spontaneous polarization P_S lets appear uncompensated charges of screening charges (σ_{SC}) on the crystal surfaces (electrons on +Z face and positive charges on –Z face), thus pyroelectric fields are built up in both sides of the crystal. In +Z face side and –Z face side both mechanisms Field Emission (FE) and/or Field Ionization (FI) could take place. Therefore, in the gap +Z face side the released electrons are accelerated towards the collector and positive ions towards the crystal surface, whereas in the gap –Z face side, because species (electrons/+ions) take to drift in the opposite way, the ions are accelerated towards the collector and the electrons towards the crystal surface. From such scenarios the electron emission current could be measured only from +Z face and during heating.

When the pyroelectric crystal cools down to RT, the rise of the spontaneous polarization lets emerge the polarization charges (P_S) in the crystal surfaces. When these ones are un-compensated, they induce a pyroelectric field in each crystal side. Thereby, FE and/or FI could take place in the gap +Z face side. But in the –Z face side only the FI and its consequent SE could be involved because the polarization charges (P_S) are embedded in the crystal surface and do not leave the crystal under any external field influence. Therefore, in the gap +Z face side the electrons are accelerated towards crystal surface and positive ions towards the collector, whereas in the gap –Z face side the drift of species (electrons/+ions) is effectuated in opposite directions. From such scenarios the electron emission could be measured only from –Z face and during cooling.

Lithium Niobate (LiNbO$_3$) is one of the well know and widely used pyroelectric crystal for investigating and studying the pyroelectric effect. Its general properties makes it a novel material for various applications in field of optics, holography and biomedical devices.

3

1.2 Pyroelectric crystal (Lithium Niobate)

Smart materials are different from the usual materials as they can sense the environment and respond, in the flexibility of their properties that can be significantly altered in a controlled fashion by external stimuli, such as stress, temperature, electric and magnetic fields (see fig 4.). The most widely used smart materials are piezoelectric ceramics, which expand or contract when an electric field is applied. Pyroelectric material is a kind of smart materials and can be electrically polarized by means of temperature variation.
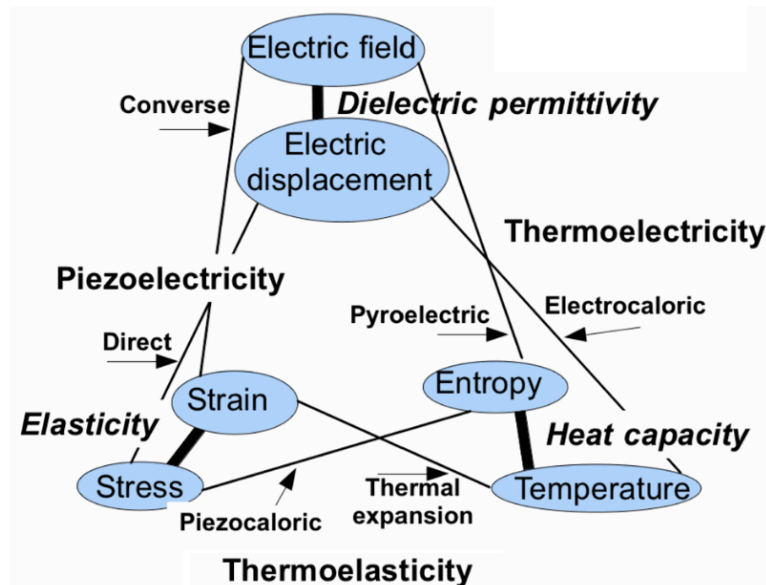
Fig 4: Interconnection between piezoelectricity, Pyroelectricity and thermoelectricity.

Lithium niobate is one of the most used crystalline dielectric materials at the present days. As the compound presents a very interesting combination of properties and characteristics that makes it possible to tailor its behaviour for numerous applications and fabricate several useful devices. The basic material properties of lithium niobate are by themselves very promising. The material can be grown in quite large crystals by the use of artificial techniques. The most extended method to grow single crystals of this compound, the Czochralski method and its variants, permits the fabrication of very homogeneous crystal even of several kilograms and more than three inches in diameter [3, 4]. Then, this is a relatively non-expensive starting material for devices. Most common lithium niobate crystals present a large concentration of intrinsic defects. Moreover, these crystals can be also doped with few amounts of suitable different impurities. The control of both intrinsic point defects and impurities offers a wide range of variation in material characteristics. Another important factor to be considered from the practical aspect in this overview of the material is the possibility of producing different sample structures. Bulk, fibres and thin films that have to be completed with surface waveguide structures, non-equivalent crystallographic orientations and ferroelectric domain structures. This exceptional situation provides the frame for many present and future uses in quite different physical branches. Lithium niobate in its crystalline form is a solid material chemically very stable at room temperature and quite insensitive to humid surroundings. It is a compound of niobium, lithium, and oxygen ($LiNbO_3$). The material is ferroelectric below a very high Curie temperature ($T_C \sim 1150$ °C). Ferroelectric domains with 180° orientations are present in the samples.
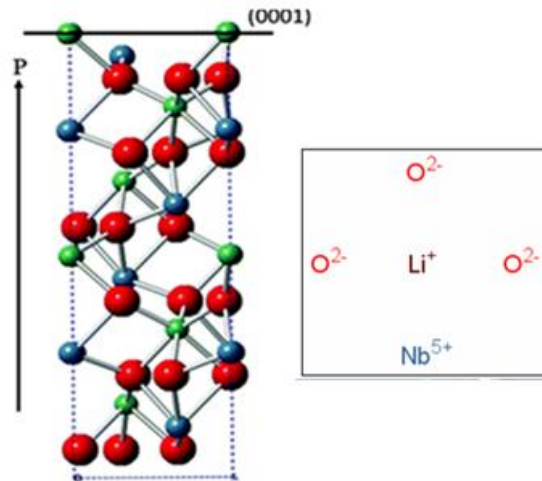
Fig 5: Schematic of the structure of lithium niobate with direction of polarization. [3]

The crystalline structure of this material at room temperature corresponds to the trigonal 3m-point group. This makes the crystal to be optically uniaxial, with two refractive indices n_e and n_o. Both indices have values exceeding of 2 in all the transparency region, which makes in many cases necessary to fit anti-reflecting coating layers on the optical surfaces. The pure (and not reduced) material is transparent from the band gap edge absorption at about 320 nm (~3.9 eV) up to the first infrared vibrational absorptions at a wavelength of about 5 μm (0.25 eV), covering all the visible and near infrared spectral regions. Table I shows the other physical properties of Lithium Niobate.

Parameters	Lithium Niobate (LiNbO$_3$)
Density (rho)	4.644 [g/cm^3]
Heat capacity at constant pressure (C_p)	89[J/kmol]
Thermal conductivity (k)	5.6 [W/m.K]
Thermal expansion α_a (perpendicular) α_c (parallel)	[1/K] 15×10^{-6} 5×10^{-6}
Specific heat	0.15 [cal/g.K]
Dielectric constant	85

Table I: Physical properties of Lithium Niobate [4].

The general properties of Lithium Niobate crystal make it a novel material for various applications in the field of optics, holography and biomedical devices. In addition, the pyroelectric behaviour of the crystal makes it a suitable smart material for devices that can measure the power generated by radiations sources such as: pyrometry, infrared imaging and radiometry [6-9]. However, there are other applications that are growing in importance; such as: lithography [10-11], electro-hydrodynamic effect based devices [12], electron emission devices [13-14], ion source spectrometry [15-16], aligning nano-particles in electrode free approach [17], nano-droplet drawing [18-20].

In a nutshell, the pyroelectric effect of the LiNbO$_3$ crystal is activated as a result of change in temperature. This change in temperature moves positive and negative charges to opposite ends through migration (i.e. the material becomes polarised) and hence an electrical potential is established. This shows the importance of understanding the heat transfer's behaviour due to conduction, convection and radiation that result in the pyroelectric effect in the LiNbO$_3$ crystal.

1.3   Heat transfer (The mechanism of heat transfer)

Heat transfer is a process of energy transfer from one body or system due to thermal contact and temperature gradient or differences. Heat transfer is considered to be the dynamic form of energy whereas internal energy is considered as static quantity [21]. The internal energy in system is due to the molecular structure and the degree of molecular activities, and they can be viewed as the sum of kinetic and potential energies of the molecules. The total energy can be decomposed in two components: one which is directly proportional to the temperature of the body or system, another the absorption or releases of energy during the phase change that occurs without changing temperature. The latter part is generally known as latent energy as just monitoring temperature such as condensation of water vapour or melting ice cannot sense it.

Temperature of a body is a measure of its average energy of motion or kinetic energy of particles in matter. When the particles move in slower or have lower mass, whether in sol-ids, liquids or gases, they carry fewer kinetic energy and the body seems cooler than a body with faster particles motion or higher mass. Heat always flows from higher temperature body to a lower temperature body [21]. There are 3 basic modes of heat transfer: heat conduction, heat convection and thermal radiation (see fig 6)
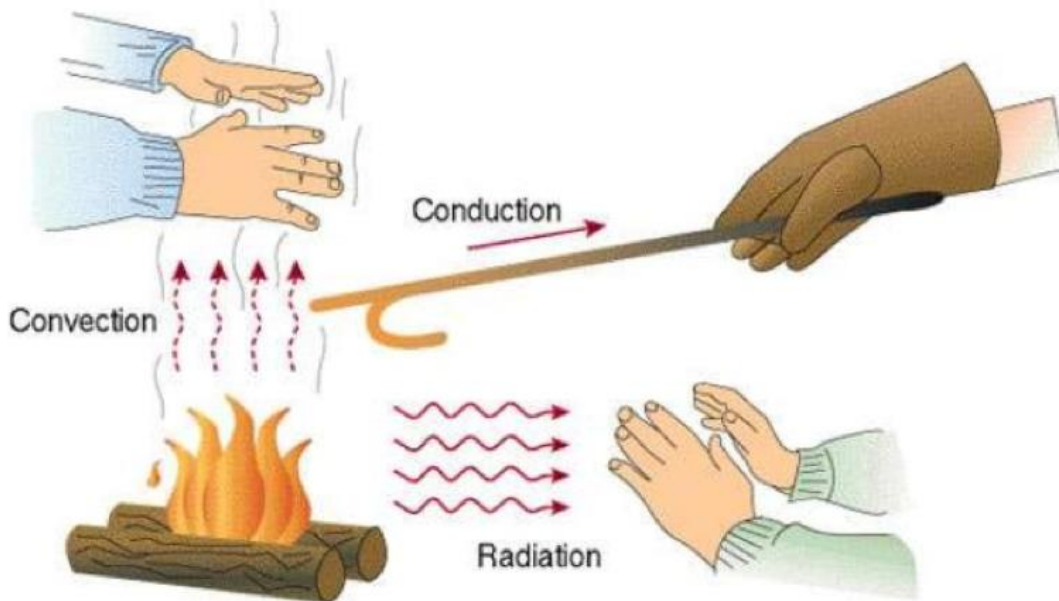
Fig 6: Different modes of heat transfers (image courtesy).

1.3.1   Conduction

Conduction is the transfer of heat through matter due to change in temperature or temperature gradient. It exists in solids, liquids and gases that do not involve any bulk motion of matter. Fourier's law of heat conduction is the governing law for the heat conduction at macroscopic level [21]. In a 1D, the heat transfer Q through a surface area of A along the length ΔL due to temperature difference ΔT is given by:

$$Q = \kappa.A.{^{\Delta T}/_{\Delta L}} \tag{4}$$

Where, κ the constant of proportionality is known as thermal conductivity. It is a temperature dependent property of the material. High thermal conductivity materials are used for cooling devices such as heat sink as they releases heat by conduction. Generally, a good conductor of electricity is considered to be a good conductor too. In the **Table II** below, shows the thermal conductivity of different classes of materials: fluids, polymers, metals, wood and glass.

Materials	κ [W m-1 K-1]	Materials	κ [W m-1 K-1]
Air	0.027	LiNbO$_3$	5.6
PVC	0.092	Mercury	8.4
Engine oil	0.145	Aluminum	204
Water	0.611	Copper	386
Pyrex glass	1.09	Silver	429

Table II: Thermal conductivity of few materials at 300K [4,22].

1.3.2 Convection

The convection heat transfer mode compose of two mechanisms: 1) the energy transfer due to random molecular motion, 2) energy transferred by motion of fluid. In the motion of fluid situation, large numbers of molecules are considered to be moving collectively or as aggregates. Under the presence of temperature gradient, this kind of motion contributes in the heat transfer. Since the molecules in the aggregate retain their random motion, the total heat transfer is then due to a superposition of energy transport by the random motion of the molecules and by the bulk motion of the fluid. Generally, the term convection is referred in this cumulative transport and the term advection when referred to transport due to bulk fluid motion.

Convection heat transfer may be classified according to the nature of the flow. We speak of forced convection when the flow is caused by external means, such as by a fan, a pump, or atmospheric winds. In contrast, for free (or natural) convection, the flow is induced by buoyancy forces, which are due to density differences caused by temperature variations in the fluid. While we have presumed pure forced convection and pure natural convection, conditions corresponding to mixed (combined) forced and natural convection may exist. In this case, the buoyancy-induced flow would be normal to the forced flow and could have a significant effect on convection heat transfer from the components. Regardless of the nature of the convection heat transfer process, the appropriate rate equation is of the form:

$$q = h \, (T_s - T_\infty) \tag{5}$$

Where q, the convective heat flux [W/m^2], is proportional to the difference between the surface and fluid temperatures, T_s and T_∞, respectively. This expression is known as Newton's law of cooling, and the parameter h [W/m^2·K] is termed the convection heat transfer coefficient. This coefficient depends on conditions in the boundary layer, which are influenced by surface geometry (orientation of the surface: vertically or horizontally), the nature of the fluid motion, and an assortment of fluid thermodynamic and transport properties. When Equation (5) is used, the convection heat flux is presumed to be positive if heat is transferred from the surface ($T_s > T_\infty$) and negative if heat is transferred to the surface ($T_\infty > T_s$). However, nothing precludes us from expressing Newton's law of cooling in which case heat transfer is positive if it is to the surface.

$$q = h \, (T_\infty - T_s) \tag{6}$$

Calculating the heat transfer coefficient (h)

The heat transfer coefficient h is evaluated by calculating the Nusselt Number (Nu). The Nusselt number is generally given as a function of Rayleigh number, which in turn depends on the geometry of the model.

$$Nu = hLc/ka \tag{7}$$

Where, ka is the thermal conductivity of fluid (air). For a vertical oriented surface Lc is the height of the plate while in the horizontally oriented surface it is given by the ratio of area (area of the plate surface) and perimeter (see fig 7).
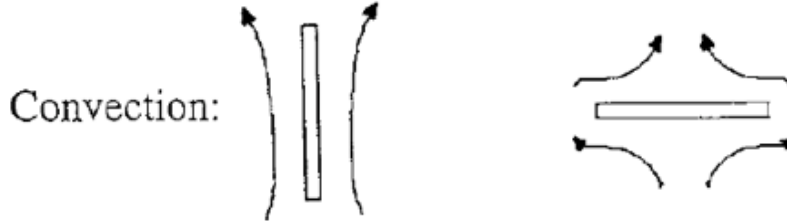
Fig 7: Schematic diagram indicating the thermal dissipation by convective process for vertical and horizontal surface [23].

Using the Nusselt number, we calculate the heat transfer coefficient h and thus calculate the power dissipated per unit area. For laminar flow, the Nusselt number generally given as [23],

Vertical surface [23]:

$$Ra < 10^9: Nu = 0.68 + 0.67R\,a^{\frac{1}{4}} \Big/ \left(1 + \left(\tfrac{0.49}{Pr}\right)^{\frac{9}{16}}\right)^{\frac{4}{9}} \tag{8(a)}$$

$$Ra > 10^9: Nu = 0.1Ra^{\frac{1}{3}} \tag{8(b)}$$

$$10^5 < Ra < 10^9: Nu = 0.59Ra^{\frac{1}{4}} \tag{8(c)}$$

Horizontal surface [23]:

$$Ra < 200: Nu = 0.96Ra^{\frac{1}{6}} \tag{9(a)}$$

$$200 < Ra < 10^7: Nu = 0.54Ra^{\frac{1}{4}} \tag{9(b)}$$

$$10^7 < Ra < 3*10^{10}: Nu = 0.15Ra^{\frac{1}{3}} \tag{9(c)}$$

The Rayleigh Number (Ra), which itself is the product of two dimensionless quantities, the Grashof number and Pandtl number [23].

$$Ra = GrPr \tag{10}$$

$$Gr = g\beta\rho^2 Lc^3 \Delta T/\mu^2 \tag{11}$$

$$Pr = \mu Cp/ka \tag{12}$$

Where, β, ρ, μ, Cp are the thermal expansion coefficient (= 3.3×10^{-3} [K^{-1}]), density (1.18×10^{-3} [g/cm^3]), viscosity (2.16×10^{-4} [g/cm-s]), heat capacity (1.02 [J/g-K]) and g is the gravitational constant.

Note:

1) A MATLAB function is defined to evaluate the heat transfer coefficient. (Appendix A.3.1).

1.3.3 Radiation

Thermal motion of charged particles in matter causes to emit thermal radiations from matter. The radiant energy emitted from the surface of a body depends on 3 main factors: surface temperature T, surface area A, emissivity of material ε and it is define by Stefan-Boltzmann law:

$$E = \varepsilon \, A \, \sigma \, T^4 \tag{13}$$

Where σ is Stefan- Boltzmann constant (5.67×10^{-8} [W m^{-2} K^{-4}]), while ε is a radiated property of the surface of the body. The values in the range of $0 \leq \varepsilon \leq 1$, shows the emission property of the body with respect to an ideal blackbody (i.e. 1). It depends strongly on the surface material and finish. Radiation may also be incident on a surface from its surroundings. The radiation may originate from a special source, such as the sun, or from other surfaces to which the surface of interest is exposed. Irrespective of the source(s), we designate the rate at which all such radiation is incident on a unit area of the surface as the irradiation G (Figure 8a).
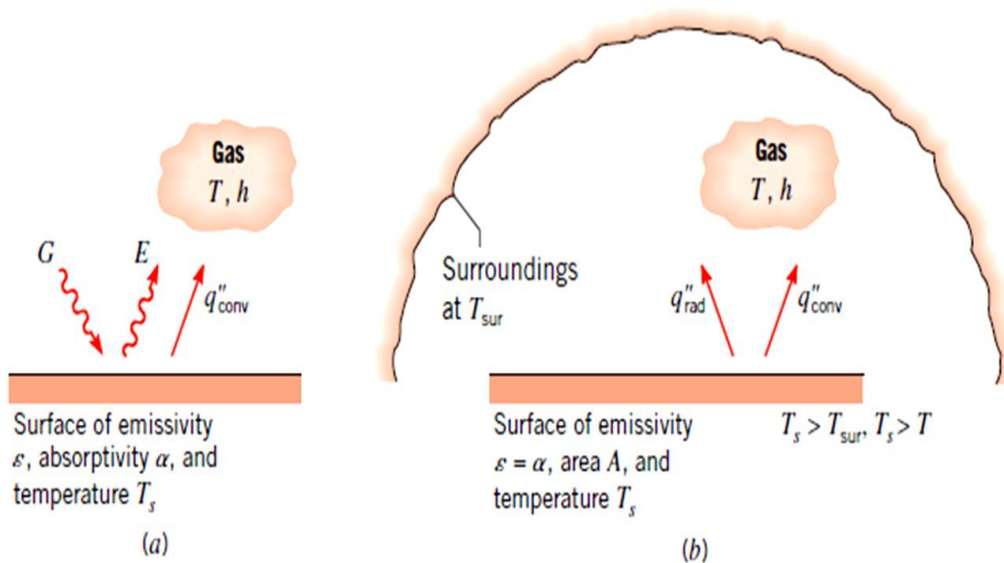
Fig 8: radiation exchange: a) at a surface, b) between a surface and large surroundings.

A portion, or all, of the irradiation may be absorbed by the surface, thereby increasing the thermal energy of the material. The rate at which radiant energy is absorbed per unit surface area may be evaluated from knowledge of a surface radiative property termed the absorptivity α.

$$G_{abs} = \alpha G \tag{14}$$

Where $0 \leq \alpha \leq 1$. If the surface is opaque, portions of the irradiation are reflected. If the surface is semi-transparent, portions of the irradiation may also be transmitted. However, whereas absorbed and emitted radiation increase and reduce, respectively, the thermal energy of matter, reflected and transmitted radiation have no effect on this energy. Note that the value of α depends on the nature of the irradiation, as well as on the surface itself. For example, the absorptivity of a surface to solar radiation may differ from its absorptivity

to radiation emitted by the walls of a furnace. In many engineering problems (a notable exception being problems involving solar radiation or radiation from other very high temperature sources), liquids can be considered opaque to radiation heat transfer, and gases can be considered transparent to it. Solids can be opaque (as is the case for metals) or semi-transparent (as is the case for thin sheets of some polymers and some semiconductor materials).

A special case that occurs frequently involves radiation exchange between a small surface at T_s and a much larger, isothermal surface that completely surrounds the smaller one (Figure 8b). The surroundings could, for example, be the walls of a room or a furnace whose temperature T_{sur} differs from that of an enclosed surface $T_{sur} \neq T_s$. For such a condition, the irradiation may be approximated by emission from a blackbody at T_{sur}, in which case $G = \sigma T_{sur}^4$. If the surface is assumed to be one for which $\alpha = \varepsilon$ (a grey surface), the net rate of radiation heat transfer from the surface, expressed per unit area of the surface:

$$q_{rad} = \frac{Q}{A} = \varepsilon E_b(T_s) - \alpha G = \varepsilon \sigma (T_s^4 - T_{sur}^4) \qquad (15)$$

Where q_{rad} is expressed in [W/m^2]. This expression provides the difference between thermal energy that is released due to radiation emission and that gained due to radiation absorption. The heat flux of heat transfer radiant is seen as the electromagnetic waves or photons. The above process of heat transfer can be done through the traditional manmade methods such as: hot plate, laser, soldering iron and peltiers. However, these approaches are expensive, cumbersome, high power consuming and they don't fulfil the modern world demand of lab-on chip process due to their macroscopic size. Other limitations in these approaches besides macroscopic heating tools were controlling and manipulating of the temperature gradients. In order to overcome these disadvantages, we use microheaters as thermal tool.

1.4   Microheaters (μHs)

Microheaters are microscale high power heaters with precise control that offer temperatures. Microheaters have gained a lot of interested over the past decades, as they are the major components in micro-sensors technologies such as humidity sensors, thermo optical switches, chemical sensors, flow sensors and gas sensors [24-28].   Microheaters are employed to provide the desired operating conditions or to simulate and/or compensate for some specific external conditions [29-30]. A Microheaters that can produce heat by applying an electrical current to ta resistor, offers various advantages such as: low power consumption, small size, shaping of the temperature distribution and possibility of in situ control and monitoring. In the real world, resistive heaters are very suitable for most of the applications as they are reliable and simple to realize in a broad set of well-established micro-fabrication processes. μHs can also be employed to replace the heat source in devices and systems when it's too complex, macroscopic, cumbersome, heavy, power consuming and/ or expensive to use other types of heaters such as: laser beam, hot plate, soldering iron rod). Microheater can achieve a temperature differences by integrated on-chip heaters from low (fractions of 1^0C) to very high (hundreds or thousands of ^{0}C). A common characteristic to most of the employed microheaters is fast response time (order of μs- ms) and reduces power consumption, due to the small mass and optimized geometry to minimize thermal losses.

Microheaters are devices that generate heat due to electric current's flow, according to Joule's effect heating law. Wire heaters and thin film heaters are two main kinds of microheaters. A MEMS-based thin film heater has more interesting applications than a wire heater due to its lower heat mass, ease of integration and compatibility with other MEMS-based devices. The general requirements for a thin film micro-heater are low power consumption, fast response, good heat confinement, good mechanical stability, good fabrication yield, shaping of the temperature distribution and possibility of in situ control and monitoring. Moreover, the miniaturization of a micro-heater can avoid heating of the en-tire host substrate, so enabling the possibility of array configuration. Heavily p-doped silicon was initially used for the micro-heater material because of its

excellent mechanical properties Nevertheless; this kind of micro-heater shows some limitations due to its relatively high power consumption. To improve the micro-heater performances, many recent studies employ dielectric membranes to assure lower power consumption. Dielectric membranes do provide improvement in terms of micro-heater power consumption. However, they could be less reliable for some applications in harsh environments.

In this thesis work, deep characterizations of four different µH designs are being investigated. In Fig 9, the schematic of the microheaters structures adapted is shown.
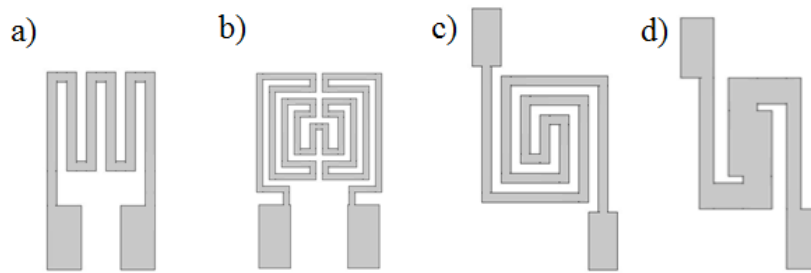
Fig 9: Schematic of adapted microheater designs for the thesis work: a) Meander, b) Fan, c) Spiral, d) S-shape.

Titanium (Ti) is used as the microheater material for each of the structures. Titanium thin film (300nm-thick) has an ideal value of electrical resistivity for our applications. This property lets low drive voltage use for heat generation. Titanium also has a good melting point value, in contrast with other similar metals like gold (Au), copper (Cu) or aluminium (Al), that are low-melting. Its other properties are key elements in terms of stability, adherence on lithium niobate surface and thermal expansion in our range of temperature. It has a low density and remains resistant to the corrosion in various conditions due to the thin layer of oxide, which forms on its surface. The fabrication process is much easier and fabrication yield is much higher than the realization of dielectric membrane-based microheaters.

For thin film microheater, modelling is a good way to predict its performance, especially its detailed temperature profile. Unfortunately, the thin film material properties are seldom discussed in detail, although they are essential for micro-heater design and performance prediction. The temperature variations of thin film material electrical resistivity and thermal conductivity are often ignored. It should be noted that these are the key material properties required for any thin film based microheater modelling. Furthermore, some important modelling techniques and experimental procedures, such as meshing strategy, grid-independent study, calibration and testing procedures, are sometimes missing. These are very useful for understanding the modelling and experiment accuracy. Modelling of microheater involves multiple coupling physics. The physical phenomenon experienced in a microheater is that of joule heating. Joule heating consists of electric currents and heat transfer.

1.5   Joules heating

In Joule heating, the temperature increases due to the resistive heating from the electric current. The generated resistive heat Q is proportional to the square of the magnitude of the electric current density J. Current density, in turn, is proportional to the electric field, which equals the negative of the gradient of the potential V:

$$Q \propto |J|^2 \qquad\qquad (16)$$

Where, Q is expressed in [W/m³] and J in [A/m²]. The coefficient of proportionality is the electric resistivity ρ = 1/σ [Ω·m], which is also the reciprocal of the temperature-dependent electric conductivity σ = σ(T) [S/m]. Combining these facts gives the fully coupled relation:

$$Q = \frac{1}{\sigma}|J|^2 = \frac{1}{\sigma}|\sigma E|^2 = \sigma|\nabla V|^2 \qquad (17)$$

Where, E is the electric field expressed in [V/m] and the voltage V is in [V]. Over a range of temperatures, the electric conductivity σ is a function of temperature T according to:

$$\sigma = \frac{\sigma_0}{1+\alpha(T-T_0)} \qquad (18)$$

Where, σ_0 is the conductivity at the reference temperature T_0 and α is the temperature coefficient of resistivity, which describes how the resistivity varies with temperature. The power density expressed in the equation (17), previously discussed, can be expressed as:

$$Q = \rho\, c_p\, \frac{\partial T}{\partial t} - \nabla(k\nabla T) \qquad (19)$$

Where, the density ρ is expressed in [kg/m³], the specific heat at constant pressure c c_p is in [J/kg·K], the temperature in [K], the time t in [s] and the thermal conductivity k in [W/m·K]. Comparing equation 17 and 18 is possible to see how, in steady-state conditions for the energy conservation, in our system the electrical energy through the Joule effect is converted in thermal energy (incoming energy), and the same energy is dissipated by heat transfer mechanisms described before (outcoming energy).The microheaters were modelled using a Finite element method (FEM) software package i.e. COMSOL™ Multiphysics.

1.6   COMSOL™ Multiphysics

1.7.1   Introduction to numerical simulation and Finite Element Method (FEM)

Numerical simulation method is based on the theoretical description of the physical systems. Initially, the mathematical equations are derived for a continuous domain. The, the equations are discretized, applied and solved only in a finite number of points of the domain. Discretization of the analysed system is bases for numerical simulation. The discretization of the domain in finite elements generates the so-called mesh. Various methods of discretization have been proposed. The Finite Element Method (FEM) is considered as a general discretization procedure of continuum problems [31]. The method was originally developed to study the stresses in complex airframe structure [32] and was later extended to the general field of continuum mechanics [33].

The finite element considers that the solution region comprises many small, inter-connected, sub-regions or elements and give a piece wise approximation to the governing equations, that is, the complex partial differential equations are reduced to either linear or nonlinear simulations equations. Since the finite element method allows us to form the elements, or sub-regions, in an arbitrary sense, a close representation of the boundaries of complicated domains is possible. The solution of a continuum problem by the FEM is approximated using the following sequential steps [34].
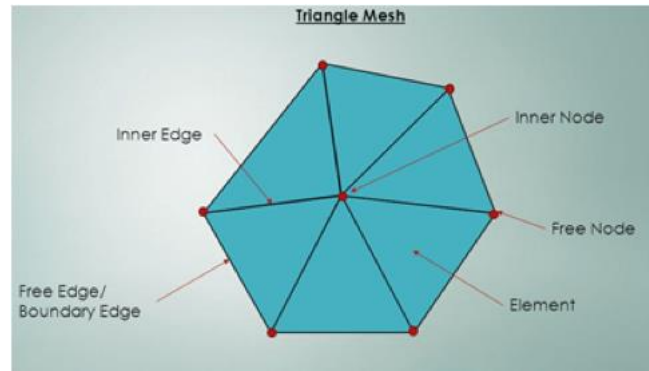
Fig 10: Typical element of a mesh with Elements, nodes and mesh [31].

• Discretize the continuum: divide the solution region into non-overlapping elements or sub-regions. The finite element discretization allows a variety of element shapes, for example in 2D, triangles, quadrilaterals. Each element is formed by the connection of a certain number of nodes (figure 10).

• Select interpolation or shape functions: the next step is to choose the type of interpolation function that represents the variation of the field variable over an element.

• Form element equations (Formulation)

• Assemble the element equations to obtain a system of simultaneous equations.

• Solve the system of equations.

In this thesis all attention is kept on the application of numerical simulation in the investigation of the behaviour of the thermal and electrical flow.

1.7.2 COMSOL Multiphysics

COMSOL Multiphysics software is a powerful finite element (FEM), partial differential equation (PDE) solution engine. The basic COMSOL Multiphysics software has eight add-on modules that expand the capabilities of the basic software in the following application area: AC/DC, Acoustics, Chemical Engineering, Earth science, Heat Transfer, MEMS, RF and Structural mechanics [35]. Multiphysics is a recent conceptualization to categorized modelling where different physicochemical mechanisms are prevent in a given application, but to be multiphysics, the field equations must couple [36]. So, "Multiphysics" refers to simulations that involve multiple physical models or multiple simultaneous physical phenomena.

The simulation of the different microheater structures is performed by coupling the power generation due to the joules heating with the heat conduction and dissipation into the device also considering the heat exchange with the heat surroundings. The multiphysics simulator uses the electric current module in combination with the heat transfer module. The joule heating was calculated as a consequence of the input voltage applied to the microheater pads.

1.6.2.I COMSOL Heat transfer Module

Product designers use the heat transfer module, developers and scientists, who use detailed geometrical descriptions to study the influence of heating and cooling in devices or processes. The Heat Transfer Module helps investigate the effects of heating and cooling in devices, components, or processes. The module furnishes we with simulation tools to study the mechanisms of heat transfer – conduction, convection, and radiation often in collaboration with other physics, such as structural mechanics, fluid dynamics, electromagnetics, and chemical reactions. In this context, the Heat Transfer Module acts as a platform for all possible industries and

applications where the creation, consumption, or transfer of heat or energy is the focus of or contributes significantly to the studied process.

After understanding the basic physics, the device need to be realized for the experimental analysis. In order to realize the device clean room technologies available at IMM-CNR are being explored.

1.7   Device fabrication techniques

Fabrication of the different microheater designs on LiNbO$_3$ crystal is performed using the clean room technologies provided at IMM-CNR. The general techniques and equipment's used for the realization of the microheater on LN crystal are discussed in this section.

1.7.1   Cleaning Process

The surface contamination of surface, especially by particle contamination, is a major problem in the fabrication process, and becomes more critical as geometries get smaller and smaller. It is well known that the device performance, reliability and product yield are critically affected by the presence of chemical contaminations and particulate impurities on the substrate surface. The objective of the substrate cleaning and surface conditioning is to remove particles and chemical impurities from the crystal surface without damaging or deleteriously altering the crystal surface. Hence a cleaning process of the LiNbO$_3$ surface is necessary and is performed to remove both organic and inorganic residues. The cleaning process involves a cleaning in acetone, water (DI) and isopropyl alcohol (IPA) for 10 min each using a sonication bath. Acetone is used to clean the oils and organic residues that appear on the LiNbO3 surface. Unfortunately the solvent (acetone) leaves their residues. This is why a two solvent method such as IPA is used for cleaning process. An additional cleaning step involving plasma process was involved in order to make sure for the removal of any other impurities or contaminations on the crystal surface (see Fig 11).

Fig 11: Image of cleaning process: Oxford plasma generator.

The plasma cleaning involves the removal impurities through energetic plasma created from oxygen gas. The plasma is created inside the chamber using high frequency voltages (typically in kHz to > Mhz) to ionize the low-pressure gas (3×10^{-3} mbar). Table III, shows the optimized parameter involved in the plasma-cleaning step using OXFORD plasma generator.

Recipe	Oxygen Flow [sccm]	RF power [W]	Pressure [mbar]	Time [Min]
Plasma-cleaning-LN	30	150	3e-3	10

Table III: Oxford Plasma generator parameters for cleaning LiNbO$_3$ surface.

The photolithography process follows the cleaning process using a photosensitive film, in order to develop microheater pattern on the LiNbO$_3$ substrate.

1.7.2   Photolithography process

Photolithography is the process of transferring geometric shapes on a mask to the surface of a substrate. Generally, there are two type of photoresist: positive and negative. For positive resist, the resist is exposed with UV light wherever the underlying material is to be removed. In these resist, exposure to the UV light changes the chemical structure of the resist so that it becomes more soluble in the developer. The exposed resist is then washed away by the developer solution, leaving windows of the bare underlying material. The mask therefore, contains an exact copy of the pattern, which is to remain on the wafer. Negative resists behave in just the opposite manner. Exposure to the UV light causes the negative resist to become polymerized, and more difficult to dissolve. Therefore, the negative resist remains on the surface wherever it is exposed, and the developer solution removes only the unexposed portions. Masks used for the negative photoresist, therefore contain the inverse of the pattern to be transferred.
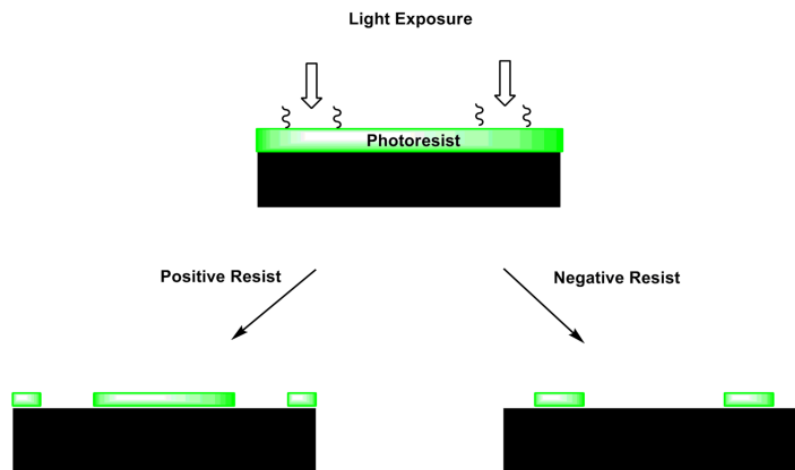
Fig 12: Pattern difference generated from the use of positive and negative resist.

Negative resist were popular in the early history, but positive resist gradually became more widely used since they offer better process controllability for small geometry features. A high performance OIR™ 906 12i positive photoresist was used for imprinting the microheater designs on the +Z surface of the crystal. OIR 906 series is a robust, fast i-line photoresist with a resolution of >0.45[μm] and a thermal stability >1200C. The standard technical product information of the OIR 906 series are shown below (see fig13):
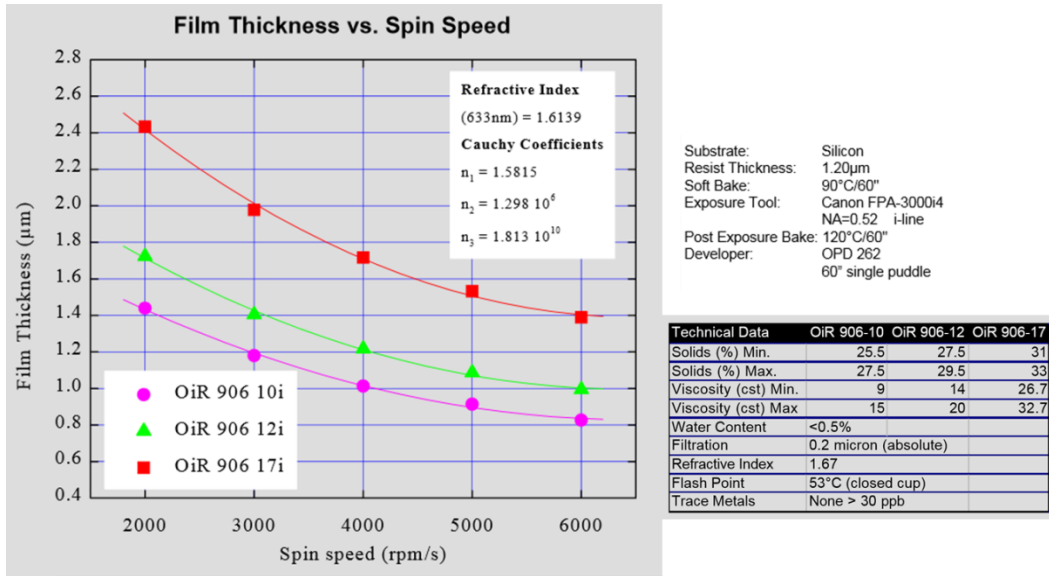
Fig 13: OIR™ 906 i-line series technical product information[37].

The photoresist is then exposed through the microheater geometric pattern on the mask with high intensity ultraviolet light. A hard contact exposure method was used where the substrate is in contact position with the mask. Because of the contact between the resist and mask, very high resolution is possible in contact printing.
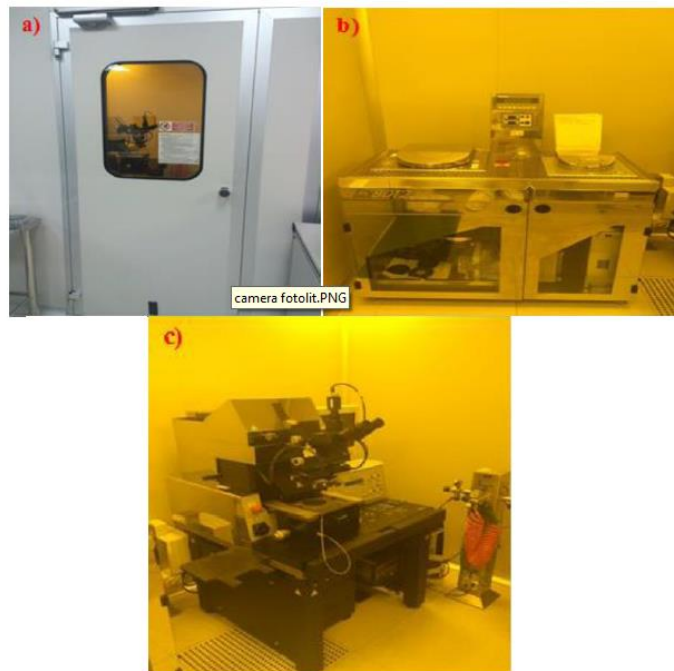

Fig 13: a) Photolithography room b) spin coater+ hot plate, and c) Mask aligner.

Finally, the sample is dipped in the developer and agitated well to remove the unwanted photoresist and generate pattern. After developing the pattern, the thin film deposition is performed for the microheaters.

### 1.7.3 Thin film deposition techniques

Two different techniques are used for depositing thin film for the microheater namely: 1) e-beam (electron beam) and 2) sputtering deposition technique. Titanium (Ti) being a strong material is deposited using E-beam

thermal deposition technique, while Aluminium (Al) and Indium Tin Oxide (ITO) are deposited using Sputtering deposition technique.

a. E-beam

E-beam evaporation is a process similar to thermal evaporation i.e. a source material is heated above its boiling/sublimation temperature and evaporated to form a film on the surfaces that is stroke by the evaporated atoms. This evaporation meth-od has just like thermal evaporation a pore ability to cover steps that also makes this method ideal for lift-off processes. A noticeable advantage of e-beam evaporation over thermal evaporation is the possibility to add a larger amount of energy into the source material. This yields a higher density film with an increased adhesion to the substrate. Because the electron beam only heats the source material and not the entire crucible, a lower degree of contamination from the crucible will be pre-sent than in the case of thermal evaporation. By using a multiple crucible E-beam gun, several different materials can be deposited without breaking the vacuum.

The E-beam evaporation process: With the source material placed in the crucible a filament below the crucible is heated. By applying a large voltage, electrons are drawn from the filament and focused as a beam on the source material by several bending magnets. The beam is swept across the surface of the source material to heat all of the material. This device consists of two main sections; an electron source, which is housed in the vacuum evaporation device, and generates electrons, accelerates them as an electron beam, and deflects them; and a crucible (hearth) section that holds the evaporated material. The electron source is also called an E-source, EB-source, or E type electron gun.
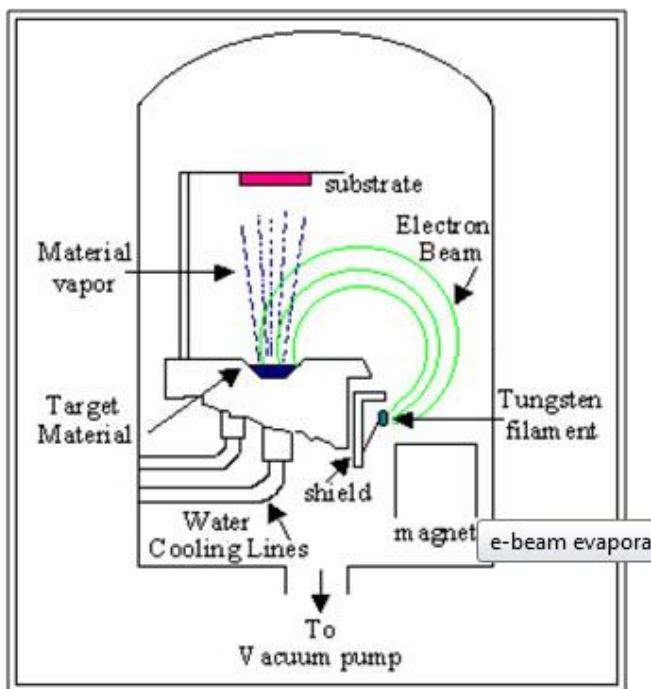
Fig 14: a) schematic structure of an electron beam evaporation device, b) e-beam depositor

Characteristics of the Electron Beam Evaporation Method

As the heat source is the kinetic energy of the electrons, the evaporant material is heated directly, which is efficient. The electricity density of the electron beam is large, and evaporation of various materials is possible, including high melting point metals, as well as oxides compounds, and substances that sublimate. Electron

beam can be precisely controlled using electric and magnetic fields. The electron beam can be scanned at high speed within a specified area, and the beam can be irradiated with the optimal electric density for the evaporant material. Electron beams are deflected by 270 degrees or 180 degrees and irradiated onto the evaporation material. It is used in a high vacuum (10^{-2}Pa to 10^{-5}Pa or so). An ultra-high vacuum type is also available. By using several crucibles and evaporation sources, it is possible to make a multi-layer film during a single processing sequence.

Comparison with other deposition methods

Compared with sputtering and CVD methods, the deposition rate is high. Creation of film as thick as 1μm or more is easily possible. Evaporation is possible even of high melting point metals and metal oxides, which cannot be evaporated (or are difficult to evaporate) by a resistance heating method or induction heating method. Because the electron beams can immediately heat or change power immediately, precise thickness control of film is possible. This is difficult with a resistance heating method or induction heating method. The evaporant material is heated directly in a water-cooled copper crucible by the electron beams, so the evaporant material re-mains free from contamination from the crucible material (No entry of impurities or creation of alloys). Electricity is applied to the filament to heat it, and induce the emission of thermal electrons. As negative high voltage (normally -4 to -10kV) is applied to the filament, this accelerates the thermal electrons due to the voltage difference between anodes. The ejected electrons are deflected by a magnetic field (permanent magnet or electromagnet) and irradiated onto the evaporant material in the crucible. As necessary, electricity is supplied to the scan coil to scan the beam and make the irradiation area larger.

b. *Sputtering*

There are many different ways to deposit materials such as metals, ceramics, and plastics onto a surface (substrate) and to form a thin film. Among these is a process called "SPUTTERING" that has become one of the most common ways to fabricate thin films. Sputtering is a physical vapour deposition (PVD) process used for depositing materials onto a substrate, by ejecting atoms from such materials and condensing the ejected atoms onto a substrate in a high vacuum environment.

The basic process is as follows. A target, or source of the material desired to deposit, is bombarded with energetic ions, typically inert gas ions such as Argon (Ar+). The forceful collision of these ions onto the target ejects target atoms into the space. These ejected atoms then travel some distance until they reach the substrate and start to condense into a film. As more and more atoms coalesce on the substrate, they begin to bind to each other at the molecular level, forming a tightly bound atomic layer. One or more layers of such atoms can be created at will depending on the sputtering time, allowing for production of precise layered thin-film structures. Though the basic idea of operation is seemingly simple, the actual mechanisms at play are intricately complex. Electrically neutral Argon atoms are introduced into a vacuum chamber at a pressure of 1 to 10 mTorr. A DC voltage is placed between the target and substrate, which ionizes Argon atoms and creates a plasma, hot gas-like phase consisting of ions and electrons, in the chamber. This plasma is also known as a glow discharge due to the light emitted. These Argon ions are now charged and are accelerated to the anode target. Their collision with the target ejects target atoms, which travel to the substrate and eventually settle. Electrons released during Argon ionization are accelerated to the anode substrate, subsequently colliding with additional Argon atoms, creating more ions and free electrons in the process, continuing the cycle.
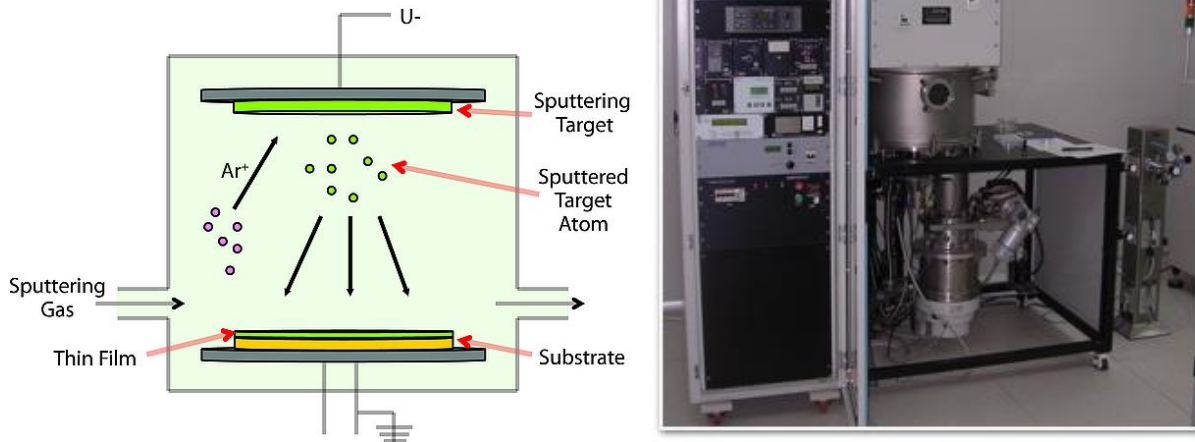
Fig 15: a) Schematic structure of a sputtering deposition technique, b) Sputtering.

After depositing the thin film materials using the respective depositing techniques, the unwanted photoresist is removed using a lift off process.

1.7.4   Lift Off process

Lift –off process is a method of obtaining patterning deposited films, which are been deposited. After the process of metal thin film deposition, the substrate is put in a glass beaker filled with acetone and placed in an ultrasonic bath. The output results in the microheater pattern development on to the respective substrate.

References:

[1] Alibart, O., Auria, V. D'., Micheli, M.D., Doutre, F., Kaiser, F., Labonte', L., Lunghi, T., Pichol-le, E'., Tanzilli, S., (2016), "Quantum photonics at telecom wavelengths based on lithium niobate waveguides", journal of optics,18: 104001(32pp).

[2] Bourim, E.M., Moon, C.-W., Lee, S.-W., Sidorkin, V., and Yoo, I.K., (2006). Pyroeletric electron emission from -Z surface polar surface of Lithium nionbate monodomain single crystal, J Electroceram, vol. 17, pp. 479-485.

[3] Tomaszewski, P., "Jan Czochralski and his method", Oficyna Wydawnicza ATUT, Wrocław–Kcynia 2003, ISBN 83-89247-27-5.

[4] http://www.almazoptics.com/LiNbO3.htm

[5] Czochralski, J., (1918) "Ein neues Verfahren zur Messung der Kristallisa-tionsgeschwindigkeit der Metalle" [A new method for the measurement of the crystalliza-tion rate of metals], Zeitschrift für Physikalische Chemie, 92: 219–221.

[6] Ramadan, A.J., Rochford, L.A., Moffat, J., Mulcachy, C., Ryan, M.P., Jones, T.S., Heutz, S., (2016), "The morphology and structure of vanadyl phthalocyanine thin films on lithium ni-obate single crystals" J.Mater.Chem.C, 4,348-351, DOI: 10.1039/C5TC03730A.

[7] Coates, P. B. (1981). Multi-wavelength pyrometry. Metrologia , 17, 3.

[8] Fujitsuka, N., Sakata, J., Miyachi, Y., Mizuno, K., Ohtsuka, K., Taga, Y., Tabata, O. (1998). Monolithic pyroelectric infrared image sensor using PVDF thin film. Sensor and Actuators A:Physical , 66 (1-3), 237-243.

[9] Lang, S. B. (2005, august). Pyroelectricity: From ancient curiosity to modern imaging tool. Physics Today , 31-36.

[10] Lehman, J., Eppeldauer, G., Aust, J. A., Racz, M. (1999). Domain-engineered pyroelectric radiometer. Applied Optics , 38 (34), 7047-7055.

[11] Kim, D. W., Moon, C. W., and Yoo, I. K. (2003). Pyroelectric Emission Lithography. Journal of the Korean Physical Society , 42, s1196-s1198.

[12] Moon, C. W., Kim, D.-W., Rosenman, G., Ko, T. K., and Yoo, I. K. (2003). Patterned Pyroelectric Electron Emitters and their Feasibility Study for Lithography Applications. Japanese Journal of Applied Physics , 42, 3523.

[13] Coppola, S., Vespini, V., Grilli, S., and Ferraro, P. (2011). Self-assembling of multi-jets by pyro-electrohydrodynamic effect for high throughput liquid nanodrops transfer. Lab on a Chip , 11, 3294-3298.

[14] Rosenman, G., Shur, D., and Skliar, A. (1996). Ferroelectric electron emission flat panel display. Journal of applied physics , 79, 7401.

[15] N. Balcon, D. Payan, M. Belhaj, T. Tondu and V. Inguimbert, "Secondary Electron Emission on Space Materials: Evaluation of the Total Secondary Electron Yield From Surface Potential Measurements," in IEEE Transactions on Plasma Science, vol. 40, no. 2, pp. 282-290, Feb. 2012. doi:10.1109/TPS.2011.2172636

[16] Neidholdt, L. E., and Beauchamp, L. J. (2007). Compact ambient pressure pyroelectric ion source for mass spectrometry. Analytical chemistry , 79, 3945-3948.

[17] Neidholdt, E. L., and Beauchamp, J. L. (2009). Ionization mechanism of the ambient pressure pyroelectric ion source (APPIS) and its applications to chemical nerve agent detection. J Am Soc Mass Spectrom , 20, 2093-2099.

[18] Gennari, O., Grilli, S., Coppola, S., Pagliarulo, V., Vespini, V., Coppola, G., Bhowmick, S., Gioffré, M.A., Gentile, G., Ambrogi, V., Cerruti, C., Carfagna, C., Ferraro, P. (2013). Spontaneous assembly of carbon-based chains in polymer matrix through surface charge templates. Langumir , 29, 15503-15510.

[19] Ferraro P., Coppola S., Grilli S., Paturzo M. and Vespini V. (2010). Dispensing nano–pico droplets and liquid patterning by pyroelectrodynamic shooting. Nature Nanotechnolo-gy, 5, 429–435, doi: 10.1038/nnano.2010.82.

[20] Vespini, V., Coppola, S., Grilli, S., Paturzo, M., and Ferraro, P. (2013). Milking liquid nano-droplets by an IR laser: a new modality for the visualization of electric field. Meas. Sci. Technol., 24 045203, doi: 10.1088/0957-0233/24/4/045203.

[21] Salvia, J.C., Melamud, R., Chandorkar, S.A., Lord, S.F., Kenny, T.W., (2010)."Real- time temperature compensation of MEMS oscillators using an Integrated Micro-Oven and a phase-locked loop", journal of microelectronics systems, 19(1), 192-201.

[22] http://www.engineeringtoolbox.com/thermal-conductivity-d_429.html

[23] James C. Sturm, Wendy Wilson, Mario Iodice (1998), "Thermal effects and scaling in organic light emitting flat panel displays", IEEE Journal of selected topics in quatum electronics, Vol 4, No.1.

[24]Dai, C.L., (2007). "A capacitive humidity sensor integrated with microheater and ring oscillator circuit fabricated by CMOS-MEMS techniques", Sensors Actuators.B, 122: 375-380.

[25] Coppola, G., Sirleto, L., Rendina, I., and Iodice, M., (2011). "Advance in thermo-optical switches: principles, materials, design, and device structure", 50(7), 071112.

[26] Chul ha, S., Kim, .S., Yang, Y., Kim, Y.J., Cho, S.M., Yang, H., Kim, Y.T., (2005). "Inte-grated and microheater embedded gas sensor array based on the polymer composites dis-pensed in micro-machined wells", Sensors and Actuators B: chemical, 105(2), 549-555.

[27] Neda, T., nakamura, K., and Takumi, T., (1996). "A polysilicon flow sensor for gas flow meters", Sensor and actuators A: physical, 54 (1-3), 626-631.

[28] Sberegglieri, G., Hellmich, W., Müller, G., (1997)."silicon hotplates for metal oxide gas sensor elements", microsystem technologies, 3, 183.

[29] Creemer, J. F., Helveg, S., Kooyman, P. J., Molenbroek, A. M., Zandbergen, H.W., Sarro, P. M., (2010). "A MEMS reactor for atomic-scale Microscopy of nanomaterials under industrially relevant conditions", Journal of micromechanical systems, 19(2), 254-264.

[30] Mills, A.F., (1999). "Basic heat and mass transfer", 2nd edition, prentice hall.

[31] Zienkiewicz, O.C., Taylor, R.L.,(2000), "The finite element method. Volume 1: the basic, fifth edition, butterworth-heineman.

[32] Clough, R.W., (1960), "The finite element analysis in plane stress analysis", proceedings 2nf ASCE Conf. On Electronic computation, Pittsburgh, PA.

[33] Zienkiewicz, O.C., and Cheung, K., (1965), "Finite elements in the solution of field problems", 200, 507-510.

[34] Lewis, R.W., Nithiarasu, P., seetharamu, K.N., (2004),"Fundamental of the finite element method for health and fluid flow, john wiley & sons, Ltd.

[35] Pryor, R.W., (2000), " Multiphysics Modelling using COMSOL. A first principle Ap-proach", jones and Barlett Publishers.

[36] Zimmerman, W.B.J., (2004), " COMSOL process modelling and simulation with finite element methods", worild scientific publishing Co. Pte Ltd.

[37] https://crn2.3it.usherbrooke.ca/guide_sb/produits/resines/Fujifilm%20OIR-906.pdf

Chapter 2
Numerical Model, Design and Fabrication

2.1   Designing

In designing microheaters for our PED (pyroelectric effect device) few crucial parameter were kept in mind: area of temperature uniformity, low power dissipation and thermal mass. The electro-thermal analysis of the four different microheater designs namely: Meander, Spiral, Fan and S shape is investigated using COMSOL™ Multiphysics [1]. The microheater occupies an area 3.5mm × 3.5mm (see Fig. 17) with a titanium layer 300nm thick. In the full 3D numerical model, a LiNbO$_3$ substrate with a size of 10mm × 10mm × 500μm was considered.
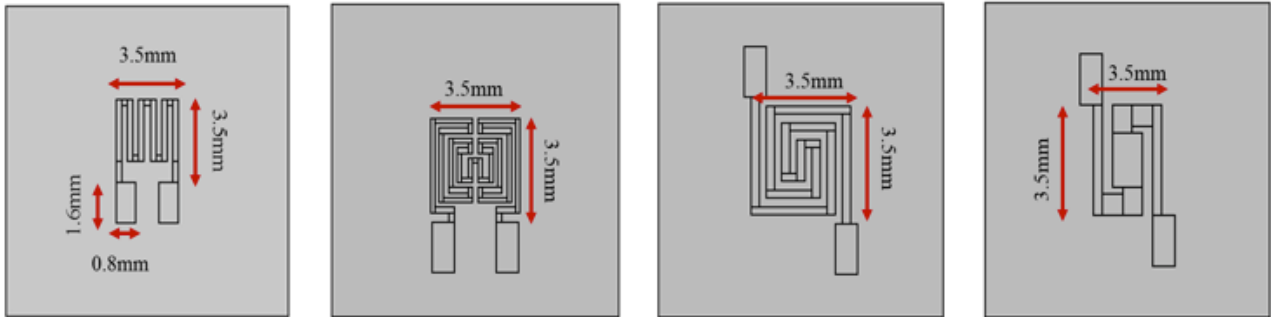
Fig17: Microheater designs a) Meander, b) Fan, c) Spiral, and d) S shape

The meander design is a simple resistor design and serves as the basis for comparison. The spiral and fan design allows the heater length with area to be optimum, while the S-shape design has the low resistance.

2.2   Numerical simulation using COMSOL™

2.2.1   Resistive Joules heating

The simulations are performed by coupling the power generation, due to the joule heating, with the heat conduction and dissipation into the device considering also the heat exchange with the surrounding air. The multiphysics simulation uses the electric current module in combination with the heat transfer module. The joule heating was calculated as a consequence of the input voltage, V$_{pot}$ applied to the heaters pads. In particular, the electrical conductivity of the microheater, σ was modelled using a temperature dependent equation:

$$\sigma = \frac{1}{\rho_o * (1 + \alpha(T - T_0))} \tag{20}$$

Where, ρ_o is the resistivity at a reference temperature T_0, and α is the temperature coefficient of the resistivity that takes into account the dependence of the resistivity of the temperature. In order to evaluate the heat transfer in the pyroelectric material, several material properties of both the LiNbO$_3$ and Ti are required. Moreover, since the electrical and thermal properties of thin film materials differ from the bulk material properties, some of the titanium properties were specifically evaluated. In particular, the thermal conductivity of 300nm-thick film of titanium was considered to be 16.8 Wm^{-1}K^{-1} [2]. This value is lower than the thermal conductivity of bulk materials (21.9 Wm^{-1}K^{-1}) [2] due to the fact that, thermal transport of atoms is lowered as a result of the phonon scattering at lattice imperfections and boundaries [2]. Similarly, the electrical conductivity decreases due to the increase in thin film resistivity, occurring because of the low mean free path of the conduction electrons due to high scattering effect [3-4]. The electrical resistivity of our titanium thin films was evaluated

(using four-point probe measurement) to be 1.732 $\mu\Omega \cdot m$. All other parameters used for the heat transfer simulations are listed are listed in table IV.

Parameter	Titanium	LiNbO₃
Specific Heat capacity at constant pressure (C_p) [J/kg*K]	129	550
Electrical Resistivity (ρ) [$\mu\Omega \cdot m$]	1.732	2.63×10^{14}
Density (rho) [kg/m^3]	4506	4700
Thermal conductivity (k) [W/(m*K)]	16.8	5.6
Surface emissivity (ε)	0.35	0.60

Table IV: Different material properties for LiNbO₃ and Titanium [3-4].

2.2.2 Physics & Boundary conditions

Both steady state and transient analyses are performed. The joule heating is simulated as a result of an input voltage V_{pot} applied to the heater's pads. In time dependent study, a square voltage pulse is applied to switch the heater on and off at different time intervals. The heat transfer problem is solved considering Dirichlet, Neumann and mixed boundary conditions, and under the following realistic assumptions:

(i) Natural convective heat transfer was assumed for both sides of the LiNbO₃ surface and bottom surface of microheater, towards the surrounding environment (which is modelled as air with a constant temperature of 27°C).

(ii) The thickness of the LiNbO₃ (500 μm) was much higher than the thickness of microheater (300nm); hence, to reduce the mesh complexity and minimize the modelling error, independent meshing procedures were considered for the different geometric structures. On the microheater upper surface, triangular 2D meshing is used with a minimum element size of 0.13mm and using a swept layer that mesh was projected along the thickness, resulting in 3D layered mesh. In LiNbO₃ volume a 3D tetrahedral meshing is considered with the minimum element size of 0.4mm;

(iii) In heat transfer physics; the heat dissipated from the surface of LiNbO₃ and microheater is greater than the heat dissipated from the vertical sides of the crystal. Hence, we can neglect the heat dissipation from the lateral surfaces by considering there a thermally insulated boundary condition [5].

(iv) In electric current physics, the contact resistance between microheater pads and connecting are considered negligible.

(v) Radiate heat power is proportional to the fourth power of temperature and hence makes a considerable amount of contribution in thermal exchange process. The physics was applied on the surfaces (top and bottom) of LiNbO₃ and microheater by applying a diffuse layer with the surface emissivity of LiNbO₃ and microheater material shown in Table IV. There is no known literature work performed on the surface emissivity of LiNbO₃, thus experimental analysis were performed to evaluate its value. A two-point calibration procedure was adapted in order to evaluate the surface emissivity using an IR camera based set-up [6]. It was estimated that the LiNbO₃ surface emissivity value varies with a percentage between 30% & 23% depending on which the reference value was approx in a range between 0.5-0.65 at an ambient temperature.

2.2.2(a) Mesh: Building and sensibility

One of the most important steps before of launching the simulation is building an appropriate mesh for the case study.

In COMSOL multiphysics, we can create manually the mesh, selecting various options to customize it, otherwise the software can build it automatically for the entire structure. We decide to build it manually, because we have two different domains with different dimensions and very large aspect ratio. The crystal, in particular, is thick 500 µm, while the micro-heater is 300 nm, so we choose to build a mesh customized for the two different domains (figure 18 (e-f)).

Crystal mesh

For the crystal we choose a mesh with 3-D tetrahedral elements that divided the entire domain. Each element has a minimum dimension of 250 µm that is half a minimum dimension of the crystal. The smaller elements are in correspondence to the edges, where there is the intersection of the two-domains, as in the figure 18(f).

Micro heater mesh

The micro-heater has a thickness of 300 nm, for this reason we choose a different mesh strategy. A mesh with 3-D elements, indeed, has the problem that the size of the elements is the same in all three dimensions. This represents a limit for our geometry, because with a single element size in nanometres range, we will have an extremely large, and unnecessary, number of elements to cover the entire geometry. We choose, as answer to this problem, a mesh with 2-D triangular elements on the surface of the micro-heater with a swept along the thickness of the same.

The software, besides, gives us the possibility of customizing the meshes for different geometries, thanks to selection of various option as the maximum element growth rate, the curvature factor and the resolution of narrow region (figure 18(e)).

The building of the mesh for both domains is the result of a sensibility analysis work using a method of mesh refinement. Mesh refinement method refers to the process of increasing the number of elements used to model. In finite element analysis, in fact, solution accuracy is judged in terms of convergence as the element "mesh" is refined. The optimized meshing for the simulation is determined by performing an independent grid study to minimize the modelling error. When the change in the solution between subsequent stages of meshing refinement is considered to be negligible, the lower but still sufficient mesh resolution is kept (figure 18 (e-f)).

| Domain elements	67308	755988
Boundary elements	30716	90408
Edge elements	5024	7896
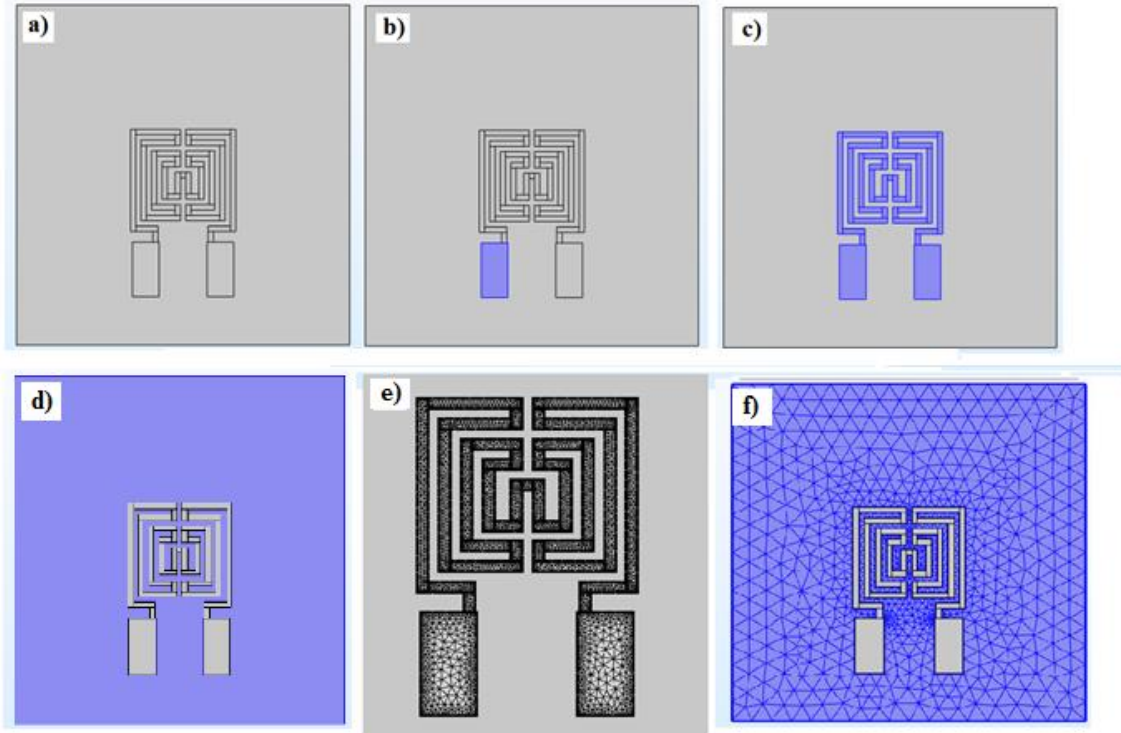
Fig 18: a) Fan shape microheater, b) terminal voltage, c) & d) Convective cooling boundary conditions on Microheater and LN surface, e) & f) Meshing configuration of Microheater and LiNbO₃.
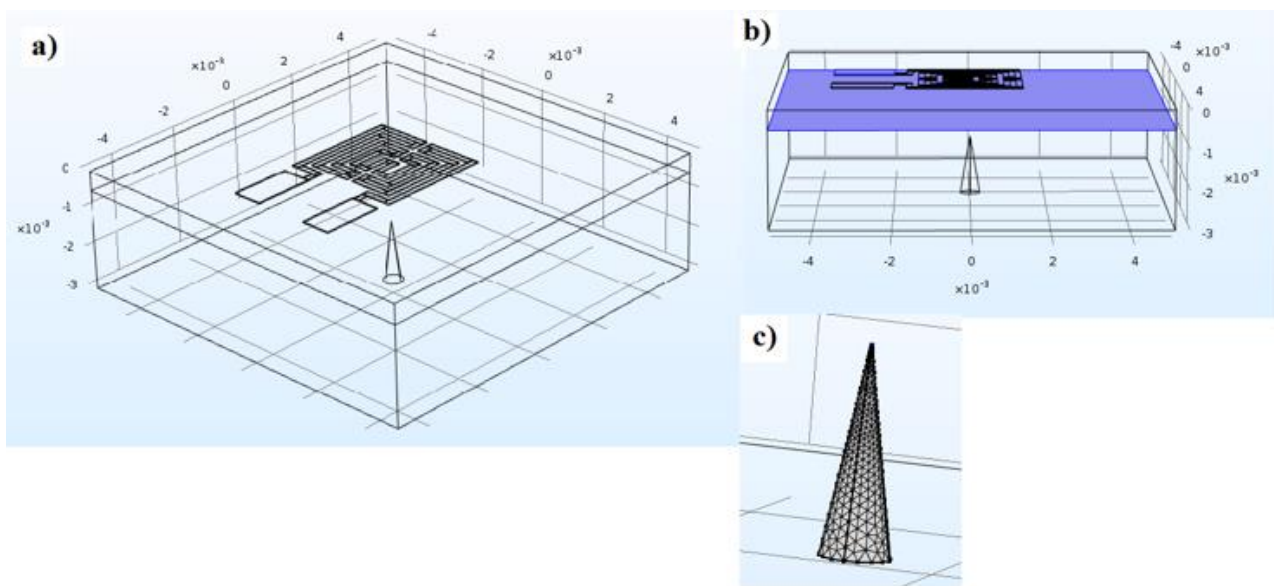
2.2.3   Electrical Field study configurations

The activation of pyroelectric effect by the microheater and the related induced electrical field is simulated using COMSOL™ Multiphysics. In particular, the steady state electric field formation between the –Z surface of LiNbO3 crystal and a metallic probe tip is investigated. In Fig. 19 the simulated structure is sketched. A beryllium metallic probe tip is considered with a height dimension of 1.5 mm and a probe tip radius of 1μm. The tip is electrically grounded and immersed in air. The electrical field between the tip and the pyroelectric crystal depends on the electrical potential build up on the surface of crystal in response to a temperature variation. In particular, the electrical potential is related to the temperature variation ΔT by equation 21 [7]; i.e.:

$$V = d_{cr} * \gamma * \Delta T / \varepsilon_{cr} \qquad (21)$$

Where, d_{cr} is the crystal thickness, γ =8.2nC*cm-2* K-1 and ε_{cr}=31 are the pyroelectric coefficient and the dielectric constant of LiNbO₃ along z-axis, respectively. COMSOL simulator is used to estimate the electrical field distribution around the tip as function of the gap between the tip and the LiNbO₃ surface. In particular, this gap is varied from 100μm to 1mm.
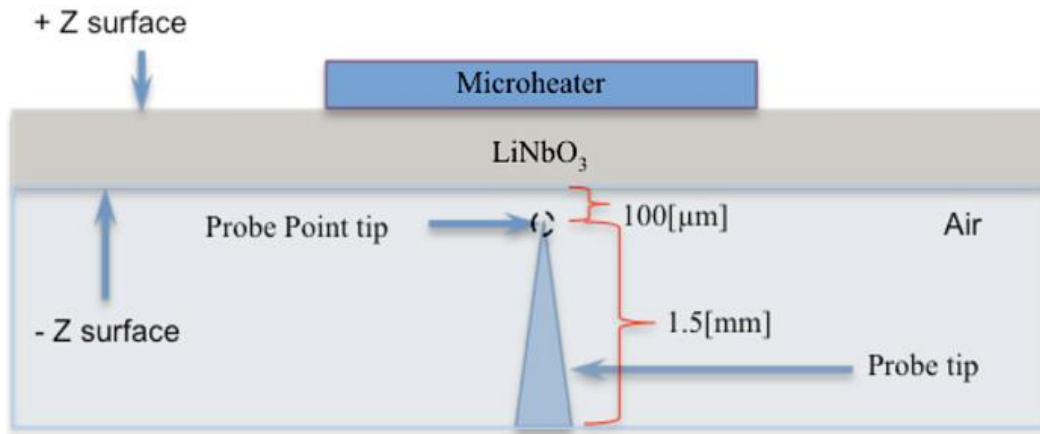
Fig19: Design used for the electric field simulation between probe tip and –Z surface of LiNbO₃ crystal.

Fig 20: a) metallic tip probe set up, b) build up electric potential boundary conditions, c) Meshing configuration of the platinum tip.

2.2.4 Study configuration

Once defined the mesh, we set the option "stationary study", that is a no-time-dependent study, with a "parametric sweep" of the voltage applied to each micro-heater. "Parametric sweep" is a special function that gives us the possibility to analyses the problem varying, in a prefixed range, a specific parameter. We choose to vary the value of the voltage applied, because we want to know the behaviour of each microheater at different temperature levels until a maximum absolute temperature of 70 °C. This absolute value of temperature (70 °C) is selected because it is observed during the experimental analysis that the crystal develop cracks initially and finally result in breaking beyond a maximum temperature of 75 °C. The last and most important option is the "Solver Configuration" where the software gives the possibility of choosing the solver type before computation. There are two main categories with different characteristics:

-        Direct solvers

-        Iterative solver

Direct solvers

The direct solvers used by COMSOL are the MUMPS, PARDISO, and SPOOLES solvers. All of the solvers are based on LU decomposition.

These solvers will all arrive at the same answer for all well-conditioned finite element problems, which is their biggest advantage, and can even solve some quite ill-conditioned problems. From the point of view of the solution, it is irrelevant which one of the direct solvers we choose, as they will return the same solution. The direct solvers differ primarily in their relative speed. The MUMPS, PARDISO, and SPOOLES solvers can each take advantage of all of the processor cores on a single machine, but PARDISO tends to be the fastest and SPOOLES the slowest. SPOOLES also tends to use the least memory of all of the direct solvers. All of the direct solvers do require a lot of RAM, but MUMPS and PARDISO can store the solution out-of-core, which means that they can offload some of the problem onto the hard disk. The MUMPS solver also supports cluster computing, allowing we to use more memory than is typically available on any single machine.

Iterative solvers

The iterative solvers in COMSOL encompass a variety of approaches, but they are all conceptually quite simple to understand at their highest level, being essentially similar to a conjugate gradient method. Other variations include the generalized minimum residual method and the biconjugate gradient stabilized method, and there are many variations on these, but they all behave similarly.

Contrary to direct solvers, iterative methods approach the solution gradually, rather than in one large computational step. Therefore, when solving a problem with an iterative method, we can observe the error estimate in the solution decrease with the number of iterations. For well-conditioned problems, this convergence should be quite monotonic. If we are working on problems that are not as well-conditioned, then the convergence will be slower. Oscillatory behaviour of an iterative solver is often an indication that the problem is not properly set up, such as when the problem is not sufficiently constrained. A typical convergence graph for an iterative solver is shown below:
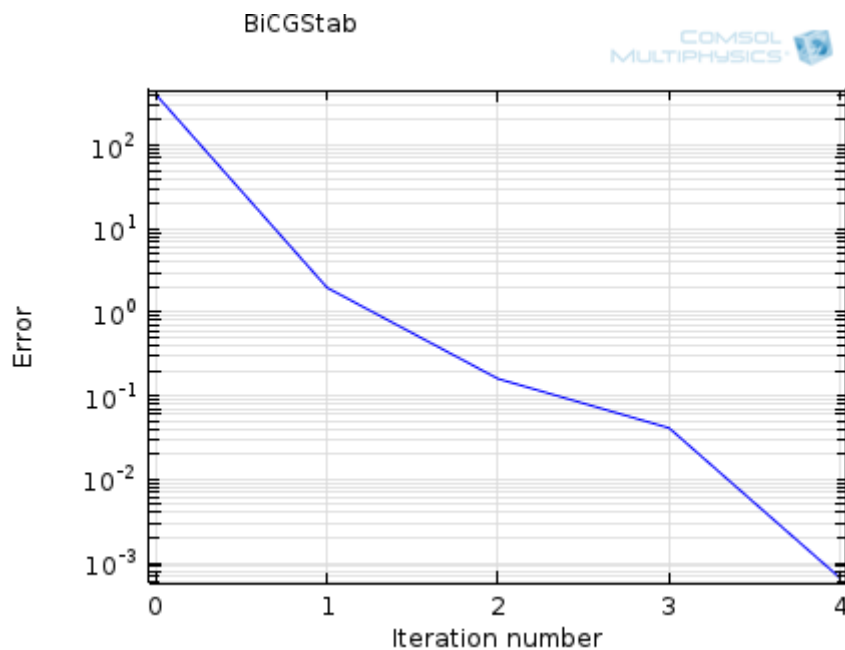
By default, the model is considered converged when the estimated error in the iterative solver is below 10^{-3}.

The solver type is determined by performing an independent set of simulations to minimize iterative error. We begin using an iterative solver for more simulations on the same model: we tightened at each step the criteria

of convergence and the results of each simulation are analysed and compared with the results of the previous one. Next, with the aim to reduce the time of computation, we choose a direct solver, comparing the results of the simulations to those obtained with the iterative method. Using a direct solver, we have, for that reason, well-detailed results with a reasonable time of computation.

2.3   Fabrication process

Fabrication of the different microheater designs on $LiNbO_3$ crystal is performed in the clean room environment at IMM-CNR. The sequential step processes involves cleaning, photolithography, thin film deposition and lift-off. A 3-inch single domain z-cut Lithium Niobate ($LiNbO_3$) of 0.5 [mm] thickness was cut in 10[mm] × 10[mm] using a diamond cutter. Four samples are obtained using the above-mentioned step for the four different microheater designs. A small "LN" sign was made on the +Z surface of the crystal in order to differentiate between the +Z and –Z surfaces of the $LiNbO_3$ crystal. Acetone was pour into a glass container. The four $LiNbO_3$ samples were set on a sample holder and placed in the container with acetone. The container was then kept in the sonication bath for 10 min. The sample holder was then remove and place in a container with the DI water for another 10 min. IPA cleaning for 10 min in the same sonication bath followed this step. The samples were removed and dried using a nitrogen blower.

Fig 21: Solvents beakers in sonication bath

The cleaning step was flowed by the oxygen plasma cleaning technique, the parameters can be observed in table V. Table V, shows the optimized parameter involved in the plasma-cleaning step using OXFORD plasma generator.

Recipe	Oxygen Flow [sccm]	RF power [W]	Pressure [mbar]	Time [min]
Plasma-cleaning-LN	30	150	3e-3	10

*Table V: Oxford Plasma generator parameters for cleaning $LiNbO_3$ surface.*

After the cleaning process a positive photosensitive thin film is spin coated on the $LiNbO_3$ substrate. The optimal spin speed suggested for the OIR 906 Fuji film resists is in a range between 2000-4000 rpm for a thin film resists. The +Z surface of $LiNbO_3$ surface of all the four samples were spin coated with OIR-906 12i photoresist at 4000rpm for 60 [s] in order to obtain a film thickness of 1.2[μm]. The spin coating of the photoresist using a hot plate followed a soft bake at 90^0C. Soft baking plays a very critical role in photo imaging. This step removes solvent from photoresist. It is a critical step as excessive baking may affect the photoactive part of the photoresist and reduce sensitivity. The photoresist coating becomes photosensitive only after soft baking.

The photoresist is then exposed through the microheater geometric pattern on the mask with high intensity ultraviolet light (12 W/cm^2). A hard contact exposure method was used where the substrate is in contact position with the mask. Because of the contact between the resist and mask, very high resolution is possible in con-tact printing. The UV exposure was performed for 4.5 [s] using the mask aligner. Subsequently, hard baking was performed at 120^{0}C for the samples, to harden and improve the adhesion of the photoresist on the surface of the crystal. Finally, the sample is dipped in the developer and agitated well to remove the un-wanted photoresist and generate pattern. The development of the photoresist was performed for 60 [s] using OPD-4624 developer.
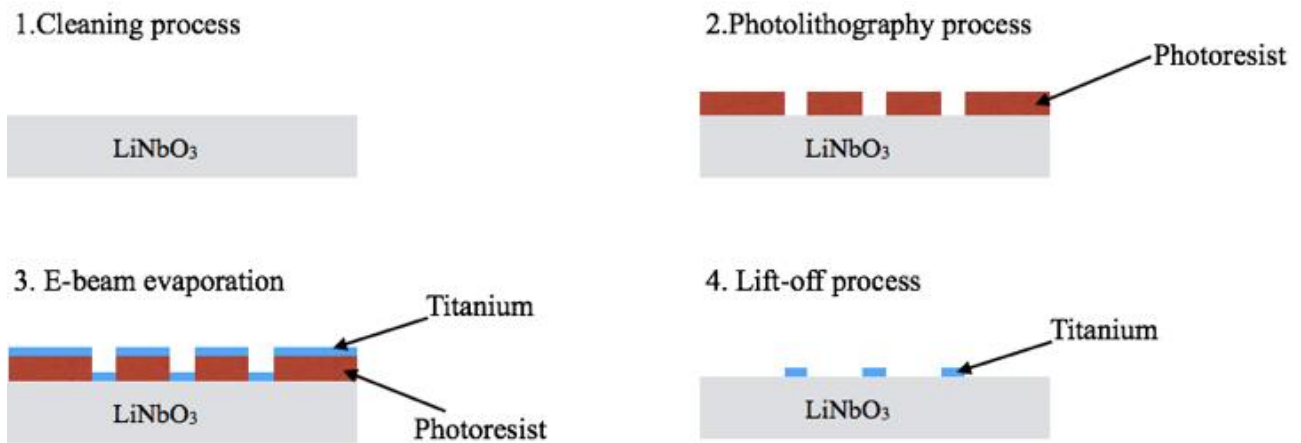
Fig 22: The schematic view of the fabrication process steps

In the second step of fabrication, we used electron-beam evaporation technique for depositing 300 nm thick Ti films onto the patterned LiNbO$_3$ +Z face, while sputtering is used to deposit aluminium and ITO of same thickness. Then a lift off process was performed in acetone for 20 min using the sonication bath. Finally, the pads of the microheater were wire bonded using silver paste.
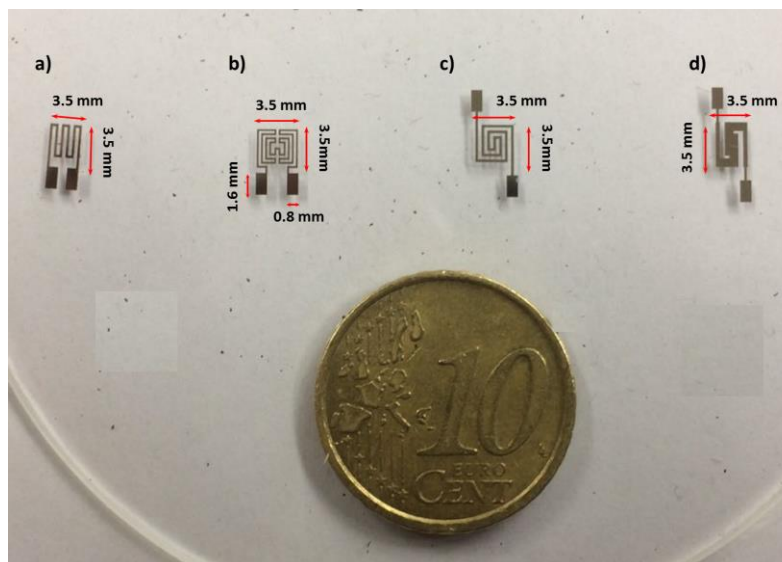
Fig23: Four different titanium micro-heater geometries: a) Meander, b) Fan, c) Spiral, and d) S-shape

The microheater resistance obtained for different materials are shown in the table VI:

Design	Track length [mm]	Microheater Resistance		
		Titanium [Ω]	Aluminium [Ω]	ITO [k Ω]
Meander	17.6	373	21	71.3
Fan	31.97315	818	49.73	155.5
Spiral	26.644	707	42.74	133.2
S shape	11.89	137	11.42	25.98

Table VI: Measured resistance obtained for different microheater design with different materials

Titanium microheaters are being considered for further pyroelectric analysis from the –Z surface of the Lithium Niobate crystal. Titanium has a high melting point, low density and remains resistance to corrosion in various conditions due to the thin layer of oxide formation on its surface makes it's a desirable material for various devices such as infrared and pressure sensors. In addition Titanium has a good adherence property with LiNbO$_3$ substrate making it an ideal material for our micro-heaters.

Design	Simulated resistance [Ω]	Measured Resistance [Ω]
Meander	365	373
Fan	807.5	818
Spiral	695	707
S shape	130	137

Table VII: Simulated and measure resistance obtained for different microheaters designs.

In the micro-electro-mechanical systems (MEMS) industry, thin film material properties database and measurement techniques have attracted engineer's attention recently due to the expansion in field of MEMS applications. Experimental evidence conducted over the years has made it clear that the size of an object can have an effect on its properties such as: mechanical, thermodynamics, electrical and optical properties. It is understood clearly that when materials shrink to dimensions on microscale or nanoscale, many of the properties or characteristics that they display in bulk form are no longer valid [8-12]. The reasons for these changes in properties are due to increased surface interactions as well as absorption and scattering effects. Thermal and electrical conductivity of thin films materials are an important parameter for any new MEMS applications such as pressure sensor, micro actuators and in our case microheaters [13-14]. The performance and reliability of these devices are influenced often by the degree to which they can conduct heat and electricity.

2.4　Thermal and electrical properties of microheater materials

The thermal and electrical properties of 3 materials namely: Titanium (Ti), Aluminium (Al) and Indium Tin Oxide (ITO) for the microheater device are investigated.

2.4.1　Electrical Conductivity [S/m]

Generally in metals, electrical resistivity (ρ) is discussed instead of conductivity (σ). These two properties are reciprocally related:

$$\rho = 1/\sigma \tag{22}$$

The value of ρ depends on the structure of the metal and the temperature. According to Mattiesen's rule, the electrical resistivity comprises of two components, one due to impurities and defects, and the other due to lattice vibrations [15-16].

$$\rho\,(T) = \rho_{res} + \rho_{th}(T) \qquad (23)$$

The magnitude of ρ_{res} called the residual resistivity, which is determined by the defects within the structures of thin film: the concentration and distribution of vacancies, impurities, and grain boundaries. These defects cause an increase in the scattering of electrons, thus reducing the mean free time between collisions. The magnitude of the second term, ρ_{th}, depends on the temperature of the material, and due to the presence of lattice vibrations. The amplitude of the lattice vibrations increases with increasing temperature, and the more they interfere with conduction.

Residual resistivity

Several studies have shown that diminishing one of the dimensions of a conductor will alter the electrical resistivity of the material [17-23]. The bulk electrical resistivity of the material changes to that of the thin film material. This change is because of the mean free path of conduction electrons that reduced due to the increase in scattering effects. Obviously, the electrical resistivity and other properties of thin films may behave differently than expected, if the thickness of the material becomes sufficiently small. The electrical resistivity of a thin film increases because of the low mean free path of the conduction electrons due to high scattering effect. There are several scattering mechanisms that exist in materials, which alter the path of electrons in metal thin films such as: surface scattering, scattering from grain boundaries, scattering from uneven or rough surface and scattering due to impurities. These effects are dependent on the procedures and conditions used to fabricate the thin films. However, what is clear about these scattering mechanisms is that processing techniques and impurity concentration will have a larger effect on bulk resistivity, while the grain boundary size and rough surface scattering are more prominent for smaller film thicknesses [24].

In our case, we investigated the electrical resistivity of various thin film materials listed in the table VII with their respective bulk resistivity value at room temperature below:

List of Materials	Bulk Resistivity (Ω.m) at 20^{0}C
Titanium (Ti)	420×10^{-9}
Aluminium (Al)	28.2×10^{-9}
Indium Tin Oxide (ITO)	1×10^{-6}

Table VII: List of materials investigated for microheaters.

In order to reduce the scattering mechanism fewer steps were taken into consideration during the fabrication process such as, the grain boundary size and rough surface scattering were more prominent for thickness below 100nm [24]. Henceforth, the electrical resistivity for thickness above 100nm was investigated for the enlisted microheater materials. Different deposition techniques were used to deposit the thin films on glass substrate (76mm×26mm×0.5mm) for the electrical resistivity measurements. A well-known four-point probe method was adapted to evaluate the electrical resistivity of thin film materials. In a four point probe system, a constant current I is applied to the extreme end probe and the potential V on the inner two probes with high impedance voltmeter is measured (see fig 24)[25].
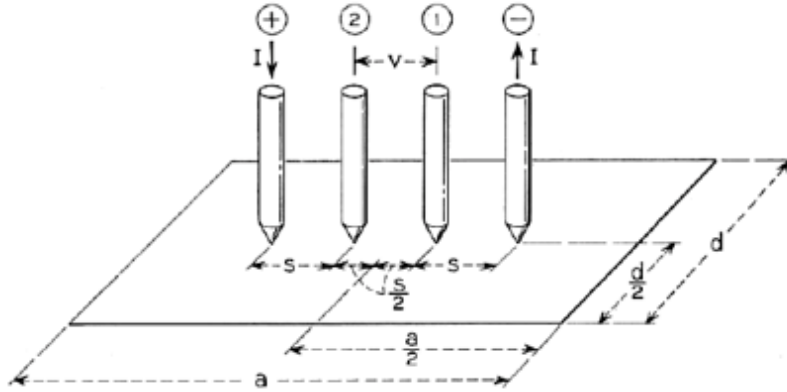
Fig 24: a) Schematic diagram for 4-point probe measurement.

The functional relationship evaluated using four-point probe between the resistivity ρ_0 and an infinite slice thickness "th" (i.e. thickness of thin film << length & width of substrate) is given by equation (24).

$$\rho_{res} = \rho_0 = \frac{V}{I} * th * 4.5324 \qquad (24)$$

For small value of d/S (see fig24), we used a correction factor CF of 4.5324 [23]. The obtained electrical resistivity for the different materials (Titanium, aluminium, ITO) with respect to the thickness is shown in the fig 25.
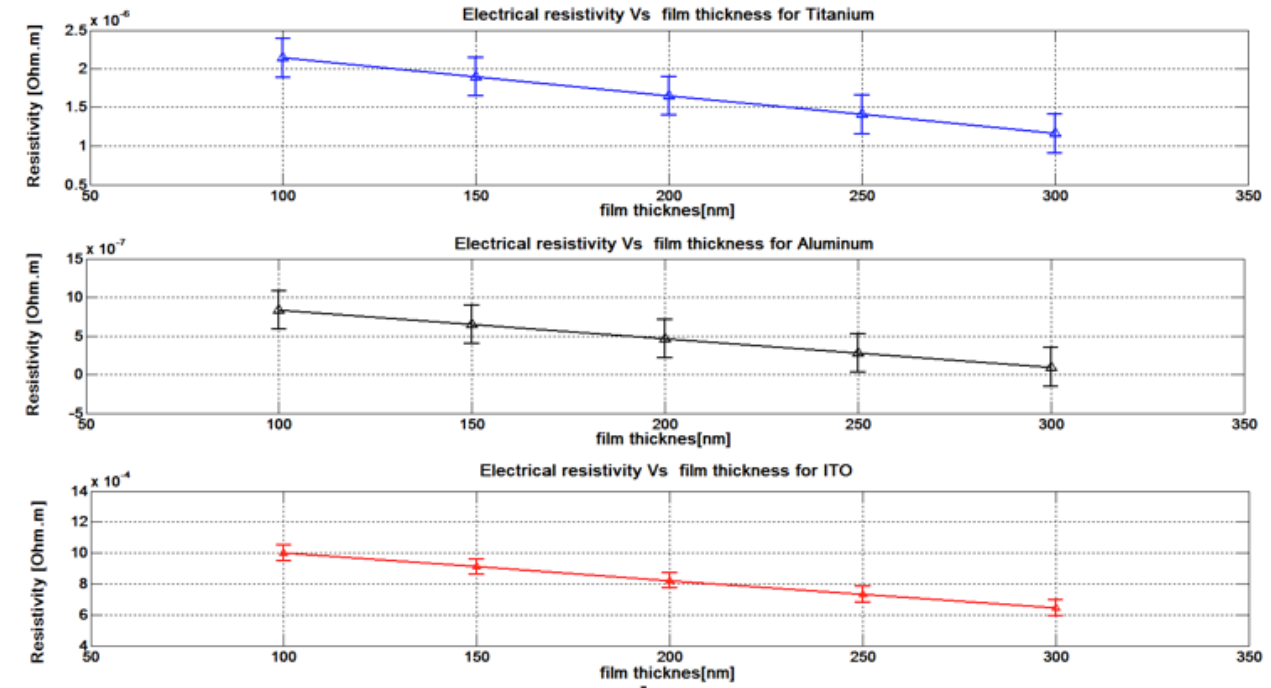
Fig 25: Obtained electrical resistivity for different microheater materials.

Lattice Resistivity

As the temperature increases so as the lattice vibration in the thin film material, thereby causing a change in resistivity. In general, electrical resistivity of metals increases with temperature. If the temperature T does not vary too much, a linear approximation can be used:

$$\rho_{th}(T) = \rho_0\left[\alpha\left(T - T_0\right)\right] \qquad (25)$$

Where α is called the temperature coefficient of resistivity (in $^0\text{C}^{-1}$), T_0 is the reference temperature (20^0C), and ρ_0 is the thin film resistivity ($\Omega.\text{m}$) at temperature at T_0. Table VIII shows the thin film resistivity of materials evaluate using the Vecco FPP-5000 4-point probe with respective temperature coefficient.

Materials Film thickness (300nm)	Thin film resistivity at 20^0C ($\mu\Omega$-m)	Temperature coefficient ($^0\text{C}^{-1}$)
Titanium (Ti)	1.613	0.0038
Aluminium (Al)	0.096	0.0043
Indium Tin Oxide (ITO)	643.05	0.002-0.003

Table VIII: Thin film resistivity and temperature coefficient of materials.

Employing Matthiessen's rule, the thin film resistivity of the materials can be estimated by combining both residual resistivity and lattice resistivity of the thin film material.

$$\rho\ (T) = \ \rho_{res} + \ \rho_{th}\ = \rho_0 + \ \rho_0\ (\alpha\Delta T) \tag{26}$$

In Table IX, the estimated thin film resistivity $\rho\ (T)$ of different materials with their respective thermal conductivity ($(\sigma = \frac{1}{\rho(T)})$) of different materials are shown.

Materials Film thickness (300nm)	Thin film resistivity at $\Delta T= 20^0\text{C}$ ($\mu\Omega$-m)	Electrical conductivity (σ) [S/m]
Titanium (Ti)	1.7356	5.762×10^5
Aluminium (Al)	0.1043	95.877×10^5
Indium Tin Oxide (ITO)	681.58	0.0147×10^5

Table IX: Estimated thin film resistivity and electrical conductivity for a 300[nm] thick film of each choice of material.

Note1: Thin film thickness of 300nm was taken into consideration for the thermal conductivity analysis, as its shows the ideal property (lesser lattice vibration and scattering effect) for our devices.

2.4.2 Thermal Resistivity

Thermal conductivity is yet another important parameter for many new MEMS applications. The performance and reliability of these MEMS devices are influenced by the degree to which they can conduct heat [26]. The thermal conductivity of thin film material also change significantly from that of the corresponding bulk material. The difference in the thermal conductivity of bulk material and thin film material is due to the fact that the thermal transport is lowered by phonon scattering at lattice imperfections and boundaries for small thickness of materials [27]. Hence the thermal conductivity of bulk material is higher than that of thin films. The thermal conductivity of metal is attributed to the movement of conduction electrons (κ_e) and the effect of lattice vibrations, (κ_l), the energy quanta of which are called phonons:

$$\kappa = \ \kappa_e + \kappa_l \tag{27}$$

In metals, the electron movement plays the dominant role while in non-metal is mainly due to the lattice vibrations (phonons).

$$\kappa \cong \ \kappa_e \tag{28}$$

The movement of the conduction electrons is prevented or delayed by scattering, resulting due to the interactions between electrons and phonons, thickness of metal film, and well as interactions between electrons, impurities and imperfections that may exist in materials. These electron- scattering mechanisms is given by:

$$\frac{1}{\kappa_e} = \frac{1}{\kappa_p} + \frac{1}{\kappa_i} \tag{29}$$

The phonon scattering resistivity (κ_p^{-1}) and the impurity-scattering resistivity (κ_i^{-1}), according the electron conduction theory depends on absolute temperature [20]:

$$\frac{1}{\kappa_p} = a_p T^2 \qquad\qquad \frac{1}{\kappa_i} = \frac{a_i}{T} \tag{30}$$

Whereas, a_p and a_i and two characteristic coefficient constants of metals. From equation (30), it can be deducted that at low temperatures the thermal resistivity is due to primarily to impurity scattering and that the effect of phonon scattering plays an important role at high temperatures. Equating equations (28), (29) and (30) the dependence of thermal conductivity of metal on temperature:

$$\kappa = \frac{1}{a_p T^2 + (a_i/T)} \tag{31}$$

In a thin metal film with thickness >100nm, the phonon scattering effect is overwhelms by the impurity and imperfection scattering effects over a wider temperature domain. Consequently the formulae can be simplified to

$$\kappa = \frac{1}{a_p T^2} \tag{32}$$

A fairly good estimation of the thermal conductivity at temperature above room temperature for thin film materials is done. According to the electron conduction theory there also exists a relationship between the electron transport of energy (thermal diffusion) and the transport of electricity (electrical diffusion), which plays a major role in the determining the thermal conductivity of a material. Generally, metals that are best electrical conductors are also considered to be the best thermal conductors with high thermal conductivity. At a given temperature T, the thermal and electrical conductivities of metals are proportional, but raising the temperature increases the thermal conductivity κ while decreasing the electrical conductivity (σ). This behaviour is quantified using Wiedemann-Franz (WF) Law:

$$\frac{\kappa}{\sigma} = L\,T \quad (\text{Or}) \quad \kappa = L\,T\,\frac{1}{\rho} \tag{33}$$

Where, ρ is the electrical resistivity of the metal and the constant of proportionality L is called the Lorenz Number. For metals the value of L is considered to be universal constants

$$L = \frac{\pi^2 k^2}{3e^2} = 2.45 \times 10^{-8} \; (\text{V/K})^2 \tag{34}$$

The Table X, lists the different thermal conductivity values for 300nm thin film and respective bulk material conductivity evaluated using the WF law for the list of materials.

Materials	Thin film conductivity [W.m^{-1}.K^{-1}] In range (27^{0}C-100^{0}C) Film thickness 300(nm)	Bulk Conductivity [W.m^{-1}.K^{-1}]
Titanium	16.8	21.9
Aluminium	200	275
Indium Tin Oxide	10.2	12

Table X: thermal conductivity of bulk and thin film metals for different materials

2.4.3   Emissivity and Specific heat

The total emissivity ε of titanium has been studied and in literature there are values estimated for this parameter. These values assume a smooth surface. Because in this work titanium is deposited onto a very smooth crystal surface, it can be assumed smooth and the emissivity values from literature do not need to be modified as listed in Table XI:

Temperature [K]	366	478	589	700	811	922	1033	1144	1255
Total emissivity	0.3	0.3	0.3	0.3	0.31	0.31	0.32	0.35	0.41

Table XI: Estimated total emissivity of Titanium thin film of 300(nm)[28]

The specific heats for the titanium thin film is assumed to be similar to those of the bulk as listed in Table XII:

Temperature [K]	300	350	400	500	600
Specific heat [J/kg· K]	129	129	130	133	136

Table XII: the estimated specific heat for the titanium thin film of 300(nm)[29]

Each of this material plays a different role as microheater material with their pros and cons. Aluminium is commonly used as thin film materials with low resistivity values making them ideal for microheaters material with high conductivity. Although in case of aluminium a thin oxide layer is formed on the surface when expose to atmosphere after a while, thereby varying (generally increasing) the resistivity of the thin film. This makes aluminium a less stable material for microheaters. Indium Tin oxide has been widely used as a conductive transparent coating. Titanium has a high melting point, low density and remains resistance to corrosion in various conditions due to the thin layer of oxide formation on its surface makes it's a desirable material for microheaters In addition Titanium has a good adherence property with LiNbO$_3$ substrate making it an ideal material for our micro-heaters.

Parameter	Aluminium	Titanium	ITO	LiNbO$_3$
Heat capacity at constant pressure (C_p) [J/kg*K]	223	129	58	628
Electrical Resistivity (ρ) [$\mu\Omega$.m]	0.1043	1.7356	681.58	2.63e-9
Density (rho) [kg/m^3]	2700	4506	7120	4700
Thermal conductivity (k) [W/(m*K)]	200	16.8	10.2	5.6

Table XIII: The material properties of microheater and pyroelectric substrate (LiNbO$_3$) taken for the purpose of numerical and experimental analysis.

References:

[1] G. velmati, N. Ramshanker and S. Mohan, "2D simulations and electro- Thermal Analysis of micro-Heater Designs Using COMSOL for Gas Sensor Applications," *Applied Physics,* Vols. 308-309, 2010.

[2] Mahony, C. O., Hill, M., Hughes, P. J., and Lane, W. A. (2002). Titanium as a micromechanical material. *Journal of micromechanics and microengineering , 12*, 438-443.

[3] Peirs, J., Reynaerts, D., and Brussel, H.V. (1998). Scale effects and thermal considerations for micro-actuators. *International conference on Robotics and Automation*, Leuven Belgium.

[4] Asheghi, M., Leung, Y.K., Wong, S.S., and Goodson, K.E. (1997). Phonon-boundary scattering in thin silicon layers. *Applied Physics letters,* vol. 71, p. 1798.

[5] Thuau, D., Koymen, I., Cheung, R., (2011). A microstructure for thermal conductivity measurement of conductive thin films. *Microelectronics engineering*, 88, 2408-2412.

[6] M. Riccio, A. Pantellini, A. Irace, G. Breglio, A. Nanni, C. Lanzieri, Electro-thermal characterization of AlGaN/GaN HEMT on Silicon Microstrip Technology, Microelectronics Reliability, Volume 51, Issues 9–11, September–November 2011, Pages 1725-1729, ISSN 0026-2714, http://dx.doi.org/10.1016/j.microrel.2011.07.003.

[7] Neidholdt, L. E., and Beauchamp, L. J. (2007). Compact ambient pressure pyroelectric ion source for mass spectrometry. *Analytical chemistry , 79*, 3945-3948.

[8] Link,S., Mohamed, M.B., El-Sayed, M.A, (1999). Simulation of the optical absorption spectra of gold nanorods as function of their aspect ratio and the effect of the medium dielectric constant: *J Phys Chem B*, 103: 3073-3077.

[9] Fujii, M., Zhang, X., Xie, H., Ago, H., Takahashi, K., Ikuta, T., Abe, H., Shimizu, T., (2005). Measuring the thermal conductivity of a single carbon nanotubes: *Phys Rev Lett*, 95:065502.

[10] Wang, X.W., Fei, G.T., Zheng, K., Jin, Z., Zhang, L.D., (2006). Size dependent 100melting behavior of Zn nanowire arrays: *Appl Phys Lett*, 88:173114.

[11] Bilalbegovic, G., (2000). Structures and melting in infinite gold nanowires: *Solid State Commun*, 115:73-76.

[12] Qi, W.H., Wang, M.P., Zhou, M., Hu, W.Y., (2005). Surface area difference model for thermodynamics properties of metallic nanocrystals: *J Phys D: Appl Phys*, 38: 1429-1436.

[13] Eaton, W.P., Smith, J.H., (1997). Micromachined pressure sensors: review and recent developments: *smart materials and structures*, 6(5).

[14] Krulevitch, P., Lee, A.P., Ramsay, P.B., Trevino, j.C., Hamilton, J., Northrup, M.A., (1996). Thin film shape memory alloy microacutuators: *IEEE J. of Microelectromechanical systems*, 5: 270-282.

[15] A. Matthiessen (1862), *Rep. Brit. Ass*, 32:144.

[16] A. Matthiessen (1864), *Progg. Anallen*, 122:47.

[17] Fuchs,K., (1938). The conductivity of thin metallic films according to the electron theory of metals: *Proc Camb Philos Soc*, 34:100-108.

[18] Sondheimer, E.H., (1952). The mean free path of electrons in metals, *Advance Physics*, 1:1-42.

[19] Rossnagel, S.M., Kuan, T.S., (2004). Alteration of Cu conductivity in the size effect regime, *J Vac Sci Technol B*, 22:240-247.

[20] Camacho, J.M, Oliva, A.L., (2005). Morphology and electrical resistivity of metallic nanostructures, *Microelec J*, 36: 555-558.

[21] Yarimbiyik, A.E., Schaff, H.A., Allen, R.A., Zaghloul, M.E., Blackburn, D.L., (2006). Modeling and simulation of resistivity of nanometer scale copper, *proceeding if the 11th asia and south pacific design automation conference*: January 24-27, yokohama 503-508.

[22] Fan, P., Yi, K., Shao, J.D., Fan, Z.X., (2004). Electrical transport in metallic films, *J App Phy*, 95: 2527-2531.

[23] Zhang, W., Brongersma, S.H., Ricard, O., Brijs, B., Palmans, R., Froyen, L., Maex, K., (2004), Influence of the electron mean free path on the resistivity of thin metal films, *Microelelectron eng*, 76: 146-152.

[24] Fred L., (2011). Developing a theretical relationship between electrical resistivity, temperature and film thickness for conductors, *Nanoscale research letters*, 6: 636.

[25] F. Lacy, "Developing a theoretical relationship between electrical resistivity, temperature and film thickness for conductors," *Nanoscale research journal,* p. 6:636, 2011.

[26] Asheghi, M., Leung, Y, K., Wong, S, S., Goodson, K, E., (1997). Phonon-boundary scattering in thin silicon layers, Appl. Phys. Lett., 71:1798.

[27] Sculock, R.G., "Low temperature behavior of solids: An introduction", dover, new york, 1966, 51-64.

[28] https://www.omega.com/literature/transactions/volume1/emissivitya.html

[29] www.engineeringtoolbox.com/specific-heat-metals-d_152.html

Chapter 3
Thermal behaviour

## 3.1 Result of the thermal analysis

We perform simulations on four different shapes of micro-heaters: S-shape, fan shape, meander shape and double spiral shape. Simulations are performed with same initial and boundaries conditions as described in previous 2.2.2. We are interested in temperature distribution on the top crystal surface, thus we present, for each micro-heater, the thermal map of the top crystal surface and thermal profiles took out of cut-lines of the same surface.
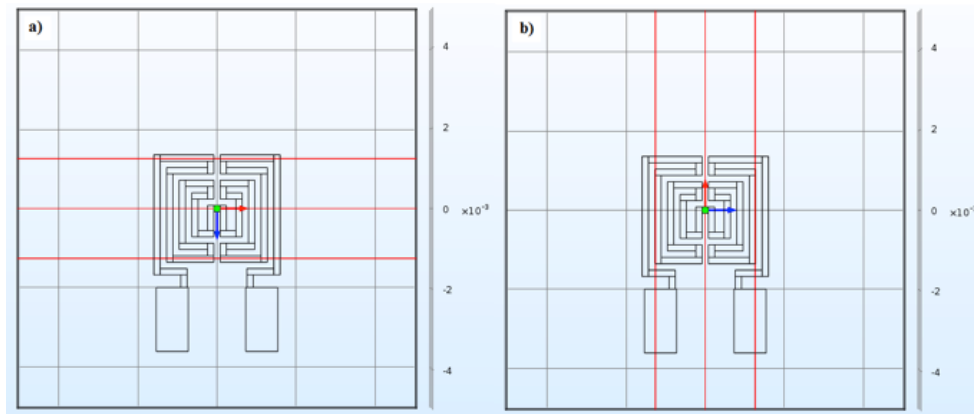
Fig 26: Cut lines along X and Y directions for the Fan shape microheater.

Thermal profiles along x and y directions are the better way to investigate about temperature distribution, because they give us a point of view of temperature uniformity on the entire surface we are interested in. Thermal maps and thermal profiles are presented and compared to each other, in order to find out which is the more efficient shape of microheater for the PE analysis.

39
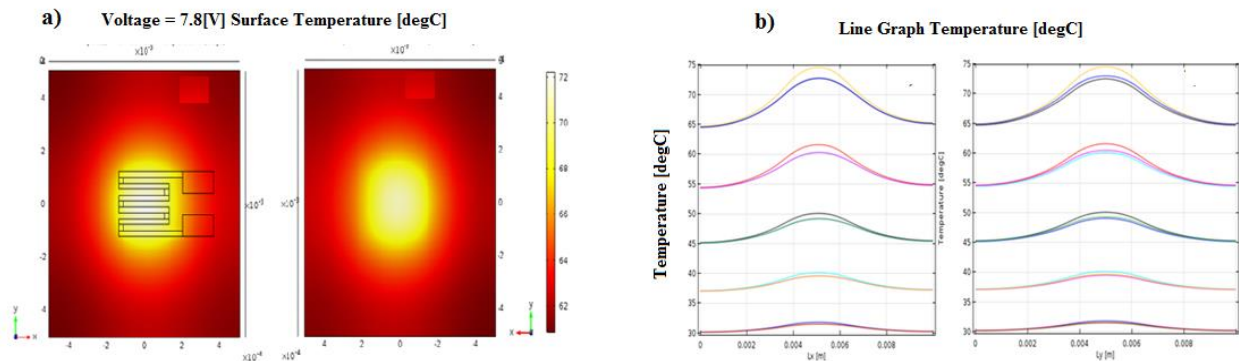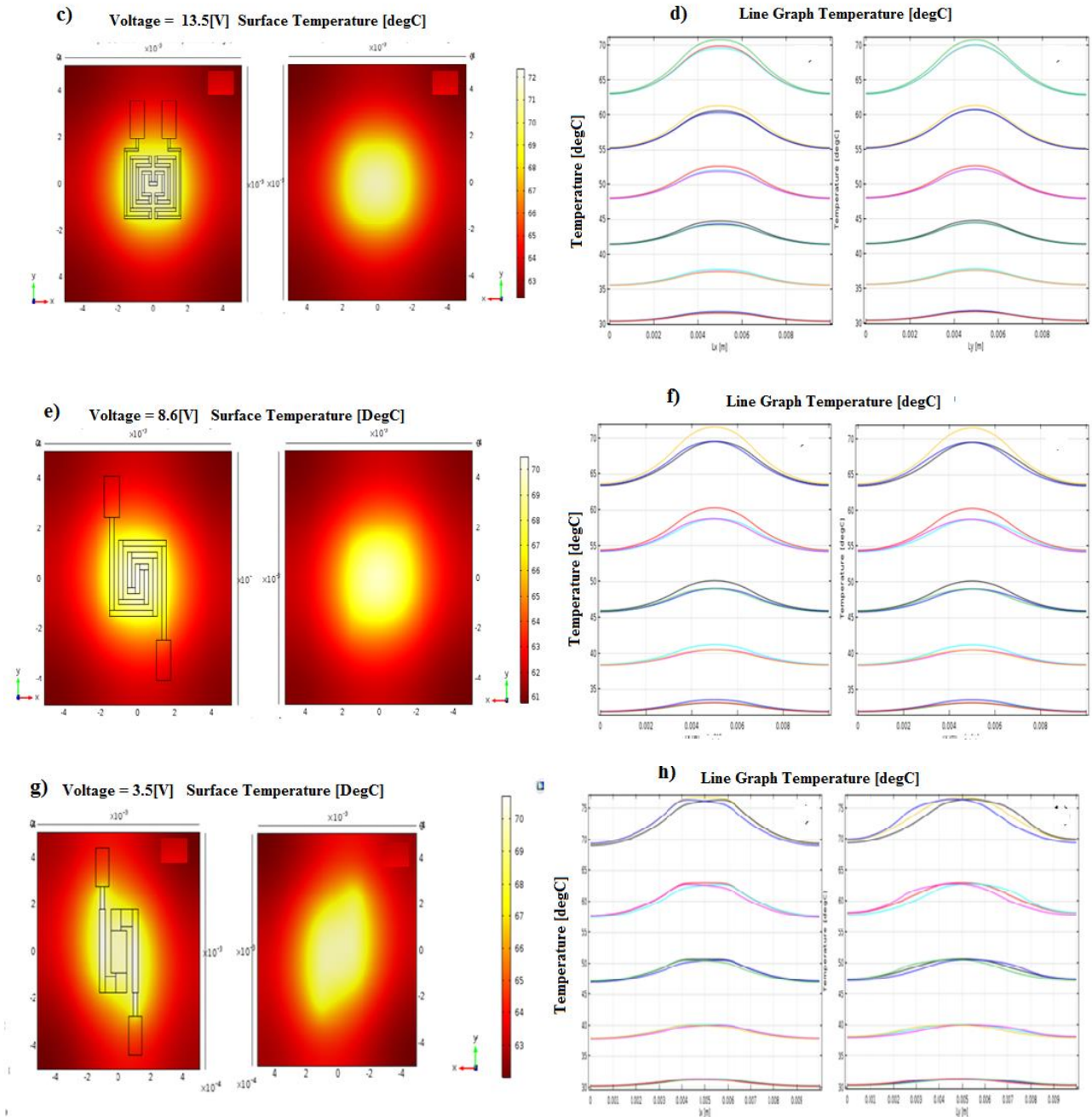
Fig27: Thermal maps of the top and bottom surface of the LN crystal surface and the thermal profile along X and Y directions for a), b) meander, c), d) fan, e), f) spiral g), h) S-shape microheater for applied power 60mW, 120mw, 180mW, 240mW and 300mW.

In the figure27, we report thermal maps of the crystal bottom surface, identified by the presence of the micro-heater, and of the top surface that represents our focus. Thermal map gives us a qualitative image about temperature distribution on the surface, with association of different colours at different powers applied and the respectively obtained temperatures. For a quantitative analysis of temperature distribution, we present thermal profiles of top crystal surface, at different temperature levels. Applying different value of the electrical power (terminal voltages) we start from a temperature of about 30°C to reach approximately at 75°C.

3.2   Steady Thermal Analysis

Thermal analyses of the microheater designs were performed using COMSOL simulator and an infrared setup [1-2]. The core of the IR system is the FLIR SC7000 camera equipped with a 640×512 InSb sensors focal plane array [Appendix A.2.]. The acquired COMSOL simulated and thermo camera thermal maps and the relative profiles along the line AA' from the –Z surface of LiNbO$_3$ are reported in Fig. 28, Fig. 29 and Fig. 30 respectively.
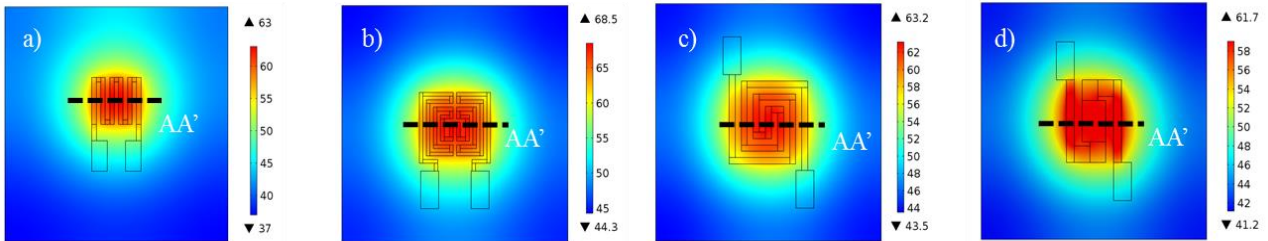

Fig 28: COMSOL simulated thermal maps of the four different microheater designs: a) meander, b) fan, c) spiral and d) S-shape.
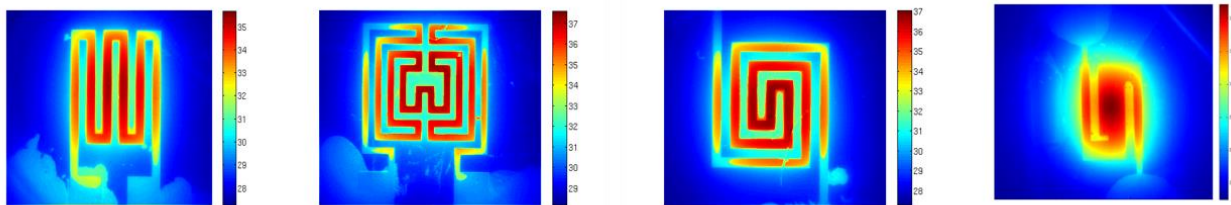
Fig 29: FLIR thermos camera thermal maps of the four different microheater designs: a) meander, b) fan, c) spiral and d) S-shape.

Note1: MATLAB Code for post processing the obtained thermocamera images in appendix A.3.2.
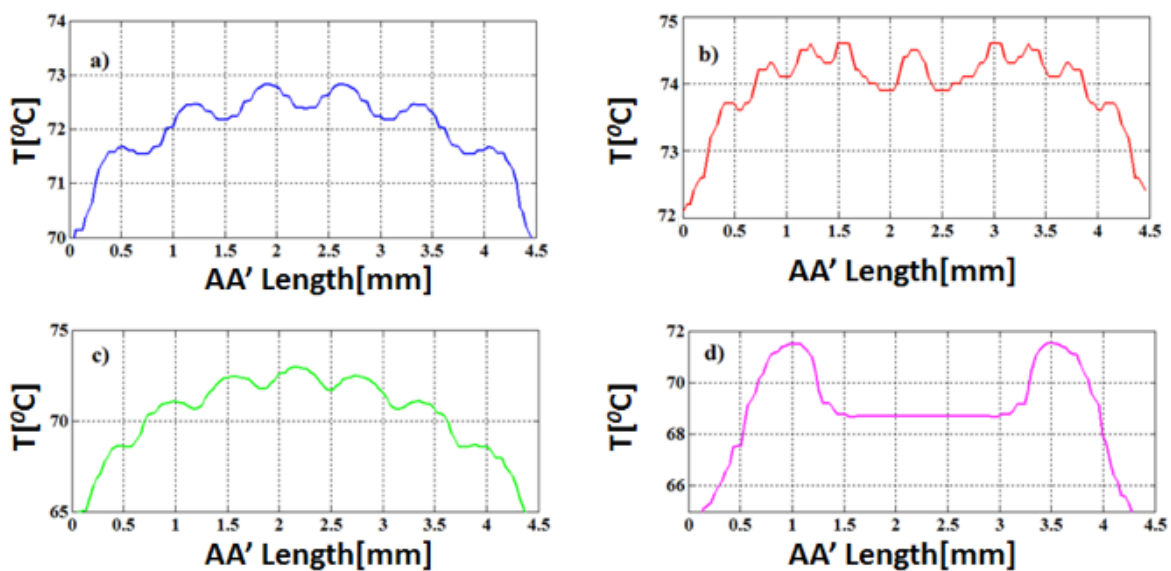

Fig 30: Simulated Temperature transverse profile of the microheater designs along AA' at 350mW: a) meander, b) fan, c) spiral and d) S shape.

In particular, in Fig.30 the temperature profiles along the line AA' obtained for an applied power of 350mW are shown. It can be observed, due to their different geometries, each structure has different temperature profile distribution. As reported in next paragraphs, these differences have a preeminent influence on the electric field analysis and thus pyroelectric emission from the –Z surface of the crystal. The thermal maps measurements allows measuring the temperature reached on the –Z surface of LiNbO3 for different applied electrical powers. These values were compared with the experimental data and illustrated in Fig. 31.
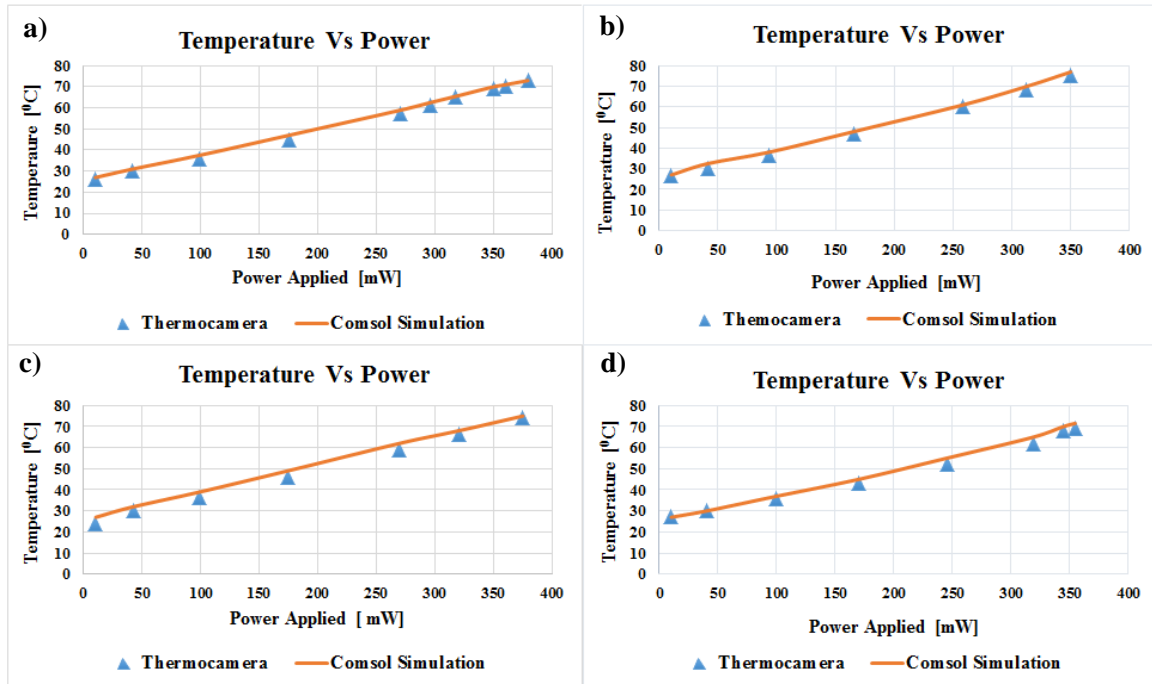
Fig 31: Temperature vs. power plot for different designs at the centre of the of microheaters structure a) meander, b) fan, c) spiral and d) S-shape estimated using simulator and observed by thermo camera.

The numerical model assumed for the microheater shows a good agreement with the experimental analysis. The maximum temperature experimentally attained on the crystal was about 75°C for each microheater, above this temperature the crystal develops cracks initially and finally breaks.

3.3   Transient Thermal Analysis

In addition to the steady state analysis, transient studies were also carried out (both experimentally and numerically) by applying an appropriate voltage square pulse waveform for 350mW electrical power with a heater-on-time of 4[s] using a pulse generator. The acquired thermal maps and relative transient profile at point A' reached on –Z surface of LiNbO$_3$ using the thermal camera are shown in Fig 32 and Fig 33 respectively. In Fig. 33a and Fig. 33b shown the measured and simulated transient temperatures reached on –Z surface of LiNbO$_3$, respectively.
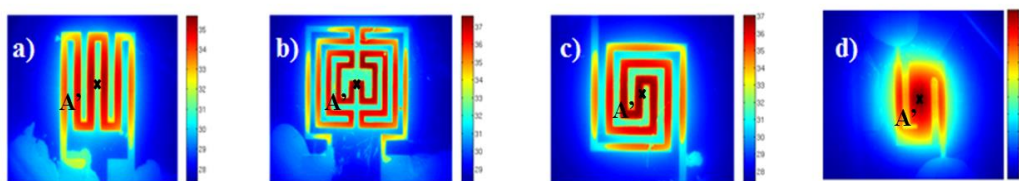
Fig 32: Thermo-camera measurement of the four different microheater designs: a) meander, b) fan, c) spiral and d) S-shape.

42
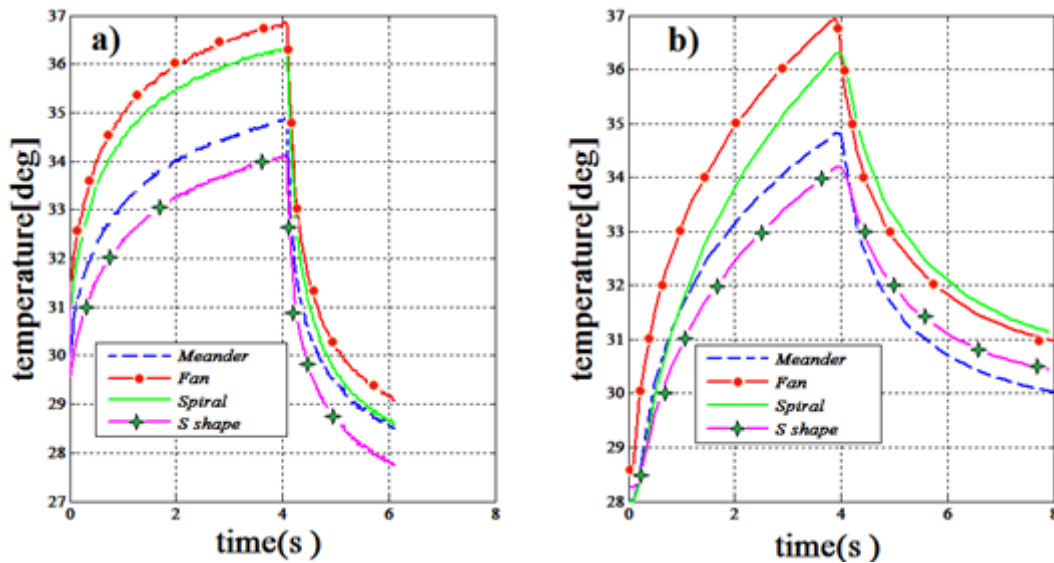
Fig 33: Experimental and numerical transient analysis of microheater designs with eater-on-time of 4s: a) Thermo camera measurement, b) COMSOL^{TM} measurement.

The maximum temperature reached in transient condition for each microheater shows similar result for both simulated and experimental analyses. On the other hand, the rates of heating and cooling are different between the measured and simulated data. The different behaviour could be explained with the experimental conditions used to perform the experimental measurement. In particular, the con-tact and thermal resistance between the pads and connecting wire, humidity and room temperature. In Table XIV the extracted time constant for the heating and cooling phase are reported.

	Heating [s]	Cooling [s]
Mender	2	0,41
Fan	3,2	0,40
Spiral	2	0,39
S-Shape	2	0,1

Table XIV: Time constant for the heating and cooling phase.

Heating and cooling basically depends on the heat exchange between the micro-heater and the environment source (air). The rate of cooling is faster since the temperature differential between the air and the heated microheater is very high resulting in the higher heat exchange, while rate of heating is slower resulting in the low heat exchange during process. Other investigations were also performed using COMSOL™, for Heater on times for 1s and 50s (see fig 34) were also investigated in the simulation at different step voltages (electrical power).
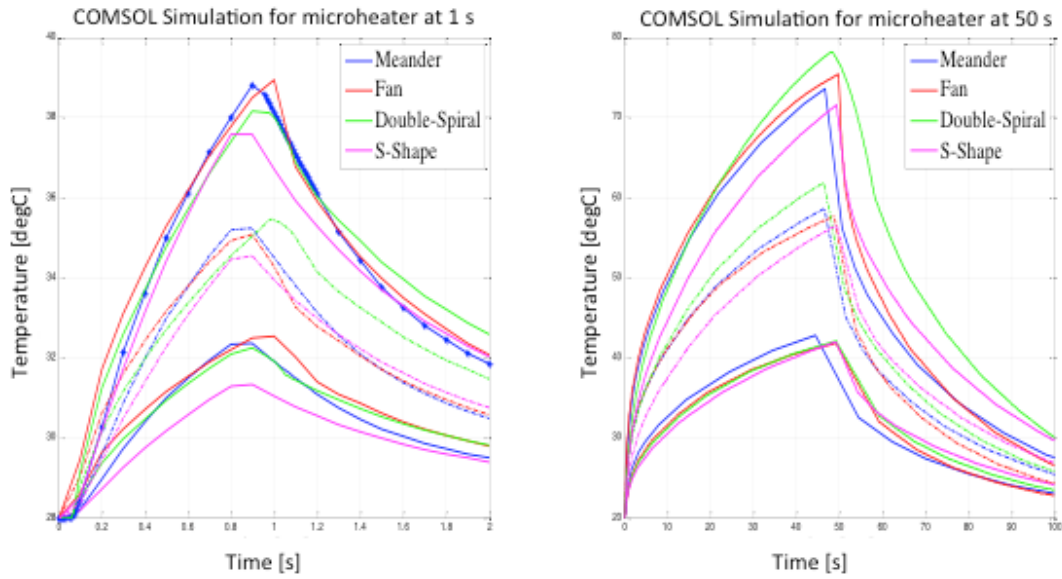
Fig 34: Theoretical analysis of microheater using COMSOL at different power dissipation with heater on time for 1s and 50 s at electrical power 100mW, 200mW, 300mW.

Among the four microheater designs, fan shape heater produces the highest temperature due to its higher track length followed by spiral and meander, where S shape microheater produces a uniform heating zone on the − Z LiNbO$_3$ surface.

References:

[1] G. Romano, M. Riccio, G. De Falco, L. Maresca, A. Irace and G. Breglio, "An ultrafast IR thermography system for transient temperature detection on electronic devices," 2014 Semiconductor Thermal Measurement and Management Symposium (SEMI-THERM), San Jose, CA, 2014, pp. 80-84. doi: 10.1109/SEMI-THERM.2014.6892219

[2] Comsol A. *COMSOL multiphysics user's guide.*

Chapter 4
Pyroelectric Investigations

4.1   Electrical Field Analysis

The evaluation of the electric field analysis was further analyse considering two major factor: 1) at constant tip to -Z surface gap of 100 µm for different designs of microheaters, 2) at different tip to –Z surface gap spacing for fan shape microheater.

4.1.1   Electrical field analysis of the microheater designs at constant tip to –Z surface gap of 100 µm.

The electric field strength simulation was further analysed between –Z surface of the LiNbO$_3$ crystal and a beryllium metallic probe of tip radius 1µm, with a height of 1.5mm. The probe was designed at a gap of 100µm from –Z surface crystal immersed inside an air box (see Fig. 19). Heat transfer at fluid (air) interface was considered for the air box with an absolute pressure of 1atm. The acquired electric field strength with their respective temperature attained by the microheaters at 300mW electrical power along the xy cut-plane are shown in fig 35.
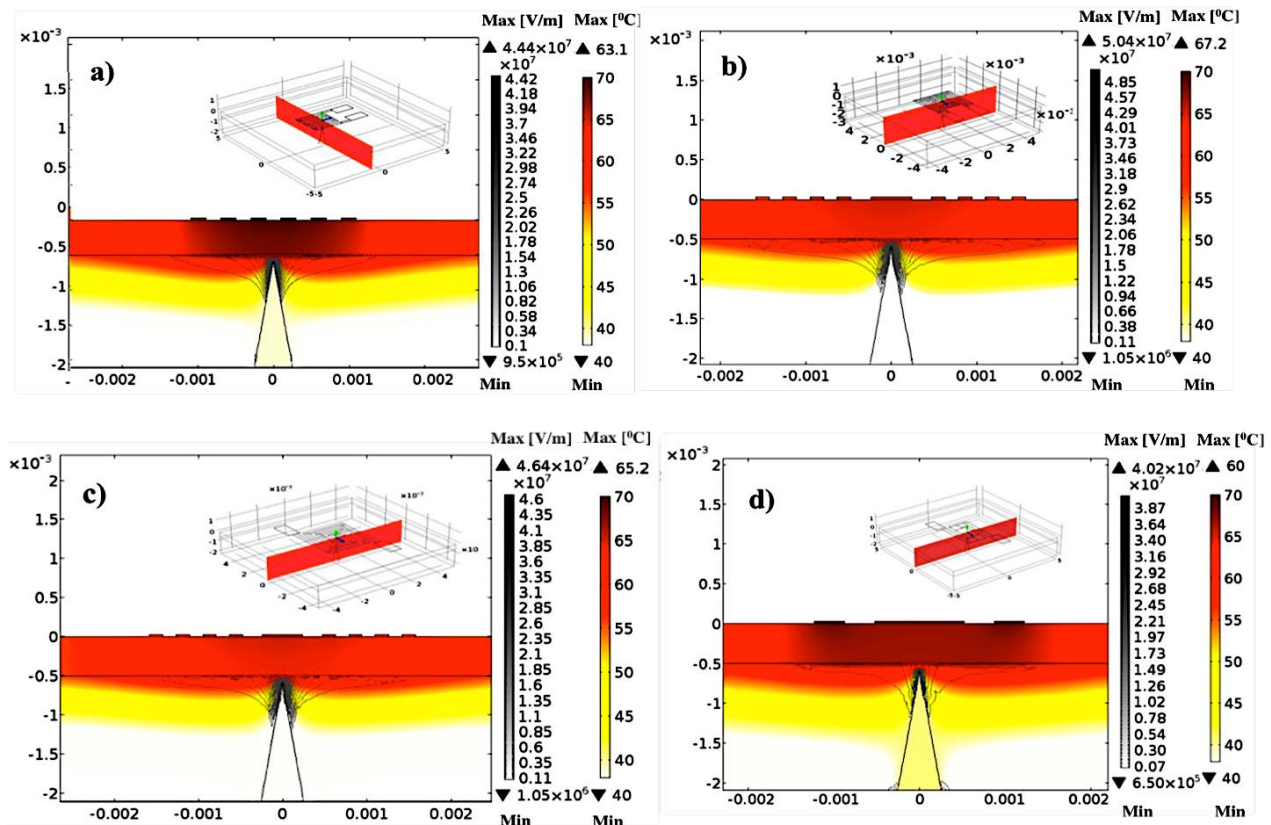

Fig 35: Electric field analysis along the XY plane (inset images) of each microheater designs: a) meander, b) fan, c) spiral and d) S shape.

It was observed that the fan shape microheater yields to have a higher electrical field strength for applied electrical power of 300mW compared to the other designs. This behaviour is attributed to the temperature transverse profile distribution due to different shape and the spacing between the heater tracks (see Fig. 30) [1].

4.1.2 Electrical field analysis for the fan shape microheaters at different tip to –Z surface gap spacing

Electric field strength was further analysed for the fan shape microheater at different tip to –Z surface of LiNbO$_3$ gap spacing, as fan shape design tends to produce comparatively higher electric field strength (see Fig. 35). A parametric sweep simulation was performed at different tip distances from the –Z surface of LiNbO$_3$ in range between 0.1mm to 1mm (Fig. 35). However, analogues simulations were also performed for the other microheater designs and the resulting electric field is plotted in figure 37.
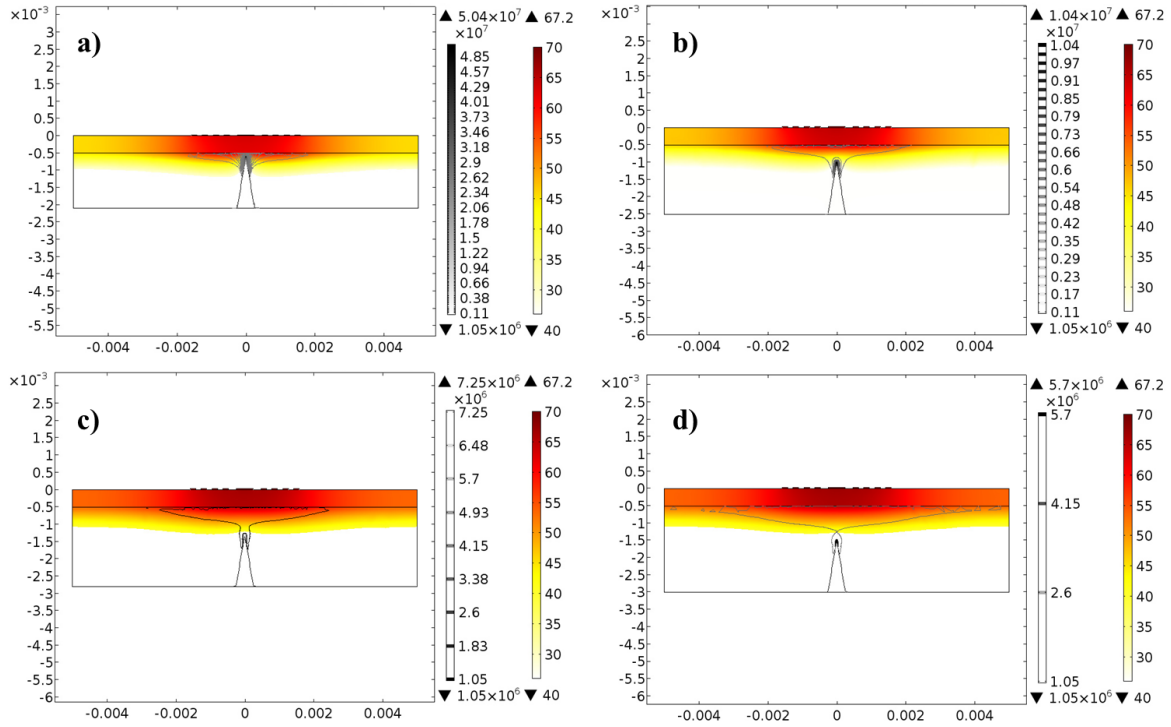
Fig 36: Electrical field analysis for the fan microheater at different tip to –Z surface gap spacing: a) 0.1[mm], b) 0.5[mm], c) 0.75[mm] and d) 1[mm].

The electric field decrease with the increase in the gap spacing between the tip and –Z surface of the crystal. An estimation of the electric field data can be evaluated as a function of gap spacing between the surface and the metallic probe using the equation 35 [2]; i.e.:

$$Egap = A\left(\frac{\gamma \cdot \Delta T}{\varepsilon_0}\right) * \left[\frac{1}{1+\left(\frac{dgap}{dcr}\right)*\varepsilon_{cr}}\right] \tag{35}$$

Where, ε_0 is the permittivity of free space, $dgap$ is the tip to sample distance, ε_{cr} is the permittivity of the crystal, dcr is the crystal thickness and A is a geometrical factor taking into account that the electrode is not flat surface but with a needle form. Studies were already performed to estimate the amplification of the electric field for a prolate spherical tip-to–plane geometry [28]. It would be modest to consider only the area of curvature in our case for the field enhancement factor as the tip has a radius of 1μm. In Finite element analysis (FEA) simulator such as COMSOL multiphysics, these parameters are already taken into account using the Fowler-Nordhiem equation. Moreover, the previous formula is valid for a vacuum gap; for atmospheric conditions the presence of free charges, which compensate the polarization charges from the crystal surface, have to be taken into account. A comparative steady state electric field analysis was performed in a vacuum and air conditions (room temperature 27^{0}C) using equation 35 and COMSOL simulation for all

the microheater designs at different tip-to-surface gap spacing for an applied electrical power of 350mW (see Fig. 37).
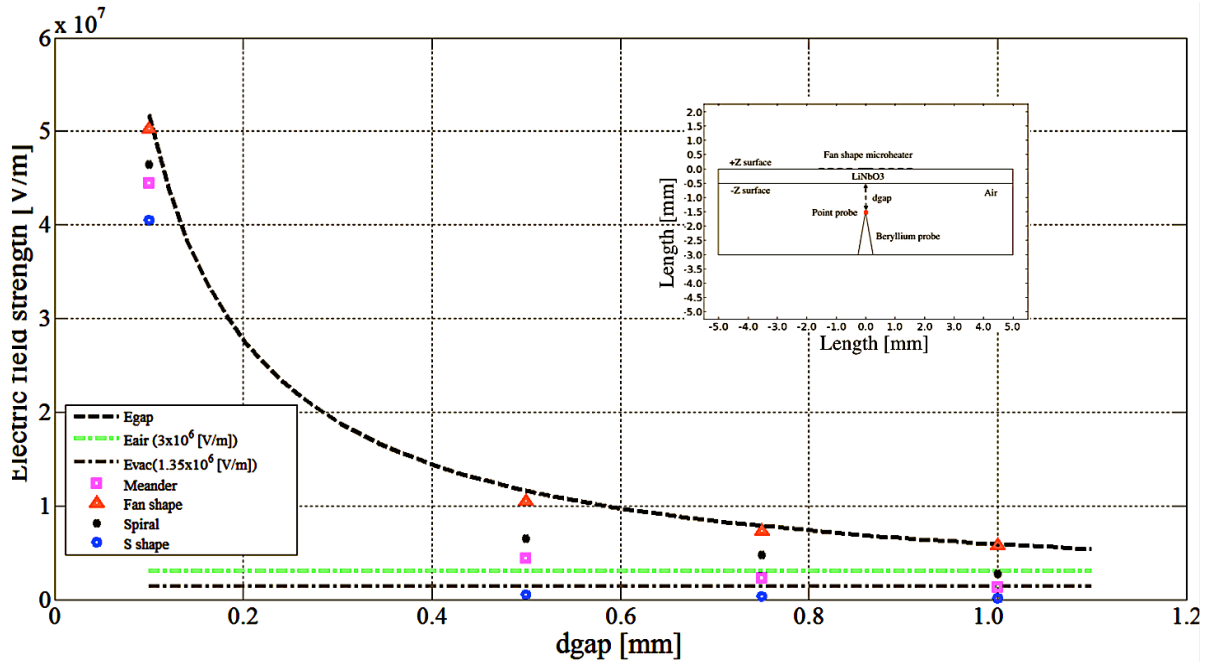

Fig 37: Electric field vs. probe tip to surface gap spacing for the microheater designs.

The obtained data for the electrical field in vacuum shows a good agreement with respect to the simulation results. Henceforth, at shorter gap spacing <1mm equation 35 can be used to approximate the electric field generated in a normal atmospheric conditions between the tip and the –Z surface of LiNbO$_3$. It is further shown experimentally how the electric field generated for different microheater designs and tip to surface gap effects the pyroelectric emission from the –Z surface of the LiNbO$_3$ crystal.

4.2   Metallic point probe measurement setup

In order to evaluate the pyroelectric effect, the setup schematically illustrated in Fig 38 was adopted. In particular, a 10mm × 10mm × 500µm pyroelectric LiNbO3 sample with the afore-described microheaters on the +Z face, was mounted with the –Z face exposed to a suspended metallic tip used to monitor electrical activity on the crystal surface. The LiNbO$_3$ +Z surface is heated by the fabricated microheater. Microheater is driven by a periodic pulse waveform, while a metallic tip is placed near the –Z face to monitor the pyroelectric effect using an oscilloscope.
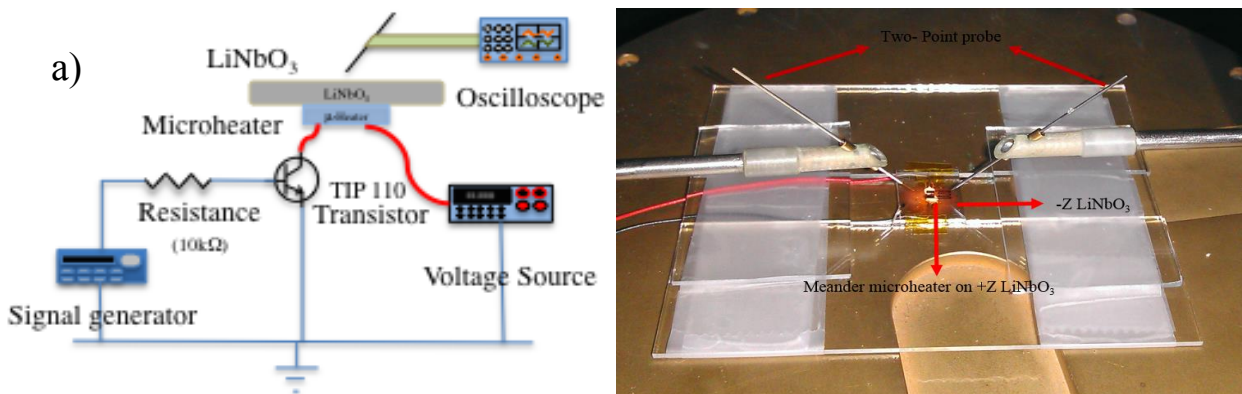

Fig 38: a) Schematic of experimental setup; b) Two probe point setup.

When the temperature of the sample is stationary, the polarization of the pyroelectric material is compensated by free charges (electrons or ions) from the ambient condition [3-5]. If a voltage is applied to the microheater, during the transient an electrical power is dissipated in the form of heat and thus the temperature of the crystal increases. Consequently, the spontaneous polarization decreases and net surpluses of compensating positive charge on the -Z face are obtained. Thus, an electrical field is induced between the –Z face and the point like metallic tip. This field charges the interelectrode capacitance, which includes the parasitic capacitances and the oscilloscope capacitance. If the electrical field is enough strong to induce an air breakdown, the interelectrode capacitance can discharge themselves through the low impedance formed by the discharge between the metallic tip and the –Z face. The oscilloscope records the voltage drop at breakdown and a negative current impulse is observed. As the microheater is switched off, the cooling transient induces an increase in polarization and net deficits of compensating positive charge on the -Z face. Thus, a positive current impulse can be observed at the oscilloscope. Obviously, the impulse occurrence is strictly dependent on gap-spacing distance between the crystal surface and the metallic tip. In particular, the induced electrical field as function of the gap spacing that can be estimated by equation (35) [4,6].

In our experiment, a metallic tip with a point radius of 1μm (see Fig. 39) was positioned on the –Z face at the centre of the area heated by the microheater where the temperature variation is higher and thus the pyroelectric effect is greater.
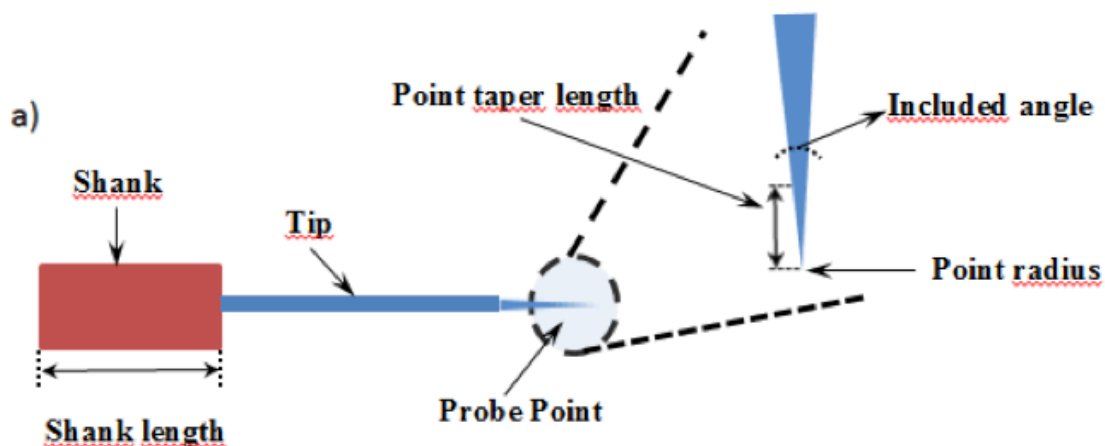
| Model Number	Tip diameter [μm]	Point radius [μm]	Point Tapper Length [mm]	Included Angle [degree]	Overall length [mm]	Shank Diameter [mm]	Material	Attributes
Micro manipulator Model 7H	508	1.0	3.43	8	0.508	35.56	Beryllium Copper	Low contact angle

Fig 39: a) Schematic of the Probe tip, b) probe tip specifications.

4.3 Pyroelectric Field Investigation

4.3.1 Constant tip to –Z surface distance varying frequency voltage signal

The fabricated microheaters were driven with a periodic square waveform with a frequency of 10mHz, and a voltage adjusted to dissipate an electrical power of 300mW for each microheater. The periodicity of the applied voltage was useful to see the pyroelectric current using the oscilloscope, and to detect the repeatability of the induced pyroelectric effect. The frequency of the waveforms was chosen in order to allow both the thermalization of the pyroelectric crystal during the heating phase and the natural cooling of the pyroelectric

material after the switching off of the microheater. As results from Fig. 31, for the applied electrical power the temperature of the –Z face was about 70-75°C. The distance between the tip and the –Z face was set to 100μm. The picked up waveforms for each microheater are reported in Fig 40.
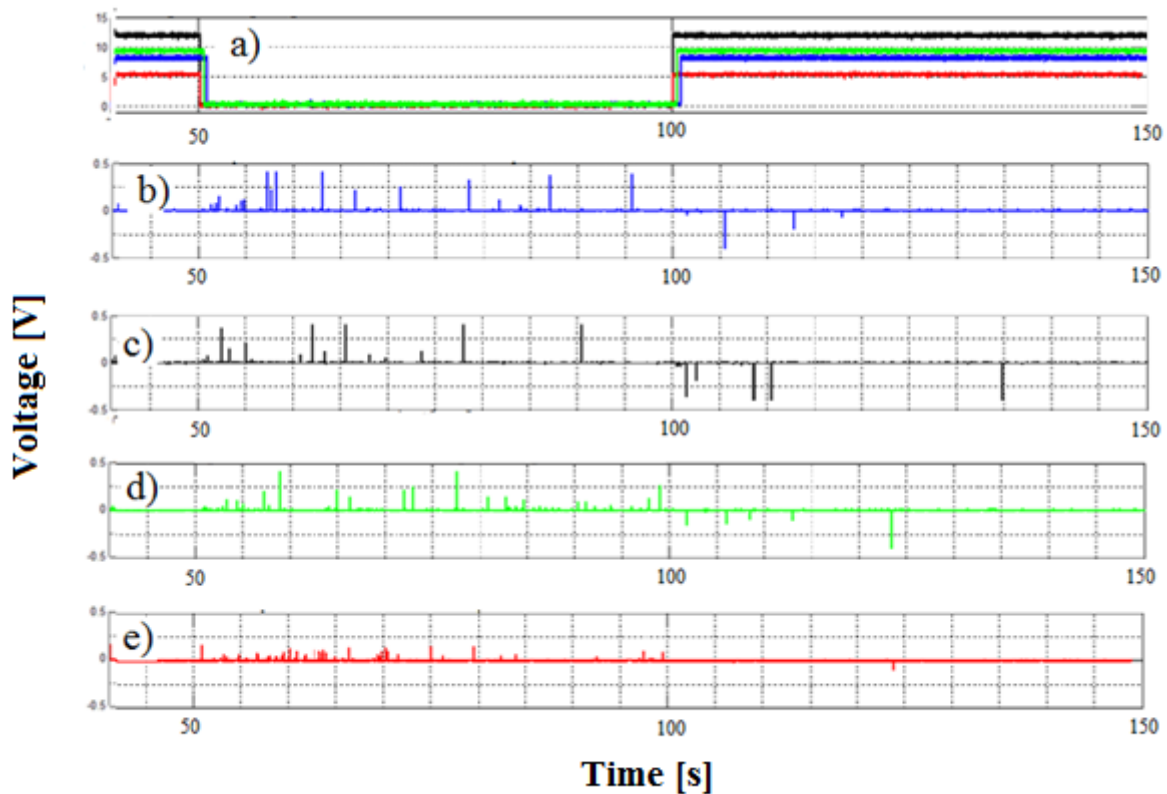
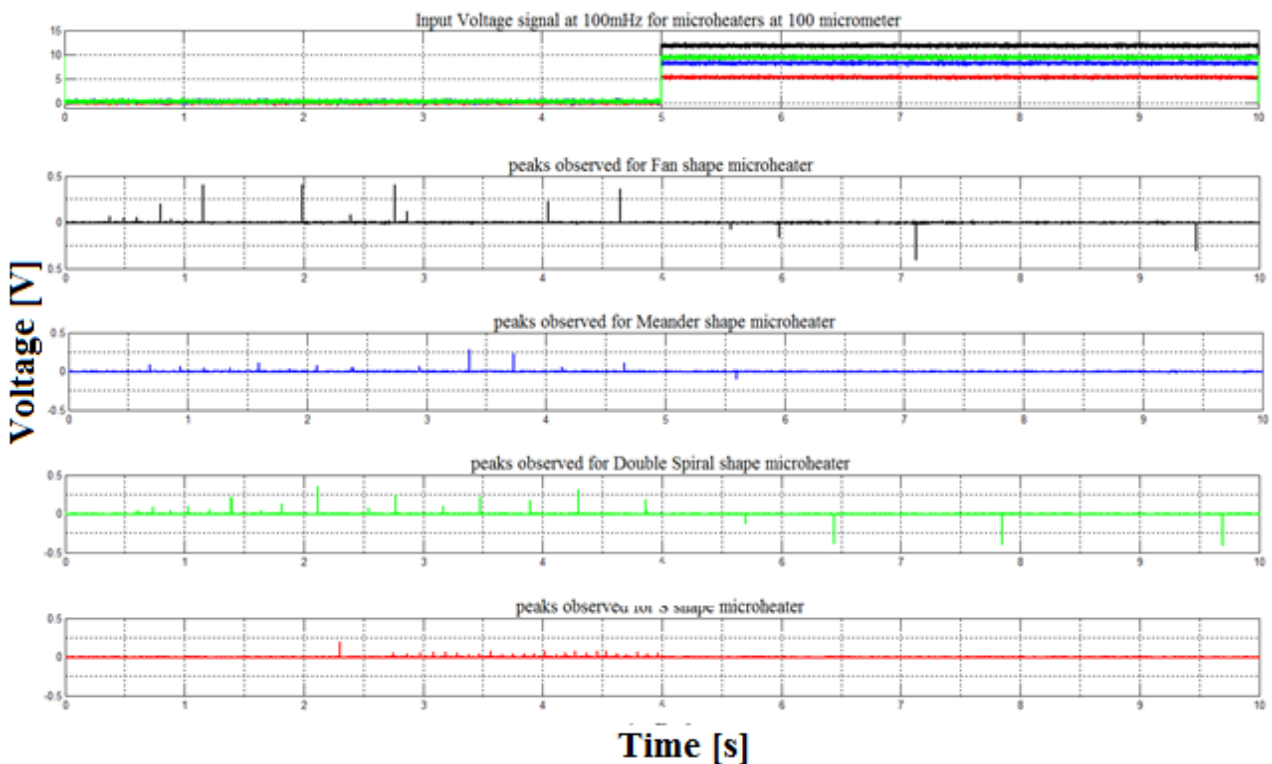***Fig 40: Current impulses obtained for different designs of microheater: a) applied voltage signal to dissipate a power of 300mW at 10mHz b) Meander c) Fan d) Spiral and d) S-shape.***

Higher electric field strength, associated at larger amplitude of current impulses, is obtained for the fan shape μH, while lower amplitude (<150mV) of current impulses was obtained in the S shape μH see Fig. 37.

Higher electric field strength results in the larger amplitude (> 250mV) of current impulses for the fan shape microheater, while lower amplitude (<150mV) of current impulses was obtained in the S shape microheater see Fig. 40. When the microheater is turned on (off), an exponential heating (cooling) of the structure is activated (see Fig. 33). So, a quick change in the rate of change of the temperature is initially induced, causing acceleration in spontaneous polarization variation. As consequence, air breakdown and consequently the occurrence of the current impulses can be happening very often. On the other hand, when the structure is approaching the thermalization, the rate of change of the temperature is slower, and as consequence, current impulses are sparser. Because the cooling phase is faster than the heating one (see Table XIV), in the same period of time, the pyroelectric effect induced in the cooling phase is greater than that one induced in the heating phase. Thus, a larger net surpluses of compensating positive charge on the –Z face are obtained during the cooling phase; as consequence, more impulses are obtained in the cooling period.
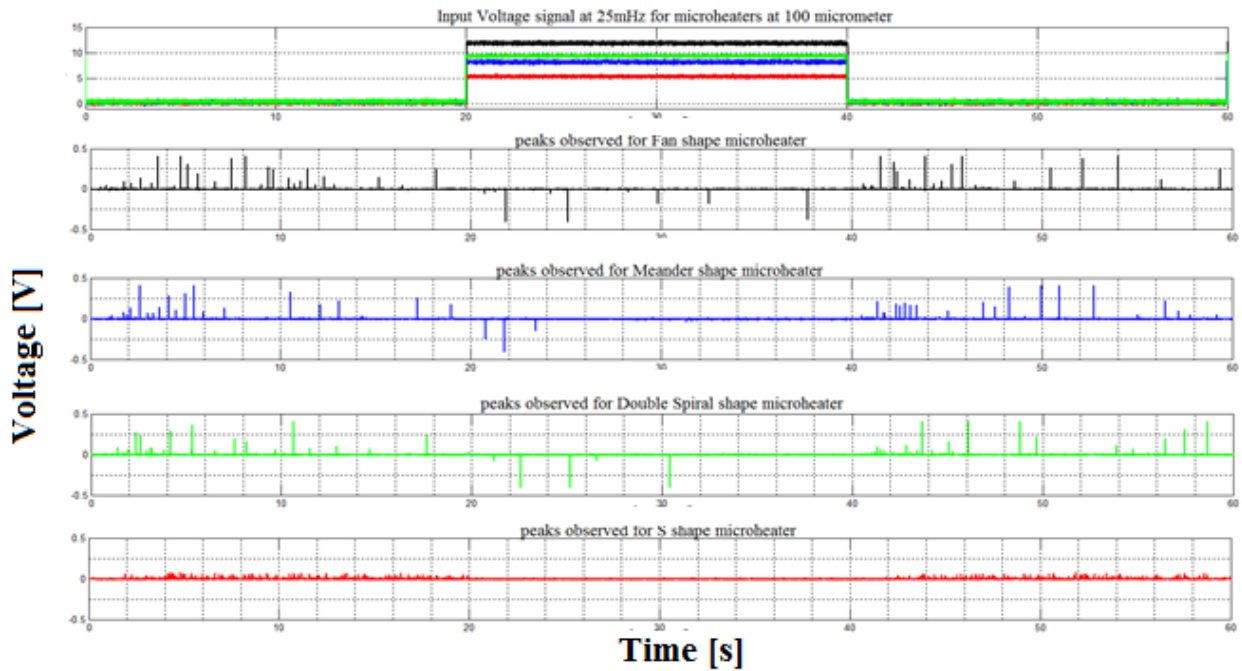
Fig 41: Current impulses obtained for different designs of microheater: a) applied voltage signal to dissipate a power of 300mW at 25mHz b) Fan c) Meander d) Spiral and d) S-shape.
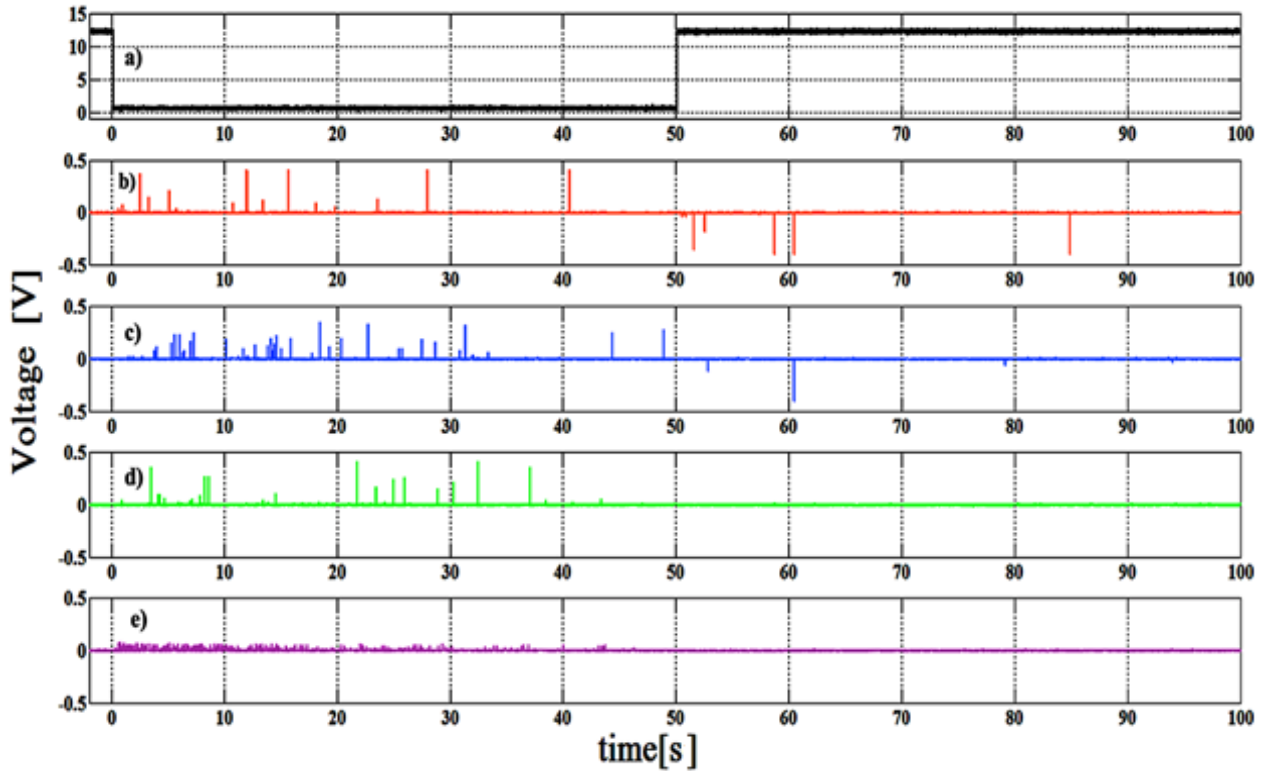

Fig 42: Current impulses obtained for different designs of microheater: a) applied voltage signal to dissipate a power of 300mW at 100mHz b) Fan c) Meander d) Spiral and d) S-shape.

The tip to surface gap spacing at 100μm for lower frequencies of 25mHz and 100mHz were also performed, the obtained peaks can be seen in Fig 41 & 42 respectively. The PE in a frequency domain give the degree of freedom for obtaining and controlling the electron emission from the –Z surface of the LiNbO₃ crystal.

4.3.2   Constant frequency voltage signal varying tip to –Z surface distance

The PE as function of the gap between the surface and the metallic tip was analysed. In particular, a micromanipulator was adopted for varying the tip-surface gap spacing from 100µm to 1mm. The measurements reported in Fig. 43 were performed on fan-shape-based structure by applying a square voltage signal useful for dissipating an electrical power of 300mW at 10mHz frequency.


Fig 43: Current impulses at different gap spacing: a) the applied signal to fan shape microheater, the impulses obtained at b) 0.1(mm), c) 0.5(mm), d) 0.75(mm), e) 1(mm).

During natural cooling (occurring after turning off the heater), current impulses of amplitude approximately greater than 250mV were observed for distances from the –Z surface of crystal ranging from 100µm to 750µm; whereas, lower amplitudes ($<$ 100mV) were detected for $dgap > 750$µm. Finally, as the tip is moved farther from the –Z surface of crystal, the induced electric field decreases at very low values and only few impulses with low amplitudes are present. The experimental results are slightly different from the simulation ones reported in Fig. 37, because the simulations did not take into account the presence of free charges around the crystal surface that compensate the polarization charges induced by the pyroelectric effect.

A similar behaviour was observed during the heating phase, even if the slower trend of this phase induces a weak pyroelectric effect resulting in a few number of current impulses with a small amplitude for a gap spacing $<$ 500µm and no impulses for $dgap >$500µm.

4.3.3   Impulses Occurrence Investigation

One of the main advantages of heating by means of a microheater is the high controllability of the heating process. For example, during heating and cooling phase, the occurrence of the charge emission impulses (i.e. the time shift between the applied voltage switching and the observed impulses) was obtained with a great regularity. In Fig. 44 the occurrence of the first impulse during heating and cooling phases is reported.
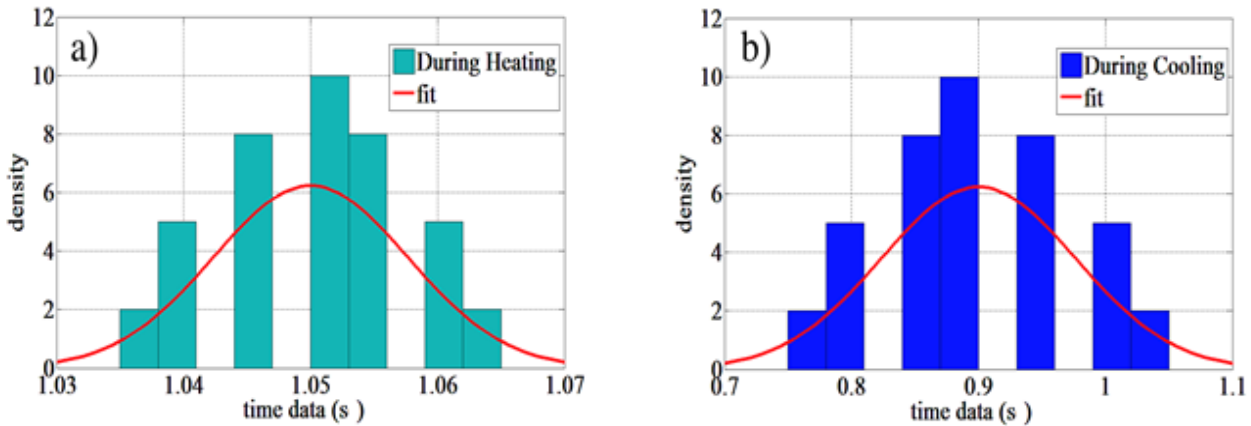
Fig 44: Occurrence of the first impulses with respect to delay time: a) during heating, b) during cooling.

The variance of the Gaussian distribution is 5.9e-3s (5.897e-5s) during the heating (cooling) condition. The higher repeatability of the first impulse during the cooling phase is due to its greater speed. In Fig. 45 the occurrence of the first impulse as a function of the driving signal frequency (from 10mHz to 100mHz) and electrical power applied to the microheater (200mW, 250mW and 300mW) is illustrated. The shown data are relative to a fan-shaped microheater; however, analogous results were also obtained for the others designs.
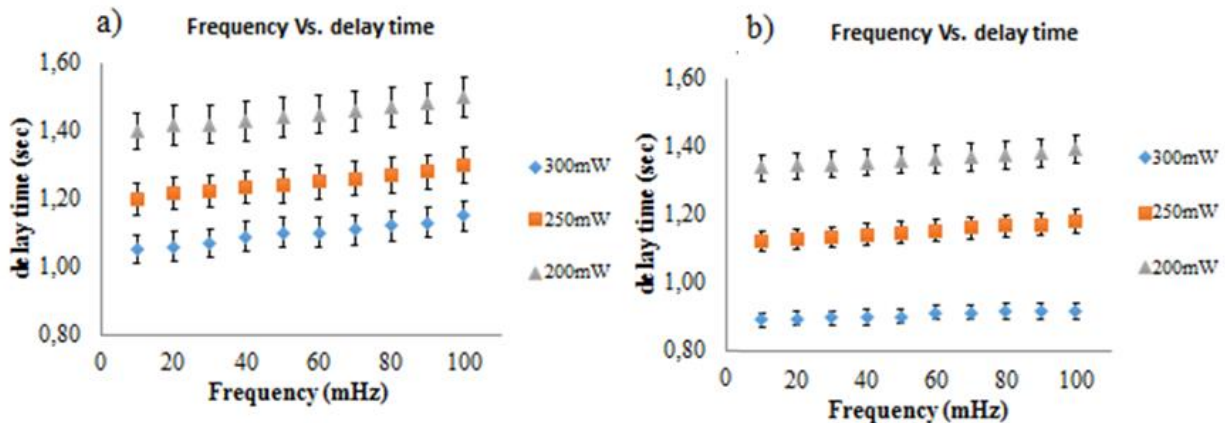

Fig 45: Delay time vs. frequency for different dissipated electrical power during: a) heating condition b) cooling condition.

The delay time for the initial occurrence of the peaks during natural cooling conditions remains more of less the same while in the heating phase a small shift is observed at different frequencies. This shift is related to the heat accumulation induced by the highest frequencies. The delay time in the occurrence of the initial impulse in cooling phase takes lesser time than the heating phase thanks the quicker rate of change in the temperature in cooling condition (see Fig. 33). The investigation demonstrates that the occurrence of the initial PE from the crystal can be governed by controlling electrical power (thus controlling the rate of heating and cooling) applied to microheater.

4.3.4 Temporal distance between electrical peaks

The temporal distance trend between electrical impulses during the whole thermal transient was also analysed. In particular, the occurrence of the impulses tends to decrease during the thermalization of the sample. Since the pyroelectric effect is related to the temperature variations, the temporal distance among the current impulses is very short (i.e. high occurrence of impulses) during the initial phase of the thermal transient, while grows larger when approaching complete thermalization of the sample.
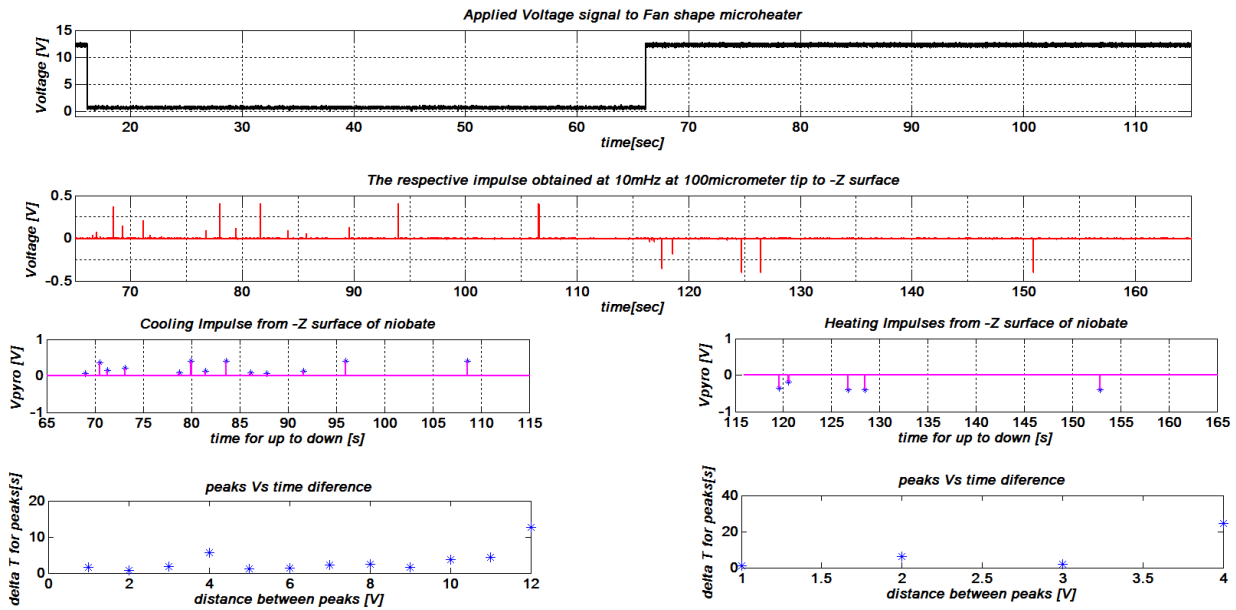
Fig 46: Fan shape Microheater at 100µm tip to –Z surface gap : a) the applied voltage signal, b) respective impulses acquired from oscilloscope, c) (left) impulses data with peaks for cooling, d) (right) impulses data with peaks for heating, e) (left) distance between the peaks vs. the distance between the time for voltage for cooling condition, f) (right) distance between the peaks vs. the distance between the time for voltage signal heating condition.

Fig. 47, shows an exponential increase with time of the distance between the impulses, which is clearly related to the dependency of the rate of heating and cooling of the crystal in a transient condition. The reported data are relative to a fan-shaped microheater, but similar results were observed for the other designs.
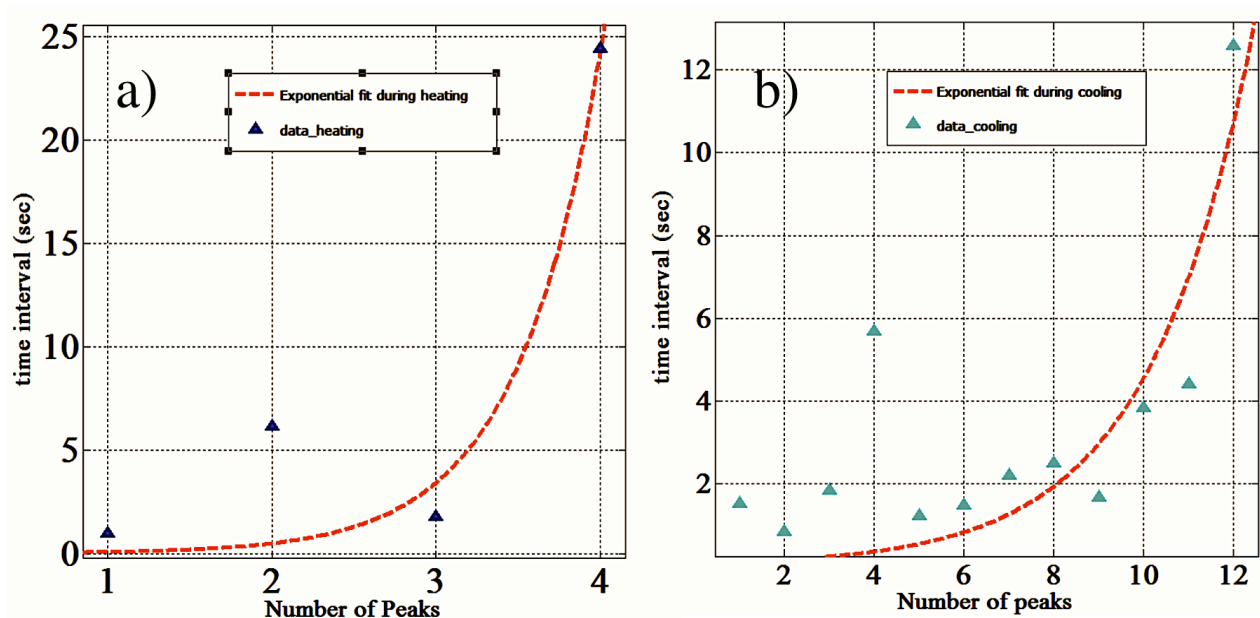

Fig 47. Exponential plot for the impulse occurrence in time during the: a) heating condition, b) cooling condition.

The fitting curve clearly shows the exponential dependence of the occurrence of the electrical impulses (i.e. the pyroelectric effect) on the thermalization of the crystal induced by the μH. Moreover, the steeper slope in the cooling condition of μH confirms that the rate of cooling is faster than the heating condition.

Furthermore pyroelectric investigation activated by the fan microheater was performed under humidity conditions using the same micrometric metallic probe setup. This study will shows the microheater as a heating tools that can used in different ambient conditions in order to generate the pyroelectric effect from LiNbO$_3$ crystal.

4.4   Pyroelectric investigation under humidity conditions

The pyroelectric effect activated by the fan shape microheater is further investigated under humidity conditions using the similar micrometric metallic probe setup inside a Teflon hood. In addition, a resistive Aluminium (Al) Sensor was integrated along the microheater in order to control the temperature variation effect from the microheater. The pyroelectric current impulses is analysed for the fan microheater design and operating conditions (Humidity) demonstrate the effectiveness of the microheater as thermal tool for activating the pyroelectric effect. Fabrication of the resistive thermal sensor was performed using similar photolithography process and metal deposition technique was performed using sputtering. The steps involve in the photolithography and metal deposition can be seen in fig 22[7].
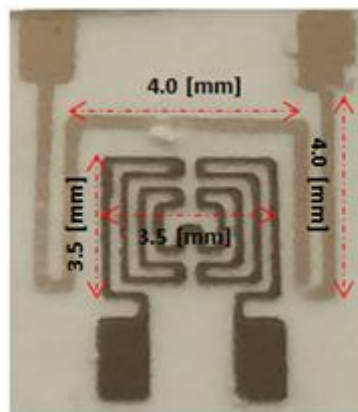

Fig 48: fabricated microheater with aluminium sensor on the +Z surface of LiNbO₃.

Titanium (Ti) of 300nm-thick for heater material and Aluminium (Al) of 200nm was used for the resistive sensor. Titanium and aluminium was deposited using electron beam and sputtering technologies. Finally the pads of the microheater and thermal sensor were wire bonded using silver paste. The measured microheater resistance was 820Ω and the Aluminium sensor was 36.7Ω respectively.
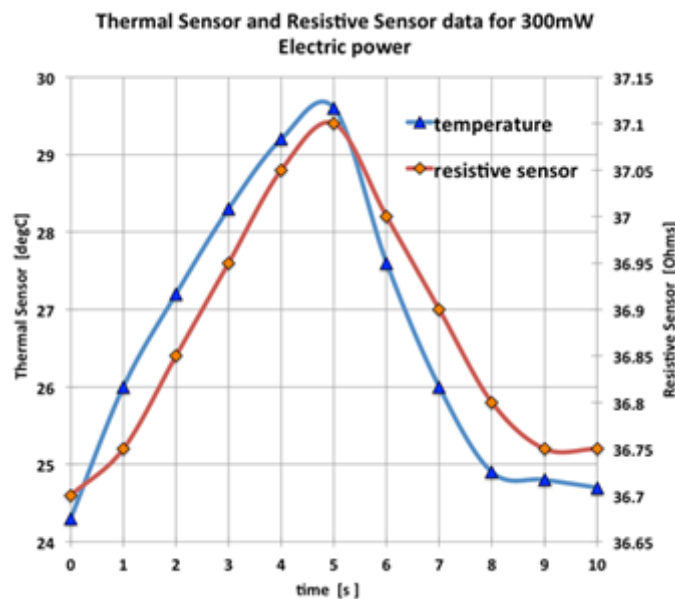
4.4.1   Thermal analysis of the microheater

Thermal analyses of the titanium microheater designs were performed both theoretically and experimentally, using COMSOL ™ Multiphysics package. The integrated aluminium resistive sensor was neglected, while performing the theoretical simulation using COMSOL multiphysics. The thermal sensor was bonded on the -Z surface in the centre of the area heated by microheater where the temperature variation is higher using a silver paste. The obtained temperature on both the thermos couple and the respective change of the resistance of the integrated resistive sensor with respect to the electric power applied on the microheater is shown in fig 49.
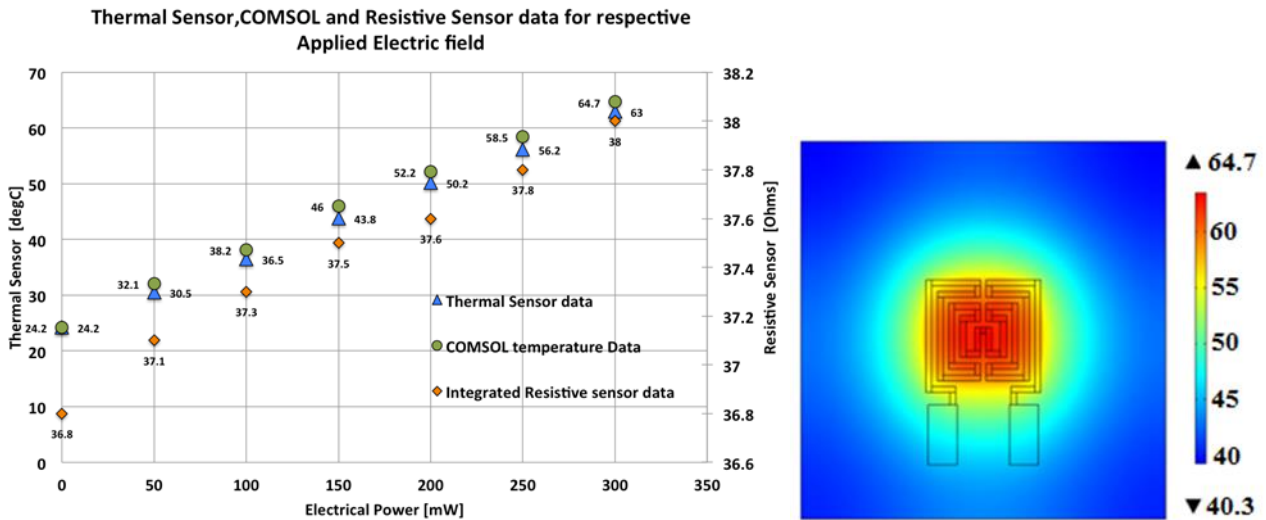
***Fig 49: a) Temperature and resistance measurement from thermo couple sensor, COMSOL &
resistive sensor at different applied electric power to microheater, b) COMSOL thermal Map of Fan
Shape Microheater at 300mW applied electrical power.***

Furthermore, the transient investigation is also further analysed by applying a step voltage in order to dissipate an electrical power of 300mW for 10 s with 50 % duty cycle using a voltage generator. In figure 50, the thermal sensor plot with the respective aluminium resistive sensor data in the transient regime for the heater on and heater off time for 5 s each is shown.


***Fig 50: Transient measurement of the thermal and resistive sensor on application of 300mW electric
power.***

Hence it can be understand that by knowing the resistance of the integrated aluminium sensor the temperature of the microheater achieved can be estimated. For instance, the temperature attained by the microheater at 28^0C, shows an resistance of 37.1 Ohms in the aluminium sensor.

4.4.2   Pyroelectric analysis under humid condition

The pyroelectric effect from –Z surface of LiNbO₃ activated by the fan shape microheater was further investigated analysing the pyroelectrical current impulses detected using a beryllium micrometric probe connected to an oscilloscope as discussed before. The micrometric metallic probe was positioned at 100µm gap from the –Z surface of crystal using a micromanipulator. The setup was placed inside a closed Teflon case for investigating pyroelectric effect under humid condition. The schematic of the closed case setup is shown in fig 51. The initial humidity of the closed system was measured around 54% using a RH318 (testo 525) Humidity sensor.
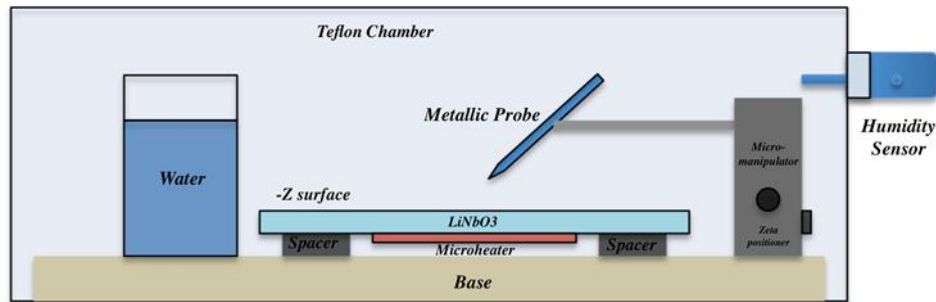
*Fig 51: Schematic of the humidity measurement setup.*

A periodic square waveform with a frequency of 100mHz, and a voltage adjusted to dissipate an electrical power of 300mW was applied to the microheater. The micrometric metallic probe was positioned at 100µm from the –Z surface of LiNbO₃ crystal for obtaining the current impulses. When the temperature of the crystal increase, the decrease in the spontaneous polarization occurs and results in the net deficits of compensating negative charges on the –Z surface of crystal. Thus, negative current impulses can be observed at the oscilloscope and vice-versa. The surface bounds charges play an important role in generating the current peaks on the oscilloscope. These bound charges response to the motion of charge particles in the air dielectric film between crystal surface and metallic probe. Controlling the humidity of the surrounding can regulate the motion of charge particles in the air. In order to reduce the humidity of the closed system 150gms of bay salt was placed in a container and inserted in the closed Teflon case system. The humidity was reduced from 54% to 42%.
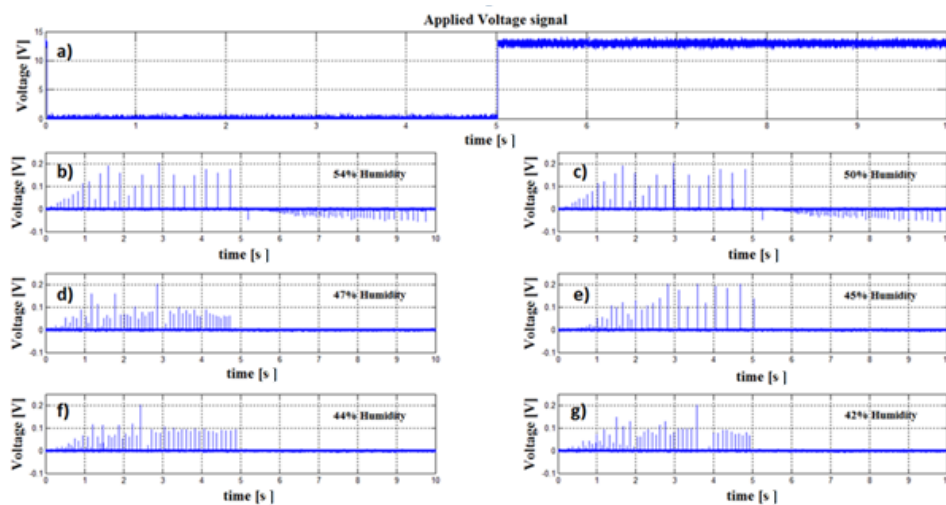
Fig 52: Current peaks obtained on oscilloscope using metallic probe: a) Voltage signal applied to microheater to dissipate electrical power of 300mW, b) 54% Humidity, c) 50% Humidity, d) 47% Humidity, e) 45% Humidity, f) 44% Humidity and g) 42% Humidity.

57

The humidity of the system decreases thus the density of air increase resulting in the reduction of the air resistance against the motion of particles making the dielectric of air less conductive inside the closed case. Thus the electric field required for the dielectric breakdown of air to produce the current peaks increases (see fig 52). This results in the obtaining lower current peaks on the oscilloscope during heating, while during the cooling a faster rate of change in temperature dominating the humidity effect resulting in more number but with lower amplitude of voltage peaks compare to heating.

It is also observed that as the humidity of the system decrease thus the density of air increase resulting in the reduction of the air resistance against the motion of particles making the dielectric of air less conductive inside the closed case. Thus the electric field required for the dielectric breakdown of air to produce the current peaks increases. This results in the obtaining lower current peaks on the oscilloscope during heating, while during the cooling a faster rate of change in temperature dominating the humidity effect resulting in more number but with lower amplitude of voltage peaks compare to heating. After attaining the system humidity of 42%, the container with the salt was replace by a container of hot water 95^0C. The current peaks were obtained on the oscilloscope from 42% to 74% (see fig 53).
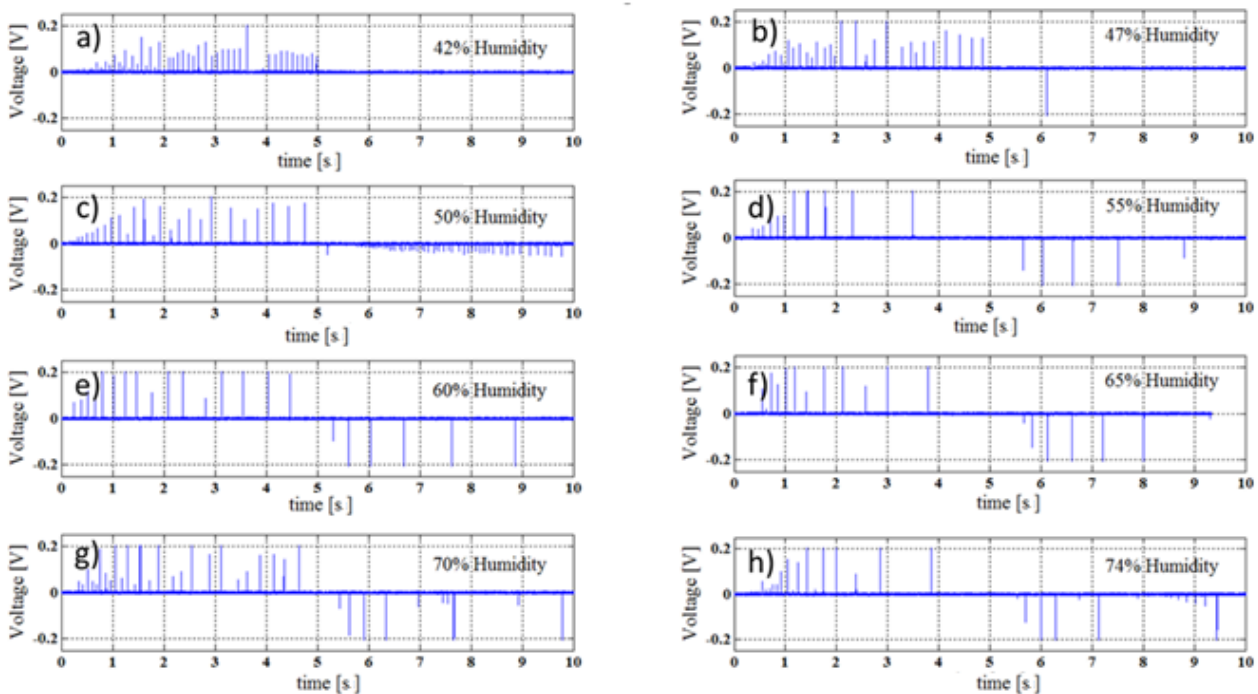
Fig 53: Current peaks obtained on oscilloscope using metallic probe: a) 42%, b) 47%, c) 50%, d) 55%, e) 60%, f) 65%, g) 70% and h) 74% Humidity.

As the humidity inside the case slowly increases the air density decrease gradually, hence the air particles are sparsely placed this means low moment of air drag due to increases in water particle making the air dielectric film more conductive. Hence the electric field require for the dielectric breakdown of air decreases resulting in the increase of current peaks with a higher voltage amplitude during the complete thermalization process.

Reference:

[1] Darhuber, J. P. Valentino, S. M. Troian and S. wager, (2003). Thermocapillary actuation of droplets on chemically patterned surfaces by programmable Micro-Heater arrays. *Journal of Microelectromechanical systems,* vol. 12, p. 6.

[2] Shur, D., and Rosenman, G., (1996). Figures of merit for ferroelectric electron emission cathodes, *Journal of Applied Physics*, **80**(6), 3445.

[3] Rosenman, G., Shur, D., Krasik, Y., and Dunaevsky, A. (2000). Electron emission from ferroelectrics. *Journal of Applied physics , 88*, 6109.

[4] Shur, D., and Rosenman, G., (1996). Figures of merit for ferroelectric electron emission cathodes, *Journal of Applied Physics*, **80**(6), 3445.

[5] Kim, D.-W., Bourim, E.M., Jeong, S.-H., and Yoo, I.K., (2004). Pyroelectric electron emission and domain inversion of LiNbO3 single cystal, *Physica B,* vol. 352, pp. 200-205.

[6] Bourim, E.M., Moon, C.-W., Lee, S.-W., Sidorkin, V., and Yoo, I.K., (2006). Pyroeletric electron emission from -Z surface polar surface of Lithium nionbate monodomain single crystal, *J Electroceram,* vol. 17, pp. 479-485.

[7] Bhowmick, S., Iodice, M., Gioffrè, M., Breglio, G., Riccio, M., Irace, A., Romano, G., Coppola, G. (2015). "Pyro-Electro-Thermal analysis of LiNbO₃ using microheaters" *Fotonica AEIT Italian Conference on Photonics Technologies, 2015*, Turin, 2015, pp. 1-5. doi: 10.1049/cp.2015.0129.

Chapter 5
Applications

## 5.1 Microheater for dispensing Nano-Pico droplets by pyroelectrodynamic shooting.
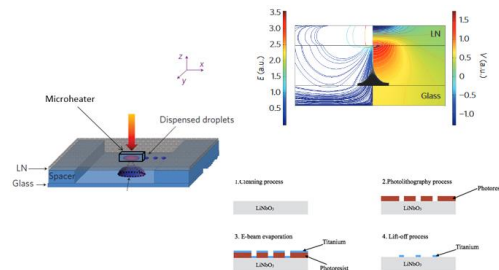
This work was performed in collaboration with ISASI (Institute of applied sciences and intelligent systems) and IMM (Institute of microelectronics and microsystems)-CNR.

5.1.1 Introduction

The wetting properties of hydrophobic surfaces using electric fields (known as electro jetting) or displacing liquid droplets using heat gradients (thermocapillarity) are useful processes in microfluidic and optofluidic systems for adapting the shape of liquid menisci and patterning liquids or forming and displacing droplets [1-5]. Different dispensing methods have been developed in recent years [6-8]. Recently, a new concept of electro hydrodynamic-based droplet generation called pyroelectrohydrodynamic shooting, for direct drawing and dispensing of droplets with volumes on the scale of attoliters from liquid drops or film reservoirs [9]. This technique does not require electrodes, high voltage circuit's connections or special capillary nozzles. The electric fields are generated pyroelectrically using functionalized substrates of lithium niobate ($LiNbO_3$). In this approach, they used the pyroelectric effect to transfer liquids between two substrates and manipulate the droplets 3 dimensionally. Although, the simplicity of the technique suggests potential and dispensing daughter droplets, fragmentation microlitere drops and liquid printing, but limited to achieve the lab-on chip device requirements. This is due to the macroscopic thermal stimulus tool used for the dispensing process such as: laser, hot plate. Here, we present a novel technique to achieve the pyroelectrohydrodynamic (PED) shooting process with the advantage of lab on chip process using microheater fabricated on the $LiNbO_3$ for the drawing and dispensing of droplets. We expect this technique will open a new window for the lab on chip process in biochemistry and nano-printing.

5.1.2 Microheater design and setup

The setup, consists of two plates and fabricated fan shape microheater acting as a heat source (See fig 54).
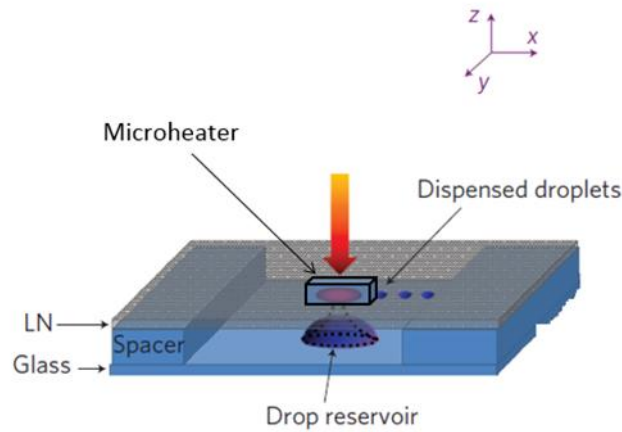
Fig 54: Schematic of the dispenser system consisting of two plates and a microheater source.

A microscope glass slide forms the base of the liquid reservoir (which could be a drop or a film), and the LiNbO$_3$ crystal wafer (z-cut, optically polished and 500 µm thick) acts as an auxiliary plate that drives the process and acts as a substrate for the dispensed liquids. The fan shape microheater is fabricated on the +Z surface of the LiNbO$_3$ using the fabrication technology mentioned in section 2.3. The output of the realized microheater with the respective dimensions is shown below in the fig 55.
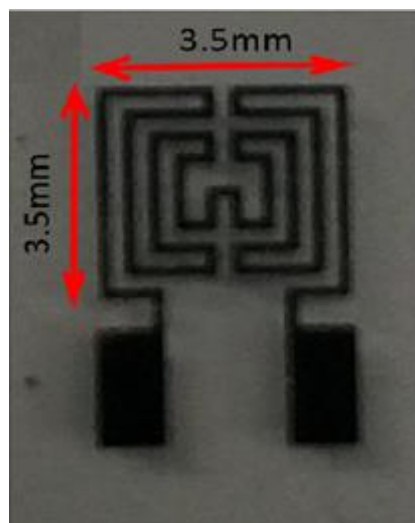

Fig 55: camera image of the final obtained fan shape microheater.

A voltage is applied (to attain an electrical power of 300mW) to the microheater in order to induce the pyroelectric effect locally. The base was a conventional 1mm- thick microscope glass slide. Thin spacer were glued on the edge of the base to super impose the LiNbO$_3$ plate at a fixed distance of ~1mm. An OIR 906 12i was spin coated at 4000 rpm for 60 s using spin coater on a cover glass, inserted in between, at a distance of 1mm from the LiNbO$_3$ crystal, that acted as the substrate on which the droplet were dispensed. Oil Drops of few microliter in volume were deposited on the glass using appropriate electronic syringe.

The measurement setup consist of CMOS camera. This camera was able to capture 125 frames s^{-1} with a resolution of 1240 ×1240 pixel^2 and a pixel area of 12×12 µm^2 respectively. The following setup experiment was performed at ISASI Pozzuoli.

5.1.3   Working principle of dispenser

At equilibrium, the spontaneous polarization P_s of the LiNbO$_3$ crystal is fully compensated by the external screening charges and no electrical field exists [see equation 3(a)]. According to the pyroelectric effect, the temperature change ΔT causes a variation ΔP_s, which builds up an electric potential across the z surfaces. Neglecting the losses, a surface charge density $\sigma = P_c \Delta T$ appears locally when the microheater heats the crystal, where P_c is the pyroelectric coefficient (P_c= -8.3×10^{-5} Cm^{-2} ^{0}C^{-1} for LiNbO$_3$ @ 25^{0}C). The electric field exerts an attractive force on the liquid (see fig 56) and when sufficiently strong, deforms the liquid into a conical tip form which thin liquid jets are released. Such liquid tip is similar to the Taylor cone, but differs because the liquid is not conductive [11-13].
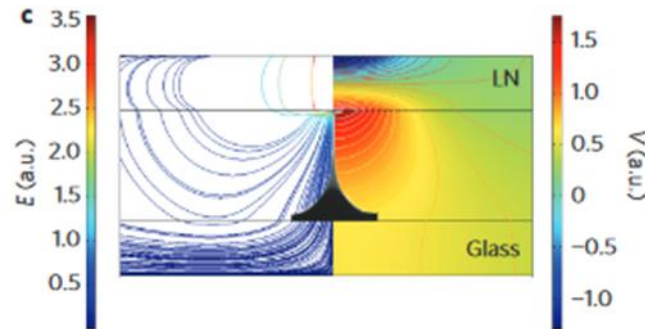

Fig 56: 3D axially symmetric plot of the electric field lines and electric potential obtained using finite element method [9].

It is well known that for a fixed drop volume, a critical value D_C can be defined for the distance D between the base and the substrate, according to the following expressing [14]:

$$D_c = (1 + {}^\theta/_4)V^{1/3} \text{ ...... (36)}$$

Where θ is the contact angle and V is the volume of the drop reservoir. A stable liquid bridge established when D< D_c (see fig 57 a). The most relevant case here refers to D> D_c, when a stable liquid bridge cannot be established between the plates, and a liquid streaming regime occur (Fig 57 b,c).
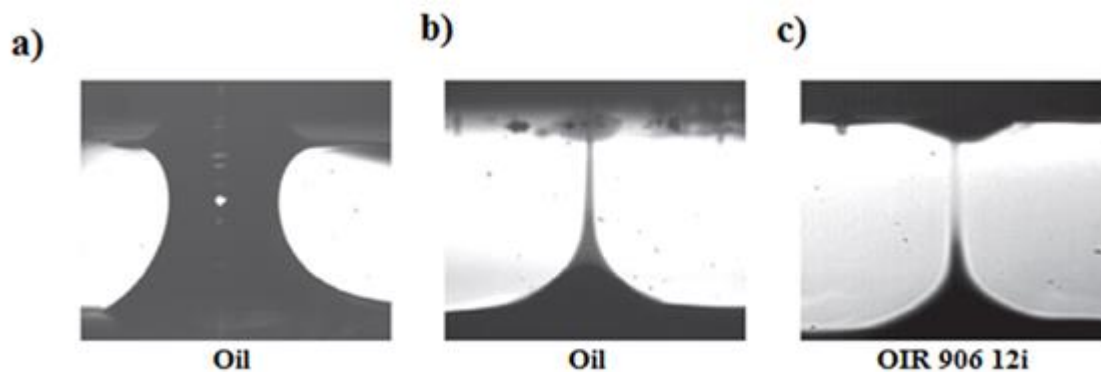
Fig 57: a) Liquid bridge obtained when D is small than the critical distance, equation (36), b,c, shooting of oil and OIR 906 12i.

We use such instability to break up the liquid reservoir and to dispense droplets. Figure 58, shows sequence of liquid shooting in which Nano litre and picoliter OIR 906 12i droplets were dispensed from a liquid OIR film and sessile oil drop reservoir stimulated by the microheater (electrical power= 300mW,) respectively.
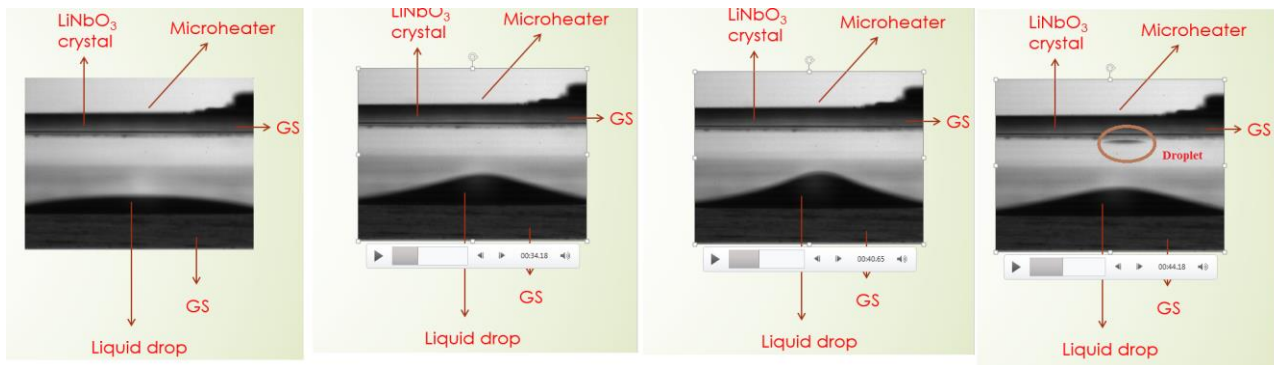
Fig 58: Sequence of OIR 906 12i droplet shots stimulated by microheater.

The phenomenon were captured by a CMOS-camera. The dynamic evolutions shows that the reservoir first deforms into a conical shape, with a height that increase under PED force, and then behaves as 'dispensing gun' that blasts the droplets periodically until the electric field vanishes. It is important to note that electrohydrodynamic-based liquid emissions have been deeply investigated theoretically for wide variety of configurations (liquids flowing in capillary tubes or nozzles, tip streaming from liquid films, steady cone jets, co-flowing liquids and so on. Moreover, the value of the electric field obtained in pyroelectrohydrodynamic for ΔT of 75^0C (~ 10kV) is comparable to the values (900V to 24kV) usually adopted in electrohydrodynamic experiments for inkjet printing [11,15].

5.2   Microheater array for microneedles formations.
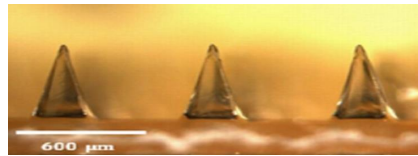
This work was performed in collaboration with ISASI (Institute of applied sciences and intelligent systems) and IMM (Institute of microelectronics and microsystems)-CNR and IIT (Italian Institute of Technology).

5.2.1   Introduction

An innovative microheater array design is realized on a lithium niobate crystal, to induce a uniform pyroelectric effect on a larger area of 1.25×1.25 cm^2. Thermal analyses of the device were performed both experimentally and theoretically using aforementioned technologies (i.e. FLIR thermocamera and COMSOL^{TM} multiphysics). A series of preliminary numerical simulations were investigated to obtain the optimized design of aforementioned specifications. The microheaters is fabricated on the +Z surface of lithium niobate crystal using photolithography process followed by titanium thin film deposition. We performed on this device a series of electro-thermal characterizations; the results of the measurements showed a good agreement with the theoretical model in terms of temperature distribution, making a comparison between the thermal maps coming from the two methodologies. A particular biomedical application, focus on the electro-hydrodynamic fabrication of biodegradable microneedles. Microneedles have been successfully generated using an array (3×1) of S-shape microheaters fabricated on pyroelectric crystal LiNbO$_3$ at IMM-CNR (see Figure 59). Further works are being performed in order to produce an array of 10×10 micro-needles in an area of 1.25×1.25 cm^2 by taking the advantage of our optimized device reported in this work.
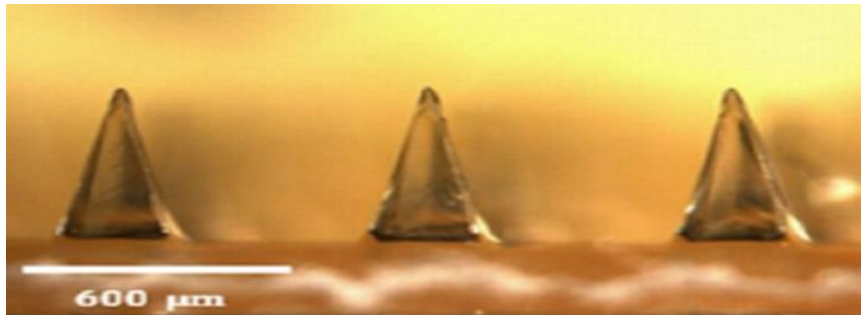
Fig 59: Biodegradable microneedles.

We simulated the behaviour of the design optimizing its geometry using 3D Finite Analysis (FEA). Though the preliminary simulations were investigated on a couple microheaters, then we examined some parameters of influence, and, as a result of our simulations, we got an optimized design of the entire array geometry. Further work involves in fabrication of the device, which geometry has been defined, taking into account the results of the numerical simulations previously performed. The microheater was fabricated by photolithography pattering on the $LiNbO_3$ crystal, followed by the titanium thin film evaporation technique.

5.2.2   Design of microheater

The simulations is performed by coupling the power generation, due to the joule heating with the heat conduction and dissipation into the device considering also the heat exchange with the surrounding air. Similar multiphysics nodes with boundary conditions (including the material properties) are used in simulating the array structure (see chapter 2.2).

Initially, a simple principle was take into consideration by coupling two S shape microheaters without having the loss of uniformity in the temperature distribution. It was observed that the central area in-between the microheaters shows a uniform temperature distribution. In consideration of the above-obtained result various designs were adapted, increasing the number of micro-heaters and improving in each step the thermal profile along optimization. The designs take into considerations with the respective thermal profile along A' (along x-axis) is shown below in the sequential manner in order to achieve a uniform temperature distribution profile in an area of 1.25×1.25 cm^2 (see Figure 60).
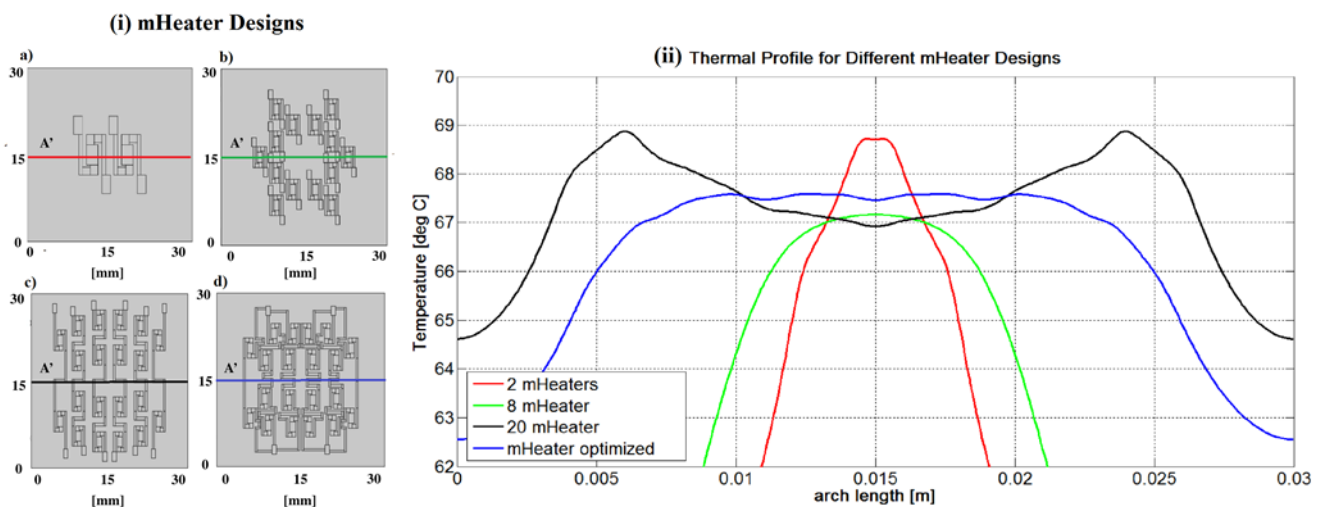
Fig 60: (i) microheater designs a) 2microheater, b) 8microheater, c) 20microheater, d) 20mod microheater; 2(ii). Thermal profile along A' for the respective microheaters.

5.2.3 Fabrication

Fabrication of the device was performed using the clean room technology at IMM-CNR. The fabrication process flow was used as mentioned in section 2.3. The realized device can be seen in fig 61.
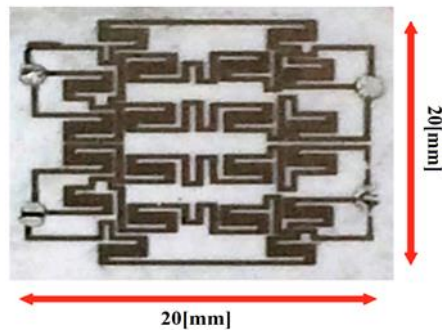
*Figure 61: Final obtained microheater.*

Finally, the pads of the microheater were wire bonded using silver paste. In table XV both the simulated and measured resistance for the realized microheater is reported showing a good agreement between the data.

Design	Simulated resistance [Ω] Top/ Bottom microheater	Measured Resistance [Ω] Top/Bottom microheater
Array	99.6 / 99.6	98.7/ 102.2

Table XV: Value of the total simulated and obtained fabricated microheater resistance.

5.2.4 Thermal analysis of microheater

Thermal measurements on titanium microheaters were performed using FLIR SC7000 series thermos-camera (appendix A.2). The compared thermal maps and the relative profiles along the lines A', A, A'' from the –Z surface of LiNbO3 are reported in Figure 62 respectively.
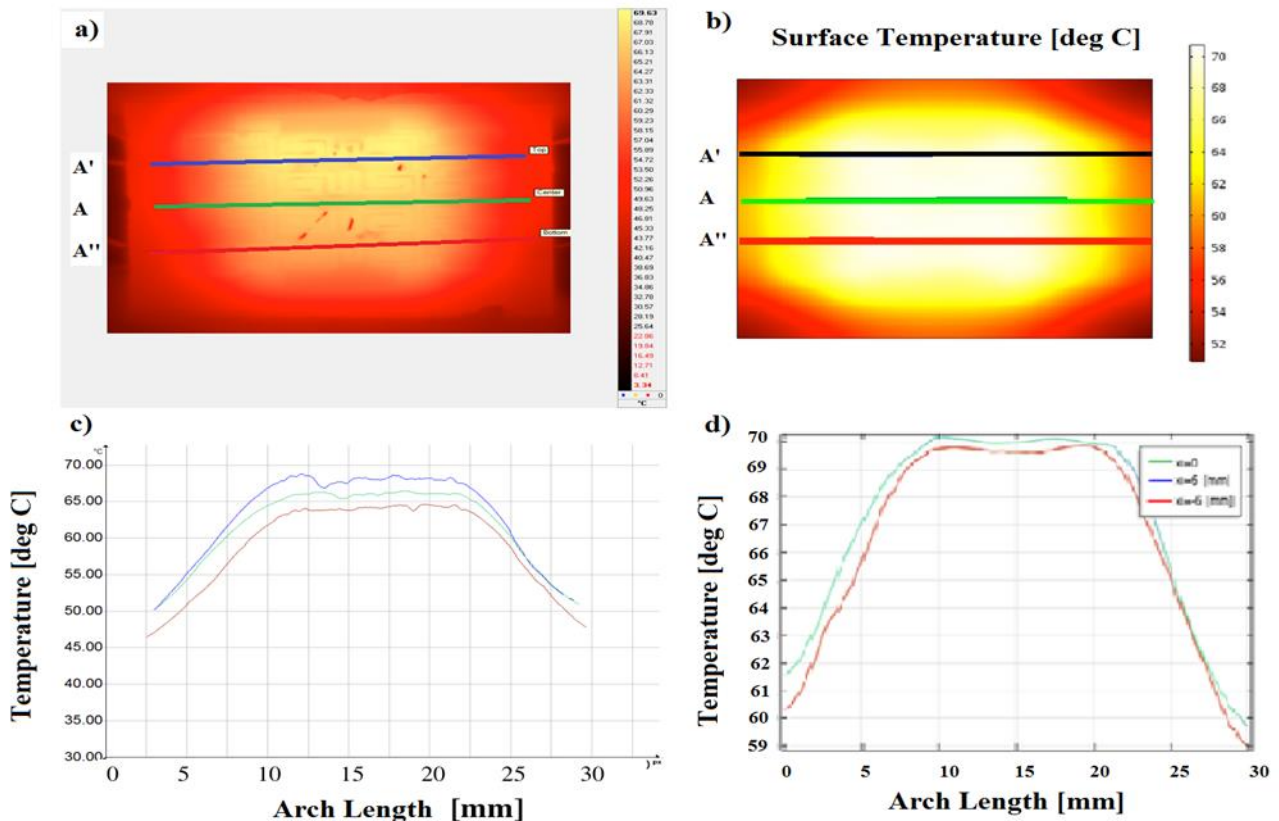
Figure 62: Thermal maps a) FLIR thermo camera, b) COMSOL^{TM} simulation, thermal profile along A' A A'' c) experimentally d) theoretical model.

Analysing thermal profiles along A', A, A'' from figure 62a & 62b, shows a good agreement between the experimental profile with respect to the simulated ones. Nonetheless, it is also shown that the temperature is uniform in an area 1.25×1.25 cm²., with a minimum temperature difference of 0.5 °C between the 3 profile lines A' A A''. Thermal profiles were also obtained along the y directions see figure 63.
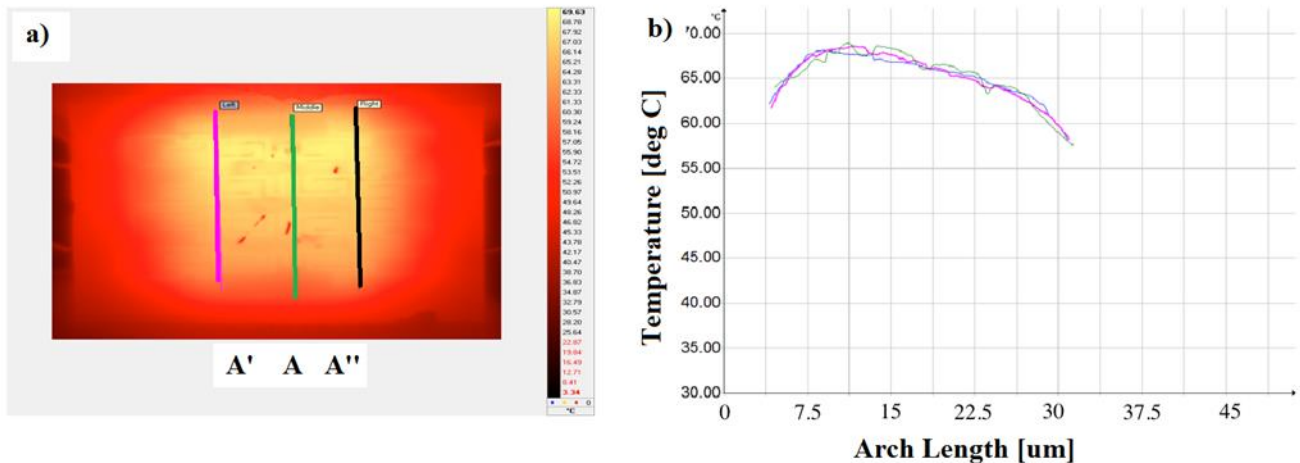

Figure 63: a) Thermal maps obtained using thermo camera, b) thermal profile along A' A A''.

The thermal profile along the y direction at 3 different profiles lines A' A A'' shows a difference of 4^{0}C in the thermal gradient along the profile lines. This effect could be explained considering the facts that two different parts formed the microheaters with a small difference in the resistance value see table XV, and/or thickness variation during deposition. Applying the same voltage for the microheaters results in different distributed electrical power along the top/bottom microheater. This result in different thermal powers due to joules heating effect, henceforth the change in temperature along the y direction.

In future work, the design must be tested for producing the 10×10 microneedles using the pyroelectric effect induce by lithium niobate using integrated by the microheater mentioned above.

5.3   Microscale Spiral formation by pyro-electrospinning using microheater for biocompatible polymers in life science applications.
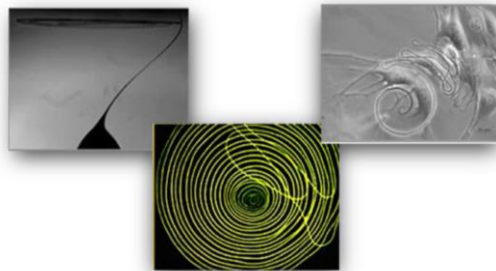
This work was performed in collaboration with ISASI (Institute of applied sciences and intelligent systems) and IMM (Institute of microelectronics and microsystems)-CNR.

Spiral patterns are found extensively in nature as well as in art. Even some technological devices are inspired to and take advantage of this kind of shape. Spiral moulds have been used for characterizing the rheological behaviour of polymers injected over fabrics [16]. Very recently, microscale soft-robots have been developed with spiral bending capabilities [17], spiral-like electrodes have been proposed for energy harvesting applications [18], and three-dimensional spirals have been suggested for developing new ways of manipulating the polarization state of the THz electromagnetic waves [19]. Here, we present the μ-pyro-electrospinning (μ-PES), an innovative approach where polymer fibres are electro spun (ES) by pyroelectric fields controlled at microscale and assemble directly into spiral patterns with true regularity at microscale. A mask-free and single step process al-lows one to fabricate spiral templates for different applications, including cell patterning.

The μ-PES, instead, is an innovative configuration where the operation conditions enable to keep the bending behaviour regular for producing true spirals at microscale. In particular, as a new modified version of ES, it is able to sustain the intrinsic tendency of ES at producing spiral envelops avoiding the noise coming from the chaotic whipping, as shown in Fig 64:
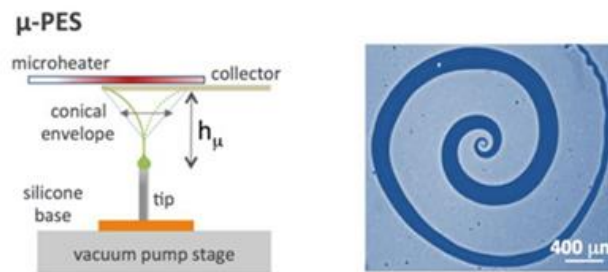

Fig 64: μ-PES with visualization of the superposition of the m-PES spiral (grey) over a golden spiral produced geometrically. The distance h_μ is in the range of millimetres [20].

The μ-PES is able to condition the driving electric field into a distribution able to favour the tendency of the fibre in spinning spirally. Spiral structures are obtained by an easy and versatile approach based on a single step process, thus avoiding repetitive, time consuming and expensive lithographic procedures, or direct printing by mechanical scanning.

5.3.1 The μ-PES setup

The μ-PES setup and the relative measurements were performed at ISASI. The μ-PES set up configuration presents two key differences compared to the first developed PES reported in [21]. Figure 64 a shows the schematic view of the μ-PES set-up .Here the polymer drop (0.5μL) is deposited onto a metal tip positioned vertically and the pyroelectric effect is regulated by a microheater integrated directly onto the surface of the $LiNbO_3$ crystal (LN-Crystal Technology Inc. in the form of z-cut wafers 500 μm thick and both sides polished with a surface quality of 40/20). A standard optical path with a high-speed CMOS camera (Motion Pro Y3-S1, pixel size 10.85 × 10.85 μm), allowed us to have a side view of the spinning process, while a traditional voltage generator drove the μH in order to have constant power dissipation (see fig 65 c). The collector was a glass coverslip mounted onto a conventional x-y translation stage (PI, Mercury C-863DC motor controller) that was stationary during the deposition of a single spiral and was moved when printing serial spirals (see fig 65 b). The collector was positioned between the base tip and the driving crystal at a typical distance ranging between around 80 μm and 1.4 mm, depending on the operation conditions.
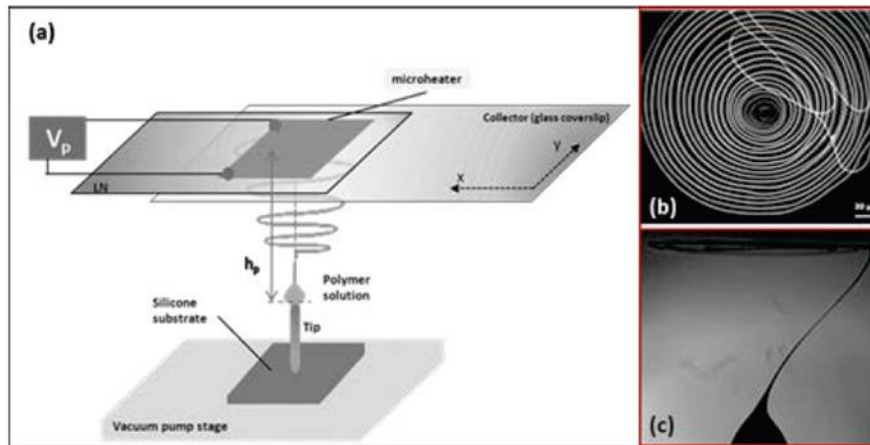
Figure 65: (a) μ-PES set-up, (b) Optical Microscope image of a PMMA 9% micro-scale, (c) A slide view of the μ-PES process [20].

5.3.2   Thermal analysis

The microheater is made of a 300 nm Titanium (Ti) thin film. This material was chosen because a thin layer of oxide on its surface prevents the corrosion in various conditions. The fabrication process is describe in section 2.3. This microheater was supplied by an external power supply (THURLBY THANDAR INSTRUMENTS, 32 V; 2 A). The power limit was 350 mW and the microheater can be used indefinitely when respecting these limits, thus avoiding detrimental thermal shocks for the crystal.
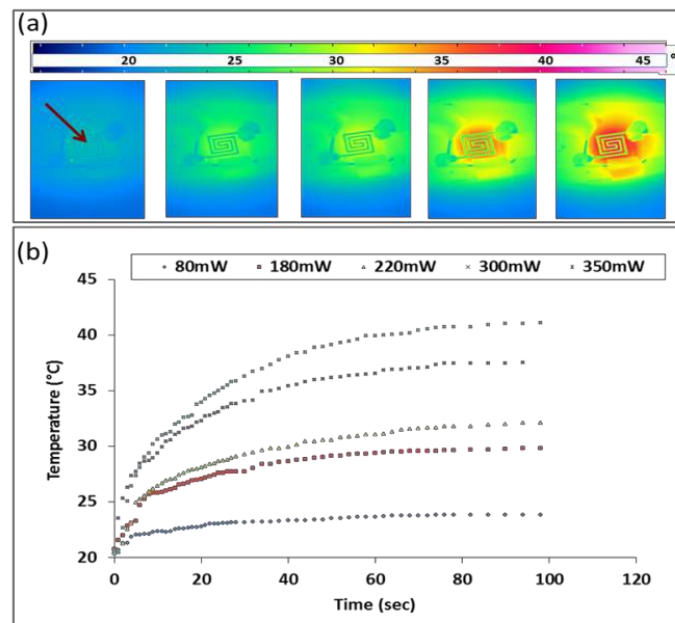

Figure 66: (a) Typical thermal camera images of the crystal during m-heating (the temperature increases from left to right); (b) corresponding temporal evolution of the crystal temperature for different operation powers in correspondence of the region evidenced by the red arrow in (a) [20].

Fig.66 (a) presents the temporal evolution of the temperature values since the microheater, our driving force, and switch on-off of the microheater at different operation powers. The experimental results show clearly that the crystal temperature rose gradually till a sort of plateau for each power value, in correspondence

of which the temperature variation is negligible (the maximum power used 350 mW corresponds to a maximum temperature measured on the crystal surface of 40°C). As this plateau is reached, according to the pyro-electric effect, being the temperature variation null, no pyro-electric field exists and the already drawn fibre stops spinning.

### 5.3.3   Sample testing using μ-PES set-up

PMMA is used here for demonstrating the reliability of the technique for different reasons, including its widespread use and the wide range of available solvents and concentrations. Poly (methyl methacrylate) (PMMA) (9011-14-7, Average molecular weight Mw ≈ 996,000 - Sigma Aldrich) was dissolved in anisole (η= 1 cP, εr = 3.6, Microchem Corp., Newton, MA) at different concentrations (2-15 wt %) and stirred at 50°C for 1 hour.
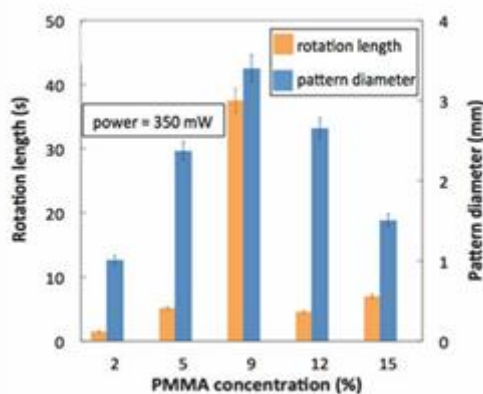
Fig66: rotation length and pattern diameter for each concentration at a fixed power of 350 mW. Mean values were evaluated over ten replicates of the experiments [20].

Furthermore, the role of polymer in μ-PES was investigated. Since the viscosity of the polymer is well known to influence the dynamics of ES, solutions of PMMA were pre-pared   in anisole with different concentrations for characterizing   the operation conditions. The results show that the polymer concentration plays a key role in producing reliable and long spirals. In particular, Fig63a gives information about the "rotation length" and the "pattern diameter" for each sample, namely the average value of the duration of the fibre revolution and of the diameter of the spiral pattern, respectively. The power and the distance tip-collector were fixed at 350 mW and 900 μm, respectively, in order to get a rotating fibre for each concentration value. These results show that PMMA @ 9%, among the others, holds the record in terms of longer spirals and wider resulting pattern, thus exhibiting its best attitude to generate long and regular spirals.

Finally, being the possibility to modulate both the cell orientation and the cell shape onto well-defined and multiscale geometries of great interest for investigating the cell functions and morphogenesis induced by cell micro patterning [21], the self-sustained spiral templates obtained were used as patterns for controlling the morphology of live cells at microscale along regular spiral shapes (Fig.66)
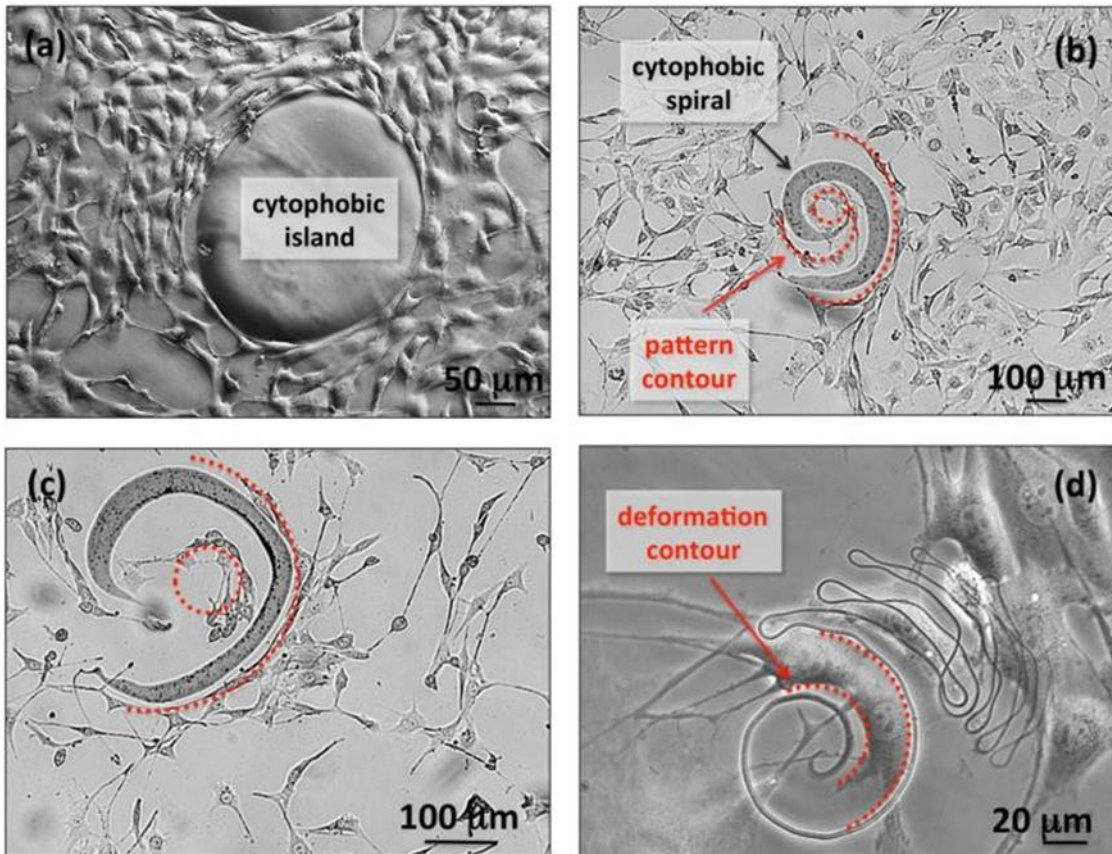
Fig 66: Optical microscope images of different PMMA patterns deposited onto a conventional glass slide and plated with the NIH-3T3 cells: (a) spot deposited by a pipette showing the cytophobic nature of PMMA; (b,c,d) spiral patterns with decreasing thickness of the fibre[20].

In summary, we developed here the μ-PES, an innovative approach belonging to the ES family, able to generate true spiral patterns at microscale, by a direct process that is mask-free and single step. The peculiarity of μ-PES configuration is its ability to keep under control those fiber bending effects that, instead, occurs chaotically in traditional ES. The results show how longer spirals can be obtained by controlling operation parameters that belong to polymer concentration and to EHD forces. These self-sustained structures are demonstrated to be useful for investigating the response of live cells to intriguing multiscale spiral shapes, thus opening the route to a potential new platform for cell morphogenesis studies and for cochlea regeneration scaffolds.

Reference:

[1] Mugele, F. & Baret, J.-C. Electrowetting: from basics to applications. J. Phys. Condens. Matter 17, R705–R774 (2005).

[2] Jiao, Z., Huang, X., Nguyen, N.-T. & Abgrall, P. Thermocapillary actuation of droplet in a planar microchannel.
Microfluid. Nanofluid.5,205–214 (2008).

[3] Squires, T. M. & Quake, S. R. Microfluidics: fluid physics at the nanoliter scale. Rev. Mod. Phys. 77, 977–1026 (2005).

[4] Gallardo, B. S. et al . Electrochemical principles for active control of liquids on submillimeter scales.Science 283, 57–60 (1999).

[5] Kataoka, D. E. & Troian, S. M. Patterning liquid flow on the microscopic scale.Nature402,794–797 (1999).

[6] Casner, A. & Delville, J.-P. Laser-induced hydrodynamic instability of fluid interfaces.Phys. Rev. Lett.90,144503 (2003).

[7] de Heij, B.et al. Highly parallel dispensing of chemical and biological reagents.Anal Bioanal Chem.378,119–122 (2004).

[8] Ondarcuhu, T. et al. Controlled deposition of nanodroplets on a surface by liquid nanodispensing: application to the study of the evaporation of femtoliter sessiledroplets.Eur. Phys. J. Special Topics 166,15–20 (2009)

[9] Ferrarp,P. Coppola, S., Grilli, S., Patruzo, M., Vespini, V., (2010), "Dispensing nano-pico droplets and liquid pattering by pyroelectrodynamic shooting", nature technology, 5: 429-435

[10] Rosenblum, B., Bräunlich, P. & Carrico, J. P. Thermally stimulated field emissionfrom pyroelectric LiNbO3Appl. Phys. Lett.25,17–19 (1974).

[11] Ahmed, R. & Jones, T. B. Optimized liquid DEP droplet dispensing. J. Micromech. Microeng.17,1052–1058 (2007).

[12] de Heij, B.et al. Highly parallel dispensing of chemical and biological reagents.Anal Bioanal Chem.378,119–122 (2004).

[13] Park, J. U.et al. High-resolution electrohydrodynamic jet printing.NatureMater.6,781–789 (2007).

[14] Maeda, N., Israelachvili, J. N. & Kohonen, M. M. Evaporation and instabilities of microscopic capillary bridges.Proc. Natl Acad. Sci. USA100,803–808 (2003).

[15] Whitesides, G. M. The origins and the future of microfluidics. Nature 442,368–373 (2006).

[16] A. Martinez, J. Castany, D. Mercado, " Characterization of viscous response of a polymer during fabric IMD injection process by means a spiral mold.", Measurement 44, 1806–1818, (2011)

[17] J. Paek, I. Cho, J. Kim, "Microrobotic tentacles with spiral bending capability based on shape-engineered elastomeric microtubes.", Sci. Rep. 5,10768-10, (2015)

[18] L. Chen, H. Guo, X. Xia, G. Liu, H. Shi, M. Wamg, Y. Xi, C. Hu, "Novel Spiral-Like Electrode Structure Design for Realization of Two Modes of Energy Harvesting", ACS Appl. Mater. Interf. , 7, 16450-7, (2015)

[19] T. Kan, A. Isozaki, N. Kanda, N. Nemoto, K. Konishi, H. Takahashi, M.Kuwata-Gonokami, K. Matsumoto, I. Shimoyama, "Enantiometric switching of chiral metamaterial for terahertz polarization modulation empolying vertically deformable MEMS spirals." Nat. Comm. , 6, 8422-7, (2015)

[20] L. mecozzi, O.gennari, R. Rega, S. grilli, S. Bhowmick, M.A.Gioffre, G. Coppola, P.Ferraro, "Spiral formation at microscale by micro-pyro-electrospinning", (2016), AIP conference proceedings, 1736(020079), DOI: 10.1063/1.4949654.

[21] S. Coppola, V. Vespini, G. Nasti, O. Gennari, S. Grilli, M. Ventre, M. Iannone, P.A. Netti, P. Ferraro, "Tethered Pyro-Electrohydrodynamic Spinning for Patterning Well-Ordered Structures at Micro- and Nanoscale", *Chem. Mater.* **, 26,** 3357–3360, (2014).

Chapter 6
Conclusion

We presented a deep investigation of the pyroelectric effect induced into ferroelectric LN by micro-heater structures integrated directly onto the surface of the crystals. Four Microheater namely: Meander, Spiral, Fan and S shape configurations were considered in order to fully understand the distribution of the electric field under different stimulation conditions. Realization of the microheaters on LN crystal gives an advantage of confined temperature gradient and with low electrical power consumption. The novel technique of generating pyroelectric field using microheaters was unexplored till now. Traditionally, thermal stimulation tools such as: Laser, soldering iron, hot plate and Peltier were used to create a variation in temperature so to generate pyroelectric effect that creates a spatial charge distribution on the surface of driving pyroelectric crystal. However, these techniques were limited, as they don't fulfil the modern world demand for lab-on chip process due to macroscopic heating tools. Other limitations in these approaches besides macroscopic heating tools were controlling and manipulating of the temperature gradients. Using integrated microheaters we overcome the aforementioned limitation of thermal stimulation tools.

The effect of the µH shape on the temperature distribution and consequently on the pyroelectric effect was evaluated using COMSOL™ Multiphysics. These microheaters were realize using the traditional microfabrication technique at IMM-CNR Naples. Simulations were validated by different experimental measurements. In particular, the pyroelectric effect activated by the µH was investigated analysing the current impulses detected using a micrometric metallic probe connected to an oscilloscope. The results show that the fan-shaped µH generates electric fields with the highest intensity values. However, the generated current pulses efficiently appeared if the metallic tip was placed not more than 1 mm from the crystal surface. Finally, the high repeatability of the pyroelectric effect induced by the integrated µH was demonstrated reporting the occurrence of the impulses. The reported results let us to claim that by regulating the rate of heating or cooling of the different design of µHs, the occurrence of the pyroelectric effect from the –Z surface of the $LiNbO_3$ can be manipulated and/or controlled is an easy and efficient manner compared with traditional ways of thermalizing the crystal. Furthermore pyroelectric investigation activated by the fan microheater was performed under humidity conditions using the same micrometric metallic probe setup. This study shows the microheater as a heating tools that can be used in different ambient conditions in order to generate the pyroelectric effect from $LiNbO_3$ crystal.

Thereafter, the effectiveness of the microheater in order to generate pyroelectric fields were demonstrated to draw liquid droplet, microneedle formation and micro-electro spinning of polymer. Initially, we demonstrate a simple way to draw nano-pico litter's liquid droplets from one or multiple sessile drops or liquid film reservoirs using pyroelectrohydrodynamic (PED) dispenser induced by $LiNbO_3$ using integrated fan shape microheater. Local pyroelectric forces, which are activated by using microheater fabricated on lithium niobate substrate, draw liquid droplets from the reservoir below substrate, and deposit then on the underside of the lithium niobate substrate.

Furthermore, realization of an optimized micro-heaters array in order to control the heat distribution over a large area about 1.25×1.25 cm^2, on lithium niobate ($LiNbO_3$) crystal was reported. The optimized device will provide us with several benefits, as the possibility of producing microneedles array with high uniformity in shape and height, in specific and relative wide area, with high accuracy.

We also report, on an innovative version of electro-spinning (ES) that we call micro-pyro-electrospinning (µ-PES) by controlling the electric field generated pyroelectrically by integrated fan microheater. The pyro-

electrohydrodynamic process activated in this way can be used to manipulate soft matter and is also able to generate true spiral patterns at microscale by a direct process.

Appendix

A.1 **Implementation of integrated system for thermal control of microfluidic circuits for biological imaging applications.**

The main objective of the work focuses on the design, implementation and characterization of integrated device for temperature control in microfluidic device to improve the techniques of live imaging of biological samples. The temperature control of living cells ("Live-imaging") is crucial for the analysis of certain cellular phenomena. In particular this is fundamental in the study of the routes that follow the protein, starting of the production until reaching the target site, whether it is intra-or extra cellular. Monitoring of these paths, given the high speed with which they occur, is related to the option to block temporally and then reactivate them. This can be achieved by bringing the temperature to below a threshold value, and then reactive to physiological values. The determination of the role and behaviour of proteins and / or protein complexes within the cell is high interest in biological research, from this information we can understand the behaviour of the cell. This is crucial to the study of cells affected by disease states, as in the case of cancer cells, in order to understand the origin and development of the disease itself. Currently the temperature in the cell samples is controlled by immersion in a waterbath, and then subsequently brought under the microscope, with problems mainly due to the temperature variation in the passage between the two workstations. At the front of these considerations, it is clear that to have a platform that allows to control the temperature inside a cell culture chamber directly under the microscope, both in the optimization of the sample preparation process, and both in the quality of the results obtained.

Once we define the objective and after some initial considerations in the design phase, it was decided to realize the heating system through the use of a micro-heater, and the cooling circuit through the use of cold water circulating all ' internal micro-channels surrounding the cell culture chamber. The solution has guaranteed the attainment of temperatures in the centre of the cell culture chamber comprise between 15^0C to 40^0C. In line with the requirements necessary to carry out the biological of interest analysis.

In the first phase, finite element analysis carried out using the simulation program Comsol Multiphysics. The final model that has been achieved. Individually the various components and their functions are analysed, the imposed boundary conditions, and the physics used. They are then brought back to the studies carried out and the analysis of the results obtained.

In the second phase, the experimental activity, they are described in the manufacturing processes of the device, carried out in the clean room at the Institute for Microelectronics and Microsystems (IMM) of the CNR of Naples, and the results of the measurements performed to characterize the ability of cooling and heating of the manufactured devices.

The experimental results have shown that the proposed solution allows to efficiently check the temperature inside the culture chamber cellular in the range of temperatures desired for the study of biological phenomena of interest.

A.1.1 **Design and Modelling**
Modelling

In this section we will be exclusively described the realization of the final model while at a later stage we will be describing the remaining models made giving particular relevance to the findings and reasons for which were not chosen. The component has been realized going to reproduce as faithfully as possible the chip as designed. Figure A.1.1 shows the design of the PDMS sample with the cooling channels, the load and the culture chamber. The geometry of the cooling channels has been realized following constraints:

• The cooling channels must surround as much as possible the culture chamber

• must reduce to a bare minimum the number of input / output holes for the liquid, in order to avoid an excessive encumbrance in the use phase of the device.

• must be avoided as much as possible to create channels between too close to problems that can come and create during the manufacturing phase (filling for deformation, rupture of the PMDS, ...)

• Space as much as possible the inlet / outlet holes each other and from the edges of the PDMS layer.
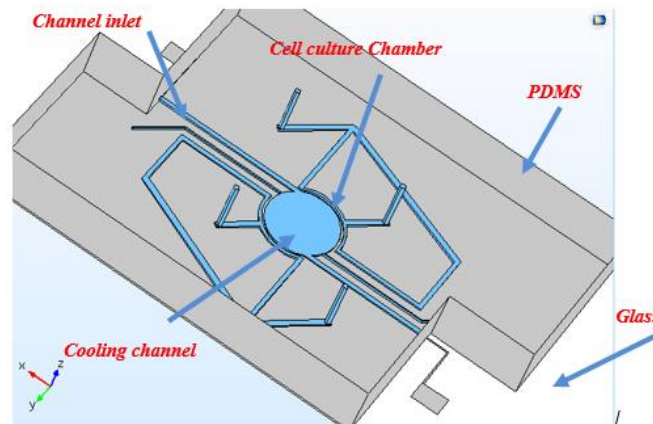
FigA.1.1: The complete microfluidics lab on chip device setup.

The work is aimed to the realization of a device capable of managing the temperature inside a cell culture chamber, for the study of intracellular phenomena that are activated or deactivated at different temperatures. The range of temperatures of interest to perform the analysis is comprised between 15 ° C and 40 ° (± 1 ° C). Assuming the ambient temperature is 25^0C thus it is evident the need to provide a system capable of both heating and cooling inside the chamber. The two fundamental criteria to be met are:

•   The bottom of the device must be transparent, at least in the area in correspondence of the cell culture chamber, to allow the use of an inverted microscope.

•   The device must be as compact as possible.

It was therefore decided to carry out the cell chamber in PDMS this being a polymer permeable to gases and impermeable to liquids and biocompatible and, therefore, suitable to being used for cell cultures. The chamber in the polymer must be closed with a microscope slide with a thickness of 170μm. It will form the surface on which cells adhere. The thickness is determined on the basis of the focal distance of the targets used for cell imaging. The room designed has a cylindrical shape with a radius 2.5 mm and height of 150μm has a channel for the loading of cells of height equal to that of the chamber, and a width of 100μm. Two additional channels have also been inserted for the passage of a temperature sensor useful during the phase of the device characterization. As a heating mechanism is a micro heater positioned below the slide is inserted. The geometry has been chosen so as to allow the use of an inverted microscope (Figure A.1), and at the same time ensure a temperature distribution of a sufficiently uniform in the central area. The heating mechanism is a micro heater which is realized below the glass slide. The geometry was chosen so as to allow the use of inverted microscope (see fig A.1.2.a) and at the same time ensuring a sufficiently homogeneous temperature distribution in the central area. The radius of the empty area in the centre coincides with the radius of the culture chamber, so as to ensure the imaging. The thickness of microheater was assumed equal to 300 nm since it is an easily replicable value in the stage of manufacture with the equipment located at the CNR-IMM, while the two characteristics

widths are 400μm for the "plates" (Figure A.1.2 a) and 100μm for the rest of the micro heater. The material chosen for the realization of microheater is titanium as it has good electrical properties and at the same time suffers little oxidation. For cooling, a system of channels is created, it is also made in the PDMS layer, which "embrace" the cell, inside which water is circulated at a controlled temperature. Even these channels have a height equal to that of the chamber but a width of 400μm. For the phase of the device characterization it was thought to a resistive temperature sensor placed inside the chamber ("Minder" sensor) while for the temperature control during use, to a further sensor ("Circular" sensor) place under the slide. The geometry of such sensors is shown in Figure A.1.2.b:
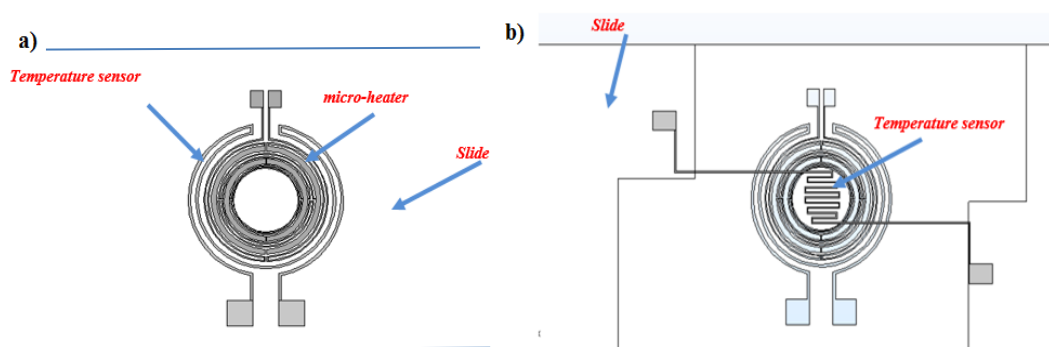
Fig A.1.2: a) View of the lower part of the slide with micro heater and temperature sensor   b) View of the upper part of the slide with temperature sensor.

The geometries of these last three components were designed COMSOL externally by means of a CAD program (Autocad), easier to use for complex geometries, and then subsequently imported. For this reason, the size of these components were fixed in pre-analysis and cannot be directly modified in COMSOL, while the other characteristic dimensions of the geometry have been parameterized in such a way as to make the dimensional modifications of such components faster.

Description	Value	Unit
Width of the slide	24	mm
Length of the slide	72	mm
Thickness of the slide	170	μm
PDMS width	24	mm
PDMS length	35	mm
PDMS height	4	mm
Chamber diameter	5	mm
Room height	150	μm
Wide supply / exhaust channels	100	μm
High power / exhaust channels	150	μm

Width sensor channels "Minder"	300	μm
Height sensor channels "Minder"	150	μm
Width cooling channels	400	μm
Height cooling channels	150	μm
Thick micro heater	300	nm
Width micro heater	100	μm
Width "plates" micro heater	400	μm
Thickness Sensor "Minder"	300	nm
sensor width "Minder"	100	μm
Thickness Sensor "Circular"	300	nm
sensor width "Circular"	100	μm

Table A.I: Dimensions of the various components of the device

The material used for the sensors is aluminium, which has an electrical conductivity very sensitive to temperature changes. It is, however, result, in the process of manufacture of the device, necessary to cover the aluminium layer with a titanium film so as to prevent the formation of oxide on the surface which can significantly change the electrical characteristics of the sensor. The size characteristics of the various components of the device are summarized in Table A.II.

| Parameter	Aluminium	Titanium	PDMS
Heat capacity at constant pressure (Cp)	904 (J/kg*K)	522(J/kg*K)	1460(J/kg*K)
Electrical Conductivity (sigma)	f(T)(S/m)	7.5e5(S/m)	2.5e-14(S/m)
Density (rho)	2700 (kg/m^3)	4506(kg/m^3)	970 (kg/m^3)
Thermal conductivity (k)	237 (W/(m*K)	21.5 (W/(m*K)	0.16 (W/(m*K)
Young's modulus (E)	70e9(Pa)	115.7e9(Pa)	750(Pa)
Coefficient of thermal Expansion (alpha)	23.1e-6 (1/K)	8.6e-6(1/K)	9e-4(1/K)
Poisson's ratio (nu)	0.35	0.321	0.49

Table A.II: Material properties

A.1.2   Numerical Simulation

The simulation is performed using the joules heating multiphysics by coupling the electric current physics with the heat transfer physics and laminar flow physics.

Heat transfer boundary condition

The boundary conditions use is similar as mentioned in the section 2.2.2. In addition a negligible voltage is applied to the resistive sensors in order to have a resistance in the sensors. It is kept in mind that the electrical power dissipate to the sensors doesn't contribute in the thermal gradient of the microheater.
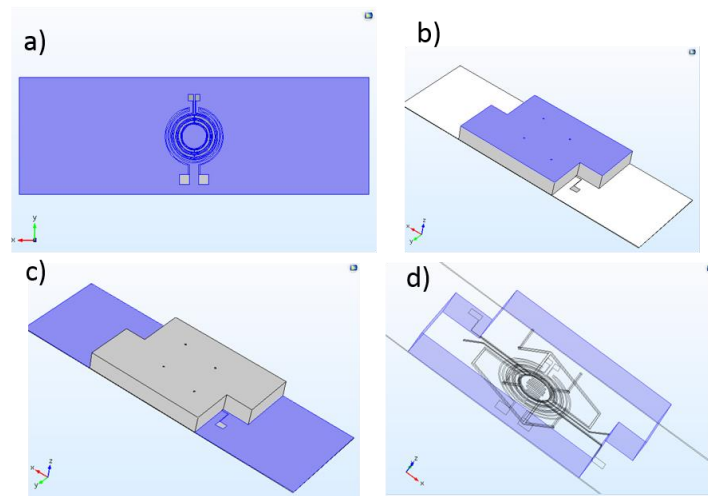

A.1.3. Natural convection cooling conditions a) Lower surface of the glass, b) Top surface of the PDMS layer, c) Top surface of the glass d) vertical side of PDMS layer.

Laminar Flow Boundary conditions

This part of the assignment was performed by the other colleagues involve in this work at IMM-CNR.

Electric Current shell

This module is used to calculate the electric field and potential distribution in layers (shells) conductive assuming that the inductive effects are negligible, namely that the width of the device is much larger than the physical thickness of the shell of electrical currents. In the study, the physical has been applied to the two temperature sensors and to the micro heater as shown in Figure A.1.5.
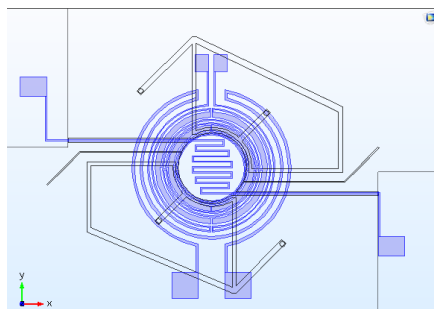

A.1.5.Domains of application of physics "shell electrical currents"

The electrical conductivity and other properties used in the equations have been previously mentioned in the properties of the material and the software acquires during the calculation directly from the library of the material corresponding to the selected surface. In the same physics we have been selected the initial values corresponding to the voltage applied at the initial time (t = 0) equal to V = 0. With regard to the micro heater, as seen in Figure A.1.4, the boundary conditions of the "Terminal" type and "Earth have been applied". The first is a condition used to impose a determined electric potential to the second device while fixing the position of the null potential (V = 0).
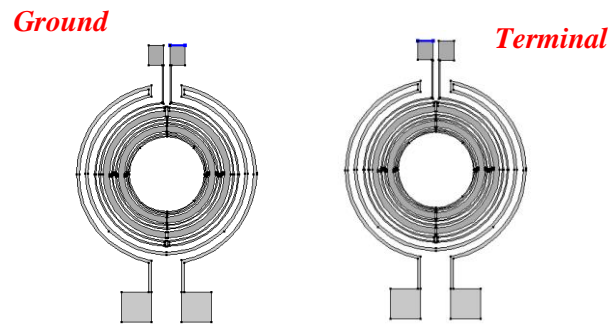
A.1.4.Terminal (a) and Earth (b) of the voltage on the micro heater.

Analogous is the speech for two temperature sensors in which the "terminal condition" has been imposed, rather than a potential, a total current flow, with a very small intensity (0.1 mA), so as to make negligible the 'sensor self-heating effect, but at the same time to allow the generation of a potential difference between the two extremes. In Figure A.1.5 they are shown the points of attachment and ground for both sensors.
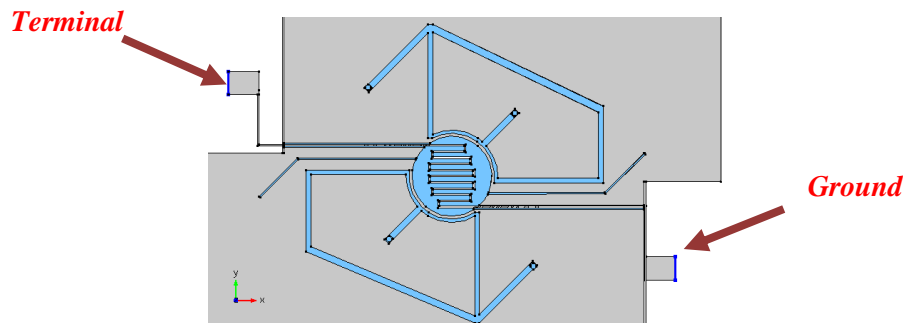
A.1.5. Terminal and ground for top resistive sensor

The multiphysics used in the model are three:

- Heat Source Electromagnetic on the contour, which associates the electromagnetic losses of the surface to a heat source on the border, in the part of the model heat transfer. It is modelled by the equation:

$$-\hat{n} \cdot (-k\nabla T) = Q_b$$

- Coupling of temperature, which causes the temperature calculated by the software being used to evaluate the electrical properties of any material.

Post processing

Studies carried out separately analyse the step of heating and cooling. For the first it was initially carried out a parametric study to vary the voltage applied so as to know the relationship between the voltage and the temperature reached inside the culture chamber once exhausted the initial transient. For this study, in which they are used the physical "transmission of heat in solids" and "Electrical shell currents", is a direct type "MUMS" solver is used for the electric field, while an iterative "GMRES multigrid" for the calculation of temperature, in order to ensure a better management of the large number of elements and therefore the degrees of freedom. The choices of reference voltages are 20 V, 30 V 40 V and 45 V, with a surrounding environment temperature of 23 ° C. The results obtained are shown in the graph in Figure A.1.6.
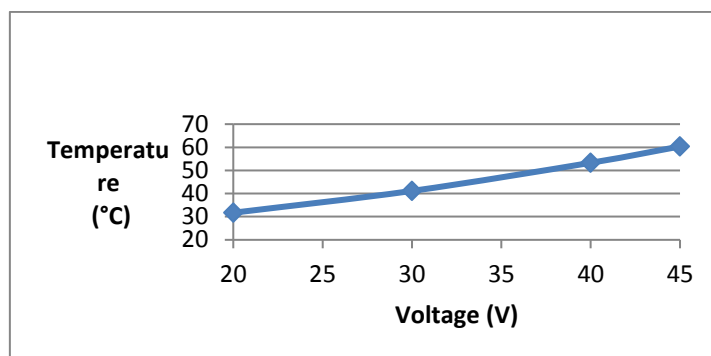
A.1.6. Temperature reached steady as a function of voltage applied to the center of the cell culture chamber.

We notice an almost linear trend of the temperature reached inside the cell chamber as a function of voltage. Again, we need to point out that the results are based on properties of the materials that have been chosen in such a way as to make the model as close to reality. In particular, the titanium was fixed to the value of electrical conductivity $\sigma = 0.75 \times 10^6$ S/m to ensure that the resistance of the micro heater in the model is equal to that of the micro fabricated heater, which is equalled to 6.72 kΩ. It may be noted that increasing of the heat generated, and then the voltage value applied, there is a greater duration of the initial transient due to the presence of the layer of PDMS on the upper face of the slide, which helps to considerably slow down the transfer heat compared to the case in which such thermal resistance is removed (Figure A.1.7).
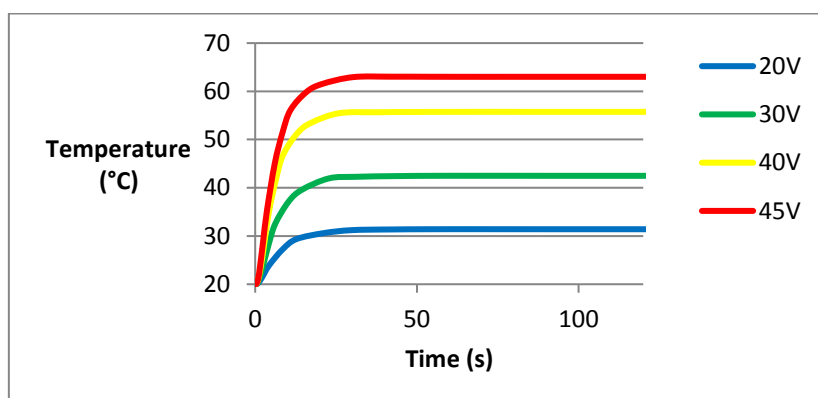
A.1.7 Increase of the temperature at the center of the culture chamber as a function of time to vary the voltage applied in the absence of PDMS layer.

During the simulations, therefore, the voltage values at the terminals of the sensors when the temperature changes were evaluated. The results reported in Figure A.1.8 show an almost linear trend of the output voltage.
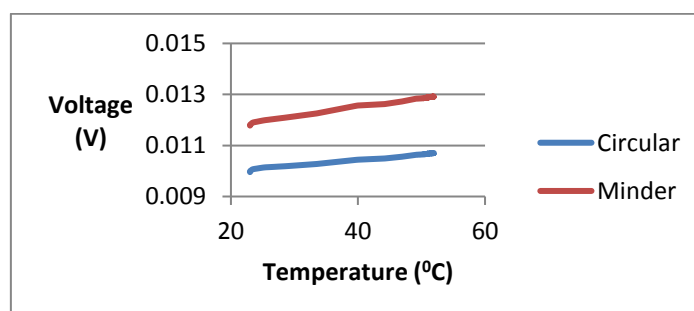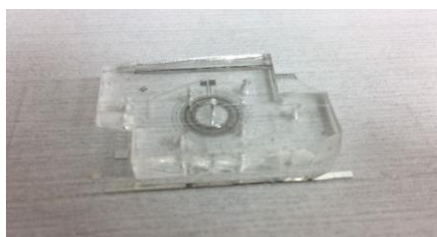

A.1.8 Characterization of the temperature sensors when the temperature changes at the center of the culture chamber.

81

The curve relating to the "Minder" sensor is the sensor characteristic curve as it correlates the thermal input of the area in which it is positioned with an electrical output, while that relating to the "Circular" sensor is a device characterization curve which serves to correlate the temperature of an external area in the room, just the internal temperature.

A.1.3   Fabrication

Fabrication of the resistive thermal sensor was performed using similar photolithography process and metal deposition technique was performed using sputtering. Titanium (Ti) of 300nm-thick for heater material and Aluminium (Al) of 200nm was used for the resistive sensor. Titanium and aluminium was deposited using electron beam and Sputtering technology. The microfluidic chamber was realized PDMS and was bonded on the glass surface with sensor using OXFORD plasma. This work was performed by the microfluidic group at IMM-CNR.


A.1.9. Complete Microfluidic setup

A.1.4   Experimental analysis

Characterization of the sensors

The characterization of aluminum manufactured temperature sensors has been realized by inserting the chip into a glass container with water, placed on a thermostated plate and connecting the electrical connection cables to the two resistance gauges (Figure A.1.10).
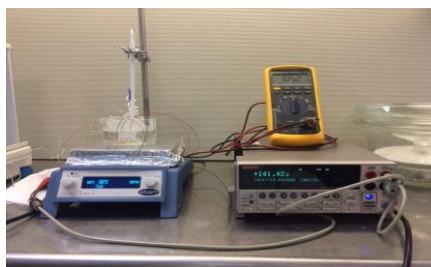

A.1.10 Complete setup for characterization of sensors

The output current was set at 0.1 mA and it is measured the value of the resistance of the two sensors to vary the temperature of the plate. During the measurement process have been used two thermocouples in the water a mail and an inserted all 'inside of PDMS in correspondence of the chamber, to ensure that the temperature of the device reach the one set on the plate.

Characterization of the microheater

In this way it was possible to determine the voltage value required to achieve the desired temperature values (in the range 25-40 ° C). There have also been carried out of the characterization measurements of the micro-heater, on which the sensors also present, in a sample without the PDMS layer. It was therefore possible to compare the experimental measurements with theoretical ones for the complete system. As can be seen from Figure A.1.11, the simulated data faithfully follow the trends of the experimental ones especially for lower

voltages, while for the other tend to deviate more and in particular reach the operating temperature with a speed of less uphill. This difference is mainly due to problems of modeling of the convective heat transfer between the micro-heater and the external environment, due to the complex geometry of the element that does not fall in the common cases reported in literature.
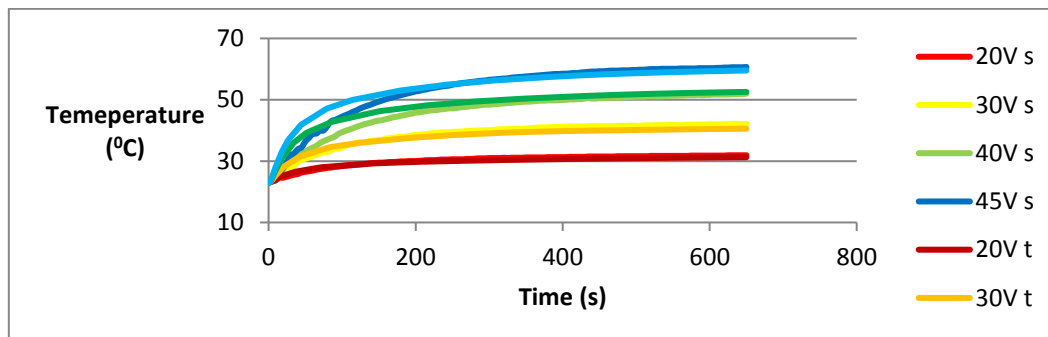
A.1.11 Compare experimental and theoretical data for the heating phase. With "s" refers to the experimental curves while with "t" theoretical ones.

A.1.5 Conclusion

The goal of this work was to achieve an integrated device capable of managing the temperature inside a microfluidic cell culture chamber in a temperature range between 15 ° C and 40 ° C. The work was divided into three phases: Simulation, Realization & Characterization. The temperature measurements inside the culture chamber were carried out through the use of a thermocouple, in replacement of the integrated resistive sensor. The experimental measurements carried out with the combination of cooling and heating systems have evidenced by a side of the real possibility of maintaining a constant temperature in a range of ± 1 ° C for a sufficiently long time to allow the imaging of biological samples, and it has also found a good correspondence between the experimental and theoretical results. It also makes it necessary, in order to realize a user-friendly platform and fully automated, the need to integrate a micro-controller that reads the temperature in the growth chamber and modify the cooling / heating system control parameters, in order to bring and maintain the temperature at the set value.

A.2   Infrared camera (FLIRSC7000)

A study was performed to investigate and compare the temperature distribution from the four different microheater obtained by numerical simulations and experimentally measured. Thermal measurements on titanium microheaters were performed using FLIR SC7000 series thermo camera. The FLIR SC7000 series is specifically designed for scientific applications that require a flexible camera with high sensitivity, accuracy, spatial resolution and speed. The SC7000 series has a 640*512 pixel formats with a low noise level of 20mK. The integration time is adjust-able in nanoseconds increments. The smart external triggering features allows synchronization of the image capture to the most fleeting events. FLIRSC7000 series works seamlessly together with FLIR ResearchIR Max software enabling intuitive viewing, recording and advance processing of the thermal data provided by the camera. The main key features of this thermo camera are: 1) multiple detector options, 2) ultra-high frame rates with windowing, 3) removable filter wheel and 4) multiple video outputs.

Detector Specifications	
Detector Type	Mercury cadmium Telluride (MCT)
Spectral Range	7.7-9.3μm
Resolution	320*256
Detector pitch	30μm
NETD	<25mK (20mK typical)
Well capacity	37/12 M electrons
Operability	>99.5%
Sensor Cooling	Internal sterling

Electronics/Imaging	
Readout	Snapshot (4 channel)
Readout Modes	Asynchronous Integrate then read

Fig A.2: a) FLIR SC7000 series™ thermocamera, b) detector and electronics specifications.

A.3   MATLAB Codes

A.3.1   The heat coefficient calculation code

```matlab
kair=2.5326e-4;                    % in W/cm*K  % 2.5326e-4
densair=1.225e-3;                  % in g/cm^3  % 1.225e-3
cpair=1.007;                       % in J/g*K   % 1.007
diffair=kair/(cpair*densair);      % in cm^2/s
g=9.8066*100;                      % in cm
beta=0.00367;                      % in 1/K     % 0.00367
v=0.14607;                         % in cm^2/s      % 0.14607
pr=v/diffair;                      % numero puro
deltat=20;
A=10e-12;
P=2*(11e-6);
lor=A/P;
%%%%%%%%%%%%%%%%
gror=(g.*beta.*deltat.*(lor.^3))./(v^2);
  raor=gror.*pr;

  if (raor <= 3e11) & (raor > 1e7)
       nuorsu=0.15.*(raor.^(1./3));
   elseif (raor <= 1e7) & (raor > 1e4)
     nuorsu=0.54.*(raor.^(1./4));
     elseif (raor <= 1e4) & (raor > 200)
     nuorsu=0.59.*(raor.^0.256);
    elseif (raor <= 200) & (raor > 1)
nuorsu=0.96.*(raor.^0.169);
   elseif (raor <= 1)
     nuorsu=1.078.*(raor.^0.107);
   end

if (raor <= 3e11) & (raor > 1e6)
  nuorgiu=0.58.*(raor.^(1./5));
   elseif (raor <= 1e6) & (raor > 1e5)
     nuorgiu=0.27.*(raor.^(1./4));
   elseif (raor <= 1e5)
  nuorgiu=nuorsu./2;
```

```
end
```

```
 hcsup=(nuorsu.*kair)./lor;
 hcinf=(nuorgiu.*kair)./lor;
```

A.3.2 Post processing of the thermocamera images for thermal analysis

```
format long
 [ImageDL, ptw] = FLIR_PTWGetFrame ('Array_S_shape_9V_BLACK_RUN2.ptw',
9);
figure;imagesc(ImageDL);colorbar;
 ptw
 load('LUT_1440us.mat')
 Img_translate  // From digital levels to temperature
 a=improfile;   // >> improfile;.

 c = imcrop;
 figure;imagesc(c);axis off;colormap jet;axis image;

 d = imrotate(c,20);
 figure;imagesc(d);colormap jet;
```

A.3.3 Constant Frequency voltage signal varying tip to –Z distance for the microheaters

```
figure;
subplot(5,1,1);
plot(ch1_100um(:,1)-18,ch1_100um(:,2),'black','linewidth',2);
xlim([-2,100])
ylim([-1,15])
%title('Voltage Vs Time for the fan shape microheater @ 10mHz ')
%xlabel('time[s]')
ylabel('Voltage [V]')
grid on
subplot(5,1,2);
plot(ch2_100um(:,1)-68,ch2_100um(:,2),'red','linewidth',2);
% xlabel('time[s]')
% ylabel('Voltage peaks [V]')
%title('Voltage peaks Vs Time @ 0.1mm ')
xlim([-2,100])
ylim([-0.5,0.5])
grid on
subplot(5,1,3);
plot(ch2_250um(:,1)-97.75,ch2_250um(:,2),'blue','linewidth',2);
% xlabel('time[s]')
% ylabel('Voltage peaks [V]')
% title('Voltage peaks Vs Time @ 0.25mm ')
xlim([-2,100])
ylim([-0.5,0.5])
grid on
subplot(5,1,4);
plot(ch2_400um(:,1)-59.1,ch2_400um(:,2),'green','linewidth',2);
xlim([-2,100])
ylim([-0.5,0.5])
% xlabel('time[s]')
% ylabel('Voltage peaks [V]')
%title('Voltage peaks Vs Time @ 0.4mm ')
grid on
subplot(5,1,5);
plot(ch2_1000um(:,1)-45,ch2_1000um(:,2),'black','linewidth',2);
xlim([-2,100])
ylim([-0.5,0.5])
xlabel('time[s]')
% ylabel('Voltage peaks [V]')
```

```
% title('Voltage peaks Vs Time @ 1mm ')
grid on
```

A.3.4 Impulse Occurrence Investigation

Hist code is use for Histogram. N = hist(Y) bins the elements of Y into 10 equally spaced containers and returns the number of elements in each container. If Y is a matrix, hist works down the columns. N = hist(Y,M), where M is a scalar, uses M bins. N = hist(Y,X), where X is a vector, returns the distribution of Y among bins with centres specified by X. The first bin includes data between -inf and the first center and the last bin includes data between the last bin and inf. Note: Use HISTC if it is more natural to specify bin edges instead. [N,X] = hist(...) also returns the position of the bin centres in X. hist(...) without output arguments produces a histogram bar plot of the results. The bar edges on the first and last bins may extend to cover the min and max of the data unless a matrix of data is supplied.

```
% hist(errbarcooling10mHz300mW);figure(gcf);
% varianceOfImage = var(errbarcooling10mHz300mW(:));


subplot(2,1,1)
nbins=40;
hist(errbarheating10mhz300mW,nbins);figure(gcf);
varianceOfImageheating = var(errbarheating10mhz300mW(:));
hold on
subplot(2,1,2)
nbins=40
hist(errbarcooling10mHz300mW,nbins);figure(gcf);
varianceOfImagecoooling = var(errbarcooling10mHz300mW(:));
```

A.3.5 Temporal Distance Evaluation

This code has been written in order to evaluate the temporal distance between the peaks obtained for the Fan shape microheater at 100 micrometre tip to –Z surface of liNbO3 gap spacing for a voltage signal to dissipate a power of 300mW.

```
subplot(5,2,[1 2]);
plot(ch1_100um(:,1)-2,ch1_100um(:,2),'black','linewidth',2);
xlim([15,115])
ylim([-1,15])
title('Applied Voltage signal to Fan shape microheater')
xlabel('time[s]')
ylabel('Voltage [V]')
grid on
hold
subplot(5,2,[3 4]);
plot(ch2_100um(:,1)-2,ch2_100um(:,2),'r','linewidth',1.5);
xlim([65,165])
xlabel('time[s]')
ylabel('Voltage [V]')
title('The respective impulse obtained at 10mHz at 100micrometer tip to -Z
surface')
grid on
grid minor

%%%%%%%%%%%%%%%%%%%%%%%%%%% time defining for half time  ch2_100um(:,1)
```

```matlab
time= ch2_100um(33327:58739,1);

%%%%%%%%%%%%%%%%%%%%%%% fit curve for time from up to down

subplot(5,2,5)
app= ch2_100um(33327:58739,2);
ind=find(abs(app)<.05);
app(ind)=0;
[pks,locs]=findpeaks(abs(app));
plot(time(locs),app(locs),'*b');
hold on
plot(time,app,'m')
xlim([65,115])
ylim([-1,1])
grid on
grid on
xlabel('time for up to down [s]')
ylabel('Vpyro [V]')
title('Cooling Impulse from -Z surface of niobate')


%%%%%%%%%%%%%%%%%%%%%%%%%%%%%%%%%%%%%%%%%%%%%%%%%%%%%%%%%%%%%

diff_locs=diff(time(locs));
plot(diff_locs,'.')

subplot(5,2,7)
ind_loc=find(diff_locs>.01);
data_down=(diff_locs(ind_loc));
plot(data_down,'*')
xlabel('distance between peaks [V]')
ylabel('delta T for peaks[s]')
title('peaks Vs time diference')


%%%%%%%%%%%%%%%%%%%%%%%%%%%%%%%%%%%%%%%%%%%%%%%%%%%%%

time= ch2_100um(58739:84151,1);

%%%%%%%%%%%%%%%%%%%%%%% fit curve for time from up to down

subplot(5,2,6)
app= ch2_100um(58739:84151,2);
ind=find(abs(app)<.05);
app(ind)=0;
[pks,locs]=findpeaks(abs(app));
plot(time(locs),app(locs),'*b');
hold on
plot(time,app,'m')
xlim([115,165])
ylim([-1,1])
grid on
grid on
xlabel('time for up to down [s]')
ylabel('Vpyro [V]')
```

```
title('Heating Impulses from -Z surface of niobate')

%%%%%%%%%%%%%%%%%%%%%%%%%%%%%%%%%%%%%%%%%%%%%%%%%%%%%%%%%%%%%%%%%%

diff_locs=diff(time(locs));
subplot(5,2,8)
ind_loc=find(diff_locs>.01);
data_up=(diff_locs(ind_loc));
plot(data_up,'*')
xlabel('distance between peaks [V]')
ylabel('delta T for peaks[s]')
title('peaks Vs time diference')
```
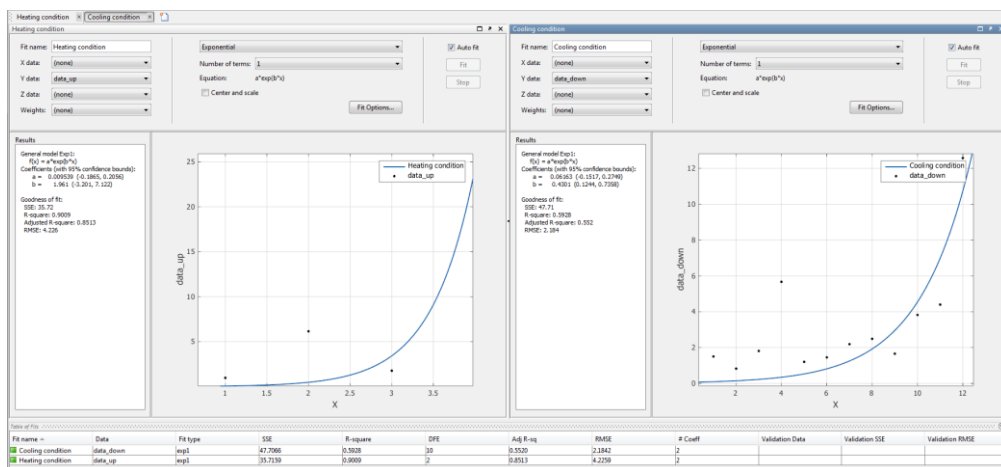
A.3.6 Exponential plot for the impulse occurrence during heating and cooling conditions.

The command cftool opens curve fitting tool or brings focus to the tool if it is already open. cftool(X, Y) creates a curve fit to X input and Y output. X and Y must be numeric, have two or more elements, and have the same number of elements. cftool opens Curve Fitting Tool if necessary.

cftool

A.3.2: Example for cftool command.

Acknowledgements